

Towards Diverse Binary Segmentation via A Simple yet General Gated Network

Xiaoqi Zhao¹, Youwei Pang¹, Lihe Zhang^{1*}, Huchuan Lu^{1,2} and Lei Zhang^{3,4}

¹*Dalian University of Technology, China.

²Peng Cheng Laboratory, China.

³Dept. of Computing, The Hong Kong Polytechnic University, China.

⁴OPPO Research, China.

*Corresponding author(s). E-mail(s): zhanglihe@dlut.edu.cn;

Contributing authors: zxq@mail.dlut.edu.cn; lartpang@mail.dlut.edu.cn;

lhchuan@dlut.edu.cn; cslzhang@comp.polyu.edu.hk;

Abstract

In many binary segmentation tasks, most CNNs-based methods use a U-shape encoder-decoder network as their basic structure. They ignore two key problems when the encoder exchanges information with the decoder: one is the lack of interference control mechanism between them, the other is without considering the disparity of the contributions from different encoder levels. In this work, we propose a simple yet general gated network (GateNet) to tackle them all at once. With the help of multi-level gate units, the valuable context information from the encoder can be selectively transmitted to the decoder. In addition, we design a gated dual branch structure to build the cooperation among the features of different levels and improve the discrimination ability of the network. Furthermore, we introduce a “Fold” operation to improve the atrous convolution and form a novel folded atrous convolution, which can be flexibly embedded in ASPP or DenseASPP to accurately localize foreground objects of various scales. GateNet can be easily generalized to many binary segmentation tasks, including general and specific object segmentation and multi-modal segmentation. Without bells and whistles, our network consistently performs favorably against the state-of-the-art methods under **10** metrics on **33** datasets of **10** binary segmentation tasks.

Keywords: Binary Segmentation, Gated Network, Gated Dual Branch, Folded Atrous Convolution.

1 Introduction

Image segmentation is the process of dividing a digital image into segments that simplify and/or change the representation of the image to something more meaningful and easier to analyze. From the perspective of pixel-level classification, image segmentation can be specifically divided into binary segmentation, semantic segmentation,

instance segmentation and panoramic segmentation. Compared with the others, segmentation problems considered in binary segmentation are more pure and focused, that is, accurately distinguishing the foreground and background. As shown in Fig. 1, binary segmentation has a wide range of applications in military, industrial, medical, etc.

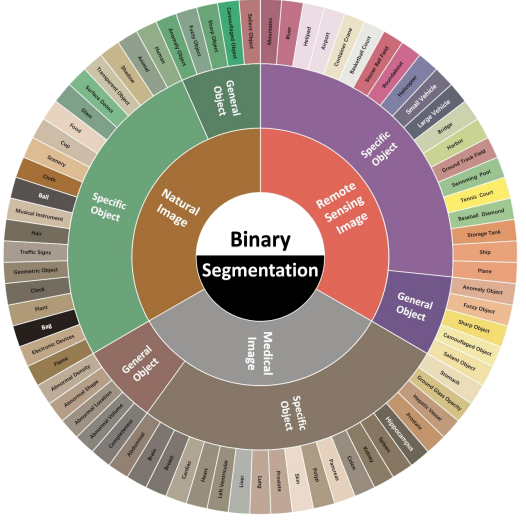


Fig. 1 Some meaningful binary segmentation tasks.

Rich foreground definitions prompt binary segmentation with numerous branches, such as salient object detection, camouflaged object detection, shadow detection and transparent object detection. In recent years, with the development of deep learning, there are many effective methods proposed and achieve good performance. Although each branch of binary segmentation is thriving and show a gratifying state, almost all methods focus on researching single one branch and ignore cross-branch comparison in experiments and techniques. As we know, each branch belongs to the binary segmentation trunk because they have a same mathematical definition. They face many same challenges in segmentation techniques. However, these task branches have become more and more independent, which will impede the development of the entire binary segmentation field. To this end, it is urgent to provide a general method for diverse binary segmentation branches.

There are three challenges in accurate binary segmentation: **Firstly**, most methods [30, 45, 84, 102, 110, 145, 158, 178, 185, 203] tend to adopt U-shape [82, 113] as the baseline and then combine multi-level features in either the encoder [110, 145, 158, 178, 185] or the decoder [45, 84, 158, 189, 211] to gradually reconstruct the high-resolution feature maps. In each convolutional block, they separately formulate the relationships of internal features during forward update. It is well known that the high-quality segmentation predicted in

the decoder relies heavily on the effective features provided by the encoder. Nevertheless, these methods directly use an all-pass skip-layer structure to concatenate the features of the encoder to the decoder in the isolated [30, 31, 87, 113, 178, 203] or nested [30, 102, 109, 193, 202, 211] manner. The effectiveness of feature aggregation at different levels is not quantified. This not only introduces misleading context information into the decoder but also causes that the typically useful features can not be adequately utilized. In cognitive science, Yang *et al.* [169] show that inhibitory neurons play an important role in how the human brain chooses to process the most important information from all the information presented to us. And inhibitory neurons ensure that humans respond appropriately to external stimuli by inhibiting other neurons and balancing excitatory neurons that stimulate neuronal activity. Inspired by this work, we think that it is necessary to set up an information screening unit between each pair of encoder and decoder blocks in binary prediction. It will help distinguish the most task-aware features of foreground regions and suppress background interference. **Secondly**, due to the limited receptive field, a single-scale convolutional kernel is difficult to capture context information of size-varying objects. This motivates many efforts [24, 33, 38, 56, 83, 86, 107, 176, 178] to investigate multi-scale feature extraction. These methods directly equip an atrous spatial pyramid pooling module [12] (ASPP) or DenseASPP [170] in their networks. However, when using a convolution with a large dilation rate, the information under the kernel seriously lacks correlation due to inserting too many zeros. This may be detrimental to the discrimination of subtle image structures. **Thirdly**, both body and boundary of the foreground need to accurately segmented. Most existing models either use progressive decoder [31, 65, 96, 98, 168, 197, 198, 202] or parallel decoder [24, 41, 56, 125, 131, 132, 159, 196]. The progressive structure begins with the top layer and gradually utilizes the output of the higher layer as prior knowledge to fuse the encoder features. This mechanism is not conducive to the recovery of details because the high-level features lack fine information. While the parallel structure easily results in inaccurate localization of objects

since the low-level features without semantic information directly interfere with the capture of global structure cues.

In this paper, we propose a simple yet general gated network (GateNet) for binary segmentation. Firstly, based on the feature pyramid network (FPN), we construct multi-level gate units to combine the features from the decoder and the encoder. We use convolution operation and nonlinear functions to calculate the correlations among features and assign gate values to different blocks. In this process, a partnership is established between different blocks by using weight distribution and the decoder can obtain more efficient information from the encoder and pay more attention to the target-aware regions. Secondly, we construct a folded atrous spatial pyramid pooling (Fold-ASPP) module to gather multi-scale high-level foreground cues. With the “Fold” operation, the atrous convolution is implemented on a group of local neighborhoods rather than a group of isolated sampling points, which can help generate more stable features and more adequately depict finer structure. Thirdly, we design a mix feature aggregation decoder that a parallel branch by concatenating the output of the progressive branch and the features of the gated encoder, so that the residual information complementary to the progressive branch is supplemented to generate the final prediction.

Our main contributions can be summarized as follows.

- We provide a unified perspective of binary segmentation by comprehensively analyzing many binary segmentation tasks.
- We propose a simple gated network to adaptively control the amount of information that flows into the decoder from each encoder block. With multi-level gate units, the network can balance the contribution of each encoder block to the the decoder block and suppress the features of background regions.
- We design a novel folded atrous convolution that can transfer existing multi-scale modules into our Fold style and enjoy more effective feature representation.
- We build a dual branch architecture. They form a residual structure, complement each other through the gated processing and generate better results.

- We construct both single-stream and two-stream gated networks to adapt the binary segmentation required one or two input sources.
- Extensive comparisons with 42 state-of-the-art methods on 33 challenging datasets of 10 binary segmentation tasks, including RGB, RGB-D and optical remote sensing image salient object detection, camouflaged object detection, defocus blur detection, shadow detection, transparent detection, glass detection, mirror detection and polyp segmentation in medical images, show that our method performs much better than other competitors under 10 metrics and possess strong generalization. Hence, it can be seen a strong baseline for the binary segmentation field.

Compared with the ECCV version [201] (Oral) of this work, the following extensions are made.

I) *We conduct a survey on the field of binary segmentation, covering 10 popular branches and 141 fully supervised methods, evaluation metrics and datasets.* **II)** *Deeper theoretical explanations of the proposed gate unit design are added and we improve the previous gate unit into a stronger version.* **III)** *Based on the overall structure of the original single-source input GateNet, we expand a two-stream version of GateNet suitable for two-source input tasks. Meanwhile, our multi-level gate units can further carry forward the spirit of suppress and balance between different sources.* **IV)** *We report much more extensive experimental results that demonstrate the superiority of both single-stream and dual-stream GateNet in 10 popular binary segmentation tasks.* **V)** *We further provide more implementation details and thorough ablation studies at qualitative and quantitative aspects.* **VI)** *We perform in-depth analyses and discussion for our gate unit.*

2 Retrospect

2.1 Diverse Binary Segmentation Tasks (DBS)

As shown in Fig. 1, there are many kinds of binary segmentation in real life. We select 10 currently well-developed and hot tasks that cover the requirements of general and specific object segmentation in natural images, remote sensing images, and medical images. According to the

rapid development of deep learning technology, we only review the research progress in recent five years in order to provide the latest and comprehensive content.

2.1.1 General Object Segmentation

- **RGB Salient Object Detection.** Salient object detection (SOD) aims to segment the most salient (judged by different consciousnesses) regions or objects in various scenes with or without the engineered cues, such as visual cues, geodesic cues, temporal cues, and human attention cues. Usually, it is adopted as a pre-processing step in many computer vision applications, such as scene classification [112], person re-identification [114] and image captioning [34].

- **RGB-D Salient Object Detection.** Although RGB SOD methods can achieve satisfactory performance in segmenting visually salient objects, some complex scenarios are still open to be resolved. For example, salient objects share similar appearance to the background or the other similar trivial objects. In recent years, various depth-assisted salient object detection (RGB-D SOD) methods [9, 107, 193] have been proposed, in which absorbing geodesic cues from the depth map is the hardcore.

- **Remote Sensing Image Salient Object Detection.** Remote sensing images (RSIs) are usually captured by sensors on an airplane as an aerial view under various viewing angle conditions. Although recent decades have witnessed the remarkable success of SOD for natural scene images, there is only a limited amount of researches focusing on SOD for optical remote sensing images (RSIs). Typically, optical RSIs cover a wide scope with complicated background and diverse noise interference.

- **Camouflaged Object Detection.** The study of camouflage has a long history in biology, and more details can be found in [124]. In the field of computer vision, research on camouflaged object detection (COD) is often associated with salient object detection task. In general, saliency models are designed for finding visually salient objects. They are not suitable for finding hidden objects. The local features of the camouflaged object are usually slightly different from the surrounding background. Recently, Fan *et al.* [30] make some attempts towards this direction. They first build

the largest COD dataset, which contains 10,000 images covering 78 camouflaged object categories.

2.1.2 Specific Object Segmentation

- **Defocus Blur Detection.** Defocus blur is a blurring degradation caused by defocusing and inappropriate depth of focus. Defocus blur is a common phenomenon in real life when the scene is beyond the focal distance of the camera. Defocus blur detection can be potentially used to many vision tasks (*e.g.*, autofocus, depth estimation).

- **Shadow Detection.** Shadow is the light effect caused by surface occlusion and are almost ubiquitous in our daily lives. One one hand, shadow can be used as auxiliary information due to rich depth and geometry visual cues. On the other hand, some important details of the object may be hidden when overlapping with shadows. Hence, shadow detection is important for shadow removal [48], scene geometry [60] and camera parameters [155].

- **Glass and Transparent Detection.** Transparent objects are widely present in the real world, such as glass, vitrines, and bottles. And most of them appear in indoor scenes, especially glass-like objects with brittle and smooth properties. Smart robot operates tasks in living rooms or offices, it needs to avoid fragile objects. Hence, it is essential for vision systems to be able to detect and segment transparent objects from input images.

- **Mirror Detection.** As a very important object in daily life, mirrors are ubiquitous. They can not only reflect light, but also present a similar mirror image of surrounding objects or scenes. As a result, once the computer vision system or robot encounters a scene with a mirror, the performance will drop significantly. To avoid this problem, it requires these systems to be able to detect and segment mirrors.

- **Polyp Detection.** According to GLOBO-CAN 2020 data, colorectal cancer is the third most common cancer worldwide and the second most common cause of death. It usually begins as small, noncancerous (benign) clumps of cells called polyps that form on the inside of the colon. Over time some of these polyps can become colon cancers. Therefore, the best way of preventing colon cancer is to identify and remove polyps before they turn into cancer.

Table 1 Summary of essential characteristics for reviewed fully-supervised binary segmentation methods. The superscript “*” in the fifth column (code link) regards this repository does not provide pre-trained weights for re-evaluating performance publicly and “N/A” represents that the code is not available. **STL** is single task learning and **MTL** is multi-task learning.

No.	Year	Methods	Publication	Code Link	Backbone	Learning Paradigm	Training Dataset	#Training
RGB Salient Object Detection								
1	2018	R3Net ^[24]	IJCAI	Pytorch	ResNeXt-101 [162]	STL	MSRA10K [19]	10,000
2		SFCN ^[184]	IJCAI	Caffe	VGG-16 [121]	STL	MSRA10K [19]	10,000
3		BMPM ^[178]	CVPR	TensorFlow	VGG-16 [121]	STL	DUTS [142]	10,553
4		PICAN ^[85]	CVPR	Pytorch	ResNet-50 [44]/VGG-16 [121]	STL	DUTS [142]	10,553
5		PAGRNN ^[189]	CVPR	N/A	VGG-19 [121]	STL	DUTS [142]	10,553
6		DGRL ^[145]	CVPR	Caffe	ResNet-50 [44]	STL	DUTS [142]	10,553
7		RAS ^[15]	ECCV	Pytorch	VGG-16 [121]	STL	MSRA-B [88]	2,500
8	2019	DEF ^[218]	AAAI	N/A	ResNet-101 [44]/DenseNet-161 [51]/VGG-16 [121]	STL	DUTS [142]	10,553
9		AFNet ^[37]	CVPR	Caffe	VGG-16 [121]	MTL	DUTS [142]	10,553
10		BasNet ^[110]	CVPR	Pytorch	ResNet-34 [44]	STL	DUTS [142]	10,553
11		CPD ^[158]	CVPR	Pytorch	ResNet-50 [44]/VGG-16 [121]	STL	DUTS [142]	10,553
12		MLMSNet ^[156]	CVPR	Pytorch	VGG-16 [121]	MTL	DUTS [142]	10,553
13		CapSal ^[179]	CVPR	TensorFlow*	ResNet-101 [44]	MTL	COCO-CapSal [179]/DUTS [142]	5,265/10,553
14		PoolNet ^[83]	CVPR	Pytorch	ResNet-50 [44]/VGG-16 [121]	MTL/STL	BSDS500 [4]+PASCAL VOC [27]+DUTS [142]/DUTS [142]	20,956/10,553
15		PS ^[146]	CVPR	N/A	ResNet-50 [44]/VGG-16 [121]	STL	MSRA10K [19]	10,000
16		PFA ^[196]	CVPR	TensorFlow*	VGG-16 [121]	STL	DUTS [142]	10,553
17		SCRN ^[159]	ICCV	Pytorch	ResNet-50 [44]/VGG-16 [121]	MTL	DUTS [142]	10,553
18		BANet ^[125]	ICCV	Caffe	ResNet-50 [44]/VGG-16 [121]	MTL	DUTS [142]	10,553
19		HRSOD ^[173]	ICCV	Caffe	VGG-16 [121]	STL	HRSOD [173]+DUTS [142]/DUTS [142]	12,163/10,553
20		EGNet ^[194]	ICCV	Pytorch	ResNet-50 [44]/VGG-16 [121]	MTL	DUTS [142]	10,553
21		DUCRF ^[164]	ICCV	Caffe	VGG-16 [121]	STL	MSRA-B [88]	2,500
22		TSPoANet ^[90]	ICCV	N/A	VGG-16 [121]	STL	DUTS [142]	10,553
23	2020	PPFP ^[139]	AAAI	Pytorch	ResNet-101 [44]/VGG-16 [121]	STL	DUTS [142]	10,553
24		GCAPNet ^[17]	AAAI	Pytorch	ResNet-50 [44]	STL	DUTS [142]	10,553
25		F3Net ^[151]	AAAI	Pytorch	ResNet-50 [44]	STL	DUTS [142]	10,553
26		MSANet ^[210]	AAAI	N/A	VGG-16 [121]	STL	DUTS [142]	10,553
27		MINet ^[102]	CVPR	Pytorch	ResNet-50 [44]/VGG-16 [121]	STL	DUTS [142]	10,553
28		ITSD ^[207]	CVPR	Pytorch	ResNet-50 [44]/VGG-16 [121]	MTL	DUTS [142]	10,553
29		LDF ^[152]	CVPR	Pytorch	ResNet-50 [44]	MTL	DUTS [142]	10,553
30		CSNet ^[41]	ECCV	Pytorch	ResNet-50 [40]/ResNet-50 [44]/CSNet [41]	STL	DUTS [142]	10,553
31		GateNet ^[201]	ECCV	Pytorch	ResNet-10x [162]/ResNet-101/ResNet-50 [44]/VGG-16 [121]	STL	DUTS [142]	10,553
32		PFS ^[94]	AAAI	N/A	ResNet-50 [44]	STL	DUTS [142]	10,553
33	2021	KRN ^[163]	AAAI	Pytorch	ResNet-50 [44]	MTL	DUTS [142]	10,553
34		JSODCOD ^[68]	CVPR	Pytorch*	ResNet-50 [44]	MTL	COD10K [30]+CAMO [66]+DUTS [142]	14,593
35		Auto-MIFNet ^[181]	ACM MM	Pytorch	ResNet-50 [44]/VGG-16 [121]	MTL	DUTS [142]	10,553
36		CTDNet ^[205]	ACM MM	Pytorch	ResNet-50/ResNet-18 [44]	MTL	DUTS [142]	10,553
37		VST ^[87]	ICCV	Pytorch	T2T [172]	MTL	DUTS [142]	10,553
38		HRNN ^[133]	ICCV	Pytorch	ResNet-50 [44]/VGG-16 [121]	MTL	HRSOD [173]+DUTS [142]/DUTS [142]	12,163/10,553
39		iNAS ^[42]	ICCV	Pytorch	NAS	STL	DUTS [142]	10,553
40		SCA ^[122]	ICCV	Pytorch	ResNet-101 [44]	STL	SCAS [122]	5,534
RGB-D Salient Object Detection								
41	2018	PDNet ^[212]	ICME	TensorFlow	VGG-16 [121]	STL	MSRA10K [19]+DUTS [142]+NJUD [59]+NLPR [105]	22,553
42		PCA ^[9]	CVPR	N/A	VGG-16 [121]	STL	NJUD [59]+NLPR [105]	2,050
43		AF ^[144]	Access	TensorFlow	VGG-16 [121]	STL	NJUD [59]+NLPR [105]	2,050
44		cmSalGAN ^[57]	TMM	Pytorch	VGG-16 [121]	MTL	NJUD [59]+NLPR [105]	2,050
45		MMC ^[11]	PR	N/A	VGG-16 [121]	STL	NJUD [59]+NLPR [105]	2,050
46		TANet ^[10]	TIP	N/A	VGG-16 [121]	STL	NJUD [59]+NLPR [105]	2,050
47		CPFP ^[193]	CVPR	Caffe	VGG-16 [121]	STL	NJUD [59]+NLPR [105]	2,050
48		DMRA ^[107]	ICCV	Pytorch	VGG-16 [121]	STL	NJUD [59]+NLPR [105]+DUTLF-D [107]	2,985
49		D3Net ^[32]	TNNLS	Pytorch	VGG-16 [121]	STL	NJUD [59]+NLPR [105]	2,185
50		ICNet ^[73]	TIP	Caffe	VGG-16 [121]	STL	NJUD [59]+NLPR [105]	2,050
51		DisenFuse ^[8]	TIP	N/A	VGG-16 [121]	STL	NJUD [59]+NLPR [105]	2,050
52		TDESDF ^[6]	TIP	N/A	VGG-16 [121]	STL	NJUD [59]+NLPR [105]	2,050
53		DPANet ^[16]	TIP	Pytorch	ResNet-50 [44]	MTL	NJUD [59]+NLPR [105]	2,050
54		JL-DCF ^[39]	CVPR	Caffe/Pytorch	ResNet-101 [44]/VGG-16 [121]	STL	NJUD [59]+NLPR [105]	2,200
55		UCNet ^[176]	CVPR	Pytorch	VGG-16 [121]	STL	NJUD [59]+NLPR [105]	2,200
56		A2dele ^[108]	CVPR	Pytorch	VGG-16 [121]	STL	NJUD [59]+NLPR [105]+DUTLF-D [107]	2,985
57		SSF ^[182]	CVPR	Pytorch	VGG-16 [121]	MTL	NJUD [59]+NLPR [105]+DUTLF-D [107]	2,985
58		S2MA ^[86]	CVPR	Pytorch	VGG-16 [121]	STL	NJUD [59]+NLPR [105]+DUTLF-D [107]	2,050/800
59		CoNet ^[56]	ECCV	Pytorch	ResNet-101 [44]	MTL	NJUD [59]+NLPR [105]+DUTLF-D [107]	2,985
60		CMWNet ^[74]	ECCV	Caffe	VGG-16 [121]	STL	NJUD [59]+NLPR [105]	2,050
61		BBSNet ^[74]	ECCV	Pytorch	ResNet-50 [44]/VGG-19/VGG-16 [121]	STL	NJUD [59]+NLPR [105]	2,050
62		HDFNet ^[101]	ECCV	Pytorch	ResNet-50 [44]/VGG-19/VGG-16 [121]	STL	NJUD [59]+NLPR [105]/DUTLF-D [107]	2,185/800
63		DANet ^[203]	ECCV	Pytorch	VGG-19/VGG-16 [121]	STL	NJUD [59]+NLPR [105]/DUTLF-D [107]	2,050/800
64		PGAR ^[14]	ECCV	Pytorch	VGG-16 [121]	STL	NJUD [59]+NLPR [105]/DUTLF-D [107]	2,185/2,985
65		CMMS ^[71]	ECCV	TensorFlow	VGG-16 [121]	MTL	NJUD [59]+NLPR [105]/DUTLF-D [107]	2,985
66		CAS-GNN ^[92]	ECCV	N/A	VGG-16 [121]	STL	NJUD [59]+NLPR [105]	2,050
67		ATSA ^[180]	ECCV	Pytorch	VGG-19 [121]	STL	NJUD [59]+NLPR [105]/DUTLF-D [107]	2,985
68		DASNet ^[195]	ACM MM	Pytorch*	ResNet-50 [44]	STL	NJUD [59]+NLPR [105]	2,200
69		FRDT ^[183]	ACM MM	Pytorch	VGG-19 [121]	STL	NJUD [59]+NLPR [105]+DUTLF-D [107]	2,985
70		MMNet ^[78]	ACM MM	Pytorch	ResNet-50 [40]	STL	NJUD [59]+NLPR [105]+DUTLF-D [107]	2,985
71	2021	HAInet ^[72]	TIP	Pytorch	VGG-16 [121]	STL	NJUD [59]+NLPR [105]/NJUD [59]+NLPR [105]+DUTLF-D [107]	2,050/2,850
72		CDNet ^[58]	TIP	Pytorch	VGG-16 [121]	MTL	NJUD [59]+NLPR [105]/NJUD [59]+NLPR [105]+DUTLF-D [107]	2,050/2,850
73		UTA ^[204]	TIP	Pytorch	ResNet-50 [44]	STL	NJUD [59]+NLPR [105]	2,200
74		DSNet ^[153]	TIP	Pytorch	ResNet-50 [44]	MTL	NJUD [59]+NLPR [105]	2,185
75		RD3D ^[13]	AAAI	Pytorch	ResNet-50 [44]	STL	NJUD [59]+NLPR [105]/NJUD [59]+NLPR [105]+DUTLF-D [107]	2,185/2,985
76		DSA2F ^[126]	CVPR	Pytorch*	VGG-19 [121]	STL	NJUD [59]+NLPR [105]/NJUD [59]+NLPR [105]+DUTLF-D [107]	2,985
77		DCF ^[55]	CVPR	Pytorch	ResNet-50 [44]	STL	NJUD [59]+NLPR [105]/NJUD [59]+NLPR [105]+DUTLF-D [107]	2,985
78		CMI ^[177]	ICCV	Pytorch	ResNet-50 [44]	STL	NJUD [59]+NLPR [105]/NJUD [59]+NLPR [105]+DUTLF-D [107]	2,185/2,985
79		SPNet ^[205]	ICCV	Pytorch	ResNet-50 [40]	STL	NJUD [59]+NLPR [105]/NJUD [59]+NLPR [105]+DUTLF-D [107]	2,185
80		DFM-Net ^[188]	ACM MM	Pytorch	ResNet-34 [44]/MobileNet-v2 [116]	STL	NJUD [59]+NLPR [105]	2,200
81		TriTransNet ^[91]	ACM MM	Pytorch	ResNet-50 [44]	STL	NJUD [59]+NLPR [105]/NJUD [59]+NLPR [105]+DUTLF-D [107]	2,185/2,985
82		CDINet ^[175]	ACM MM	Pytorch	VGG-16 [121]	STL	NJUD [59]+NLPR [105]+DUTLF-D [107]	2,985

No.	Year	Methods	Publication	Code Link	Backbone	Learning Paradigm	Training Dataset	# Training
Salient Object Detection in Optical Remote Sensing Images								
83	2019-2021	LV-Net [70]	TGRS	N/A	N/A	STL	ORSSD [70]	600
84		DAFNet [186]	TIP	Pytorch*	VGG-16 [121]	MTL	ORSSD [70]/EORSSD [186]	600/1,400
85		PDF-Net [69]	NC	N/A	VGG-16 [121]	STL	ORSSD [70]	600
86		MFI-Net [209]	TGRS	N/A	ResNet-34 [44]/VGG-16 [121]	MTL	ORSSD [70]/EORSSD [186]	600/1,400
87		RRNet [22]	TGRS	Pytorch	ResNet-50 [40]	STL	ORSSD [70]/EORSSD [186]	600/1,400
88		GGRNNet [89]	PRCV	N/A	ResNet-50 [44]	STL	ORSSD [70]/EORSSD [186]	600/1,400
89		MJRBNet [135]	TGRS	Pytorch	ResNet-50 [44]/VGG-16 [121]	STL	ORSSD [70]/EORSSD [186]/ORSL-4199 [135]	600/1,400/2,000
Camouflaged Object Detection								
90	2020-2021	SINet [30]	CVPR	Pytorch	ResNet-50 [44]	STL	COD10K [30]+CAMO [66]	4,040
91		PFNet [97]	CVPR	Pytorch	ResNet-50 [44]	STL	COD10K [30]+CAMO [66]	4,040
92		Rank-Net [93]	CVPR	Pytorch	ResNet-50 [44]	STL	COD10K [30]+CAMO [66]	4,040
93		MGL [174]	CVPR	Pytorch	ResNet-50 [44]	MTL	COD10K [30]+CAMO [66]	4,040
94		JSODCOD [163]	CVPR	Pytorch	ResNet-50 [44]	MTL	COD10K [30]+CAMO [66]+DUTS [142]	14,593
95		UGTR [168]	ICCV	Pytorch	ResNet-50 [44]	STL	COD10K [30]+CAMO [66]	4,040
96		MirrorNet [165]	Access	N/A	ResNet-50 [44]	STL	COD10K [30]+CAMO [66]	4,040
97		TANet [111]	TCSVT	N/A	ResNet-50 [44]	STL	COD10K [30]+CAMO [66]	4,040
98		ERRNet [54]	PR	N/A	ResNet-50 [44]	STL	COD10K [30]+CAMO [66]	4,040
Defocus Blur Detection								
99	2018-2021	BTBNet [199]	CVPR	N/A	VGG-16 [121]	STL	CUHK [49]+DUT [199]	1,204
100		DeFusionNet [132]	CVPR	N/A	VGG-16 [121]	STL	CUHK [49]+DUT [199]	1,204
101		CENet [200]	CVPR	Caffe	VGG-16 [121]	STL	CUHK [49]+DUT [199]	1,204
102		R2MRF [131]	AAAI	N/A	DenseNet-161 [51]/VGG-16 [121]	STL	CUHK [49]+DUT [199]	1,204
103		BR2Net [130]	TMM	N/A	ResNeXt [162]/VGG-16 [121]	STL	CUHK [49]+DUT [199]	1,204
104		Depth-Distill [23]	ECCV	Pytorch	ResNeXt-101 [162]/VGG-19 [121]	MTL	CUHK [49]+DUT [199]	1,204
105		IS2CNet [191]	TCSVT	Caffe	VGG-16 [121]	STL	CUHK [49]+DUT [199]	1,204
106		SG [198]	CVPR	Pytorch	VGG-16 [121]	STL	CUHK [49]+DUT [199]	1,204
107		DENets [197]	TIP	Pytorch	VGG-16 [121]	STL	CUHK [49]+DUT [199]	1,204
Shadow Detection								
108	2018-2021	ST-CGAN [140]	CVPR	N/A	ResNeXt-101 [162]	MTL	ISTD [140]/SBU [138]	1,330/4,089
109		DSC [50]	CVPR	Caffe	VGG-16 [121]	STL	SBU [138]	4,089
110		ADNet [65]	ECCV	Pytorch	N/A	STL	SBU [138]	4,089
111		BDRAR [215]	ECCV	Pytorch	ResNeXt-101 [162]	STL	SBU [138]	4,089
112		ARGAN [25]	ICCV	N/A	VGG-16 [121]	STL	ISTD [140]/SBU [138]	1,330/4,089
113		DSDNet [206]	CVPR	Pytorch	ResNeXt-101 [162]	STL	ISTD [140]/SBU [138]	1,330/4,089
114		AFFPN [62]	SPL	Pytorch	ResNeXt-101 [162]	STL	ISTD [140]/SBU [138]	1,330/4,089
115		RCMPNet [79]	ACM MM	N/A	ResNet [44]	STL	SBU [138]	4,089
116		MIB [216]	ICCV	N/A	EfficientNet-B3 [129]/ResNeXt-101 [162]	STL	ISTD [140]/SBU [138]	1,330/4,089
117		FSDNet [49]	TIP	Pytorch	MobileNet-V2 [116]	STL	CUHK-Shadow [49]	7,350
118		ECA [35]	ACM MM	N/A	ResNet-101 [44]	STL	ISTD [140]/SBU [138]/CUHK-Shadow [49]	1,330/4,089/7,350
Transparent Object Detection								
119	2018-2021	TOM-Net [7]	CVPR	Torch	VGG-16 [121]	MTL	TOM-Net [7]	178,000
120		TransLab [160]	ECCV	Pytorch	ResNet-50 [44]	MTL	Trans10K [160]	5,000
121		Trans2Seg [161]	IJCAI	Pytorch	ResNet-50 [44]	STL	Trans10K-v2 [161]	5,000
122		Transfusion [217]	ICCV	N/A	ResNet-50 [44]	MTL	Trans10K [160]	5,000
Glass Object Detection								
123	2018-2021	GDNet [98]	CVPR	Pytorch	ResNeXt-101 [162]	STL	GDD [98]	2,980
124		RCARP [80]	CVPR	N/A	ResNeXt-101 [162]	STL	GSD [80]	3,202
125		EBLNet [43]	ICCV	Pytorch	ResNeXt-101 [162]	MTL	GDD [98]	2,980
Mirror Object Detection								
126	2019-2021	MirrorNet [171]	ICCV	Pytorch	ResNeXt-101 [162]	STL	MSD [171]	3,063
127		PMD [81]	CVPR	Pytorch*	ResNeXt-101 [162]	MTL	MSD [171]	3,063
128		PDNet [96]	CVPR	Pytorch	ResNet-50 [44]	STL	RGBD-Mirror [96]	2,000
Polyp Segmentation (Medical Image)								
129	2020-2021	ACSSNet [187]	MICCAI	Pytorch*	ResNet-34 [44]	STL	Kvasir-SEG [53]/EndoScene [136]	600/547
130		PraNet [31]	MICCAI	Pytorch	Res2Net-50 [40]	STL	Kvasir [53]+CVC-ClinicDB [5]	1,450
131		ResUNet++ [52]	JBHI	TensorFlow*	ResNet [44]	STL	Kvasir [53]+CVC-ClinicDB [5]	1,450
132		TransFuse [190]	MICCAI	N/A	ViT [26]/DeiT [134]/Res2Net [40]/ResNet [44]	STL	Kvasir [53]+CVC-ClinicDB [5]	1,450
133		MSNet [202]	MICCAI	Pytorch	Res2Net-50 [40]	STL	Kvasir [53]+CVC-ClinicDB [5]	1,450
134		EMS-Net [143]	EMBC	N/A	Res2Net-50 [40]	STL	Kvasir [53]+CVC-ClinicDB [5]	1,450
135		APRNet [118]	EMBC	N/A	ResNet-34 [44]	STL	Kvasir-SEG [53]/EndoScene [136]	600/547
136		UACANet [63]	ACM MM	Pytorch	Res2Net-50 [40]	STL	Kvasir [53]+CVC-ClinicDB [5]	1,450
137		SA-Net [150]	MICCAI	Pytorch	Res2Net-50 [40]	STL	Kvasir [53]+CVC-ClinicDB [5]	1,450
138		LOD-Net [18]	MICCAI	Pytorch*	ResNet-101 [44]	STL	Kvasir [53]+CVC-ClinicDB [5]	1,450
139		CCBANet [99]	MICCAI	Pytorch*	ResNet-34 [44]	STL	Kvasir [53]+CVC-ClinicDB [5]	1,450
140		HRENNet [117]	MICCAI	N/A	ResNet-34 [44]	MTL	Kvasir-SEG [53]/Kvasir [53]+CVC-ClinicDB [5]	600/1,450
141		SCR-Net [154]	AAAI	N/A	N/A	STL	Kvasir-SEG [53]	700

Table 2 Summary of essential characteristics for reviewed fully-supervised binary segmentation methods.

The superscript “*” in the fifth column (code link) regards this repository does not provide pre-trained weights for re-evaluating performance publicly and “N/A” represents that the code is not available.

No.	Year	Methods	Publication	Code Link	Core Components	Framework Style	CRF	Deep Supervision	Targeted Loss
RGB Salient Object Detection									
2018	2018	R3Net ^[24]	IJCAI	Pytorch	Recurrent residual refinement network; Residual refinement block	Parallel	✓	✓	✓
		SFCN ^[184]	IJCAI	Caffe	Symmetrical fully convolutional network; Structural loss	Progressive			
		BMPM ^[178]	CVPR	TensorFlow	Multi-scale context-aware feature extraction module; Gated bi-directional message passing module	Progressive			
		PICANet ^[85]	CVPR	Pytorch	Pixel-wise contextual attention network; Bidirectional LSTM	Progressive			
		PAGRNet ^[189]	CVPR	N/A	Progressive attention; Multi-path recurrent feedback	Progressive			
		DGRL ^[45]	CVPR	Caffe	Localization-to-Refinement network; Recurrent localization network	Progressive			
		RAS ^[15]	ECCV	Pytorch	Residual learning; Reverse attention	Progressive			
2019	2019	DEF ^[218]	AAAI	N/A	Deep embedding features; Recursive feature integration network; Guided filter refinement network	Progressive		✓	✓
		AFNet ^[37]	CVPR	Caffe	Attentive feedback network; Boundary-enhanced loss	Progressive		✓	✓
		BasNet ^[110]	CVPR	Pytorch	Boundary-aware network; Hybrid loss (pixel-level, patch-level and map-level)	Progressive		✓	✓
		CPD ^[158]	CVPR	Pytorch	Cascaded partial decoder	Progressive			
		MLMSNet ^[156]	CVPR	Pytorch	Multi-task intertwined supervision; Mutual learning module	Progressive			
		CapSal ^[179]	CVPR	TensorFlow	Leverage caption source; New dataset	Progressive			
		PoolNet ^[83]	CVPR	Pytorch	Pooling-based modules; Edge detection branch	Progressive			
		PS ^[146]	CVPR	N/A	Iterative top-down and bottom-up inference network	Progressive			
		PFA ^[196]	CVPR	TensorFlow*	Pyramid feature attention (SA&CA); Edge preservation loss	Parallel			
		SCRN ^[159]	ICCV	Pytorch	Cross refinement unit; Edge-Aware models	Parallel			
		BANet ^[125]	ICCV	Caffe	Selectivity-invariance; Boundary-aware network; Integrated successive dilation module	Parallel			
		HRSOD ^[173]	ICCV	Caffe	New dataset; Global&Local network; Attended patch sampling	Progressive			
		EGNet ^[194]	ICCV	Pytorch	Edge guidance network; Complementary information modeling	Progressive			
		DUCRF ^[164]	ICCV	Caffe	Deep unified CRF Saliency Model	Progressive			
		TSPOANet ^[90]	ICCV	N/A	CapsulNet-based model; Explore the part-object relationships	Progressive			
2020	2020	PPFN ^[139]	AAAI	Pytorch	Feature polishing module	Progressive			
		GCPANet ^[17]	AAAI	Pytorch	Feature interweaved aggregation; Self refinement; Head attention; Global context flow	Progressive			
		F3Net ^[151]	AAAI	Pytorch	Cross feature module; Cascaded feedback decode; Pixel position aware loss	Progressive			
		MSANet ^[210]	AAAI	N/A	Attention transfer learning; Multi-type self-attention;	Progressive			
		MINet ^[102]	CVPR	Pytorch	Aggregate interaction module; Self-interaction module; Consistency-enhanced loss	Progressive			
		ITSD ^[207]	CVPR	Pytorch	Lightweight interactive two-stream decoder (Saliency&Contour); Adaptive contour loss	Progressive			
		LDF ^[152]	CVPR	Pytorch	Body&Detail supervision; Iterative feature interaction network	Progressive			
		CSNet ^[41]	ECCV	Pytorch	A flexible convolutional module (gOctConv); light-weighted SOD model (100K parameters)	Parallel			
		GateNet ^[201]	ECCV	Pytorch	Gate Unit; Folded atrous convolution; Dual branch architecture	Progressive&Parallel			
		PFS ^[94]	AAAI	N/A	Pyramid shrinking decoder; Adjacent fusion module; Scale-aware enrichment module	Progressive			
		KRN ^[163]	AAAI	Pytorch	Coarse locating module; Attention-based sampler; Fine segmenting module	Progressive			
		JSODCOD ^[68]	CVPR	Pytorch*	Adversarial learning; Similarity measure module; Data interaction strategy	Progressive			
2021	2021	Auto-MSFNet ^[181]	ACM MM	Pytorch	NAS-based model; Progressive polishing loss	Progressive			
		CTDNet ^[205]	ACM MM	Pytorch	Complementary tri-lateral decoder	Progressive			
		VST ^[87]	ICCV	Pytorch	Transformer-based model; New token upsampling method	Progressive			
		HRNN ^[133]	ICCV	Pytorch	Low-resolution saliency classification network; High-resolution refinement network	Progressive			
		iNAS ^[42]	ICCV	Pytorch	NAS-based network; Device-aware search scheme; Latency group sampling	Progressive			
		SCA ^[122]	ICCV	Pytorch	New dataset; Semantic scene context-aware framework	Progressive			
RGB-D Salient Object Detection									
2018-2019	2018-2019	PDNet ^[212]	ICME	TensorFlow	RGB-based prior-model; Independent depth encoder	Progressive			
		PCA ^[9]	CVPR	N/A	Multi-level cross-modal fusion; Complementarity-aware fusion module	Progressive			
		AF ^[144]	Access	TensorFlow	Switch map; Weighted RGB and Depth stream output	Progressive			
		cmSalGAN ^[57]	TMM	Pytorch	Cross-modality generative adversarial network	Progressive			
		MMCH ^[11]	PR	N/A	Multi-path multi-modal fusion; Global&Local cross-modal fusion	Progressive			
		TANet ^[10]	TIP	N/A	Three-stream multi-modal fusion; Cross-modal distillation; Channel-wise attention	Progressive			
		CPFP ^[193]	CVPR	Caffe	Contrast loss; Contrast prior; Fluid pyramid integration strategy	Progressive			
		DMRA ^[107]	ICRA	Pytorch	Depth refinement block; Depth-induced multi-scale weighting module; Recurrent attention	Progressive			
		D3Net ^[32]	TNNLS	Pytorch	New dataset; Depth depurator unit	Progressive			
		ICNet ^[73]	TIP	Caffe	Information conversion module; Cross-modal depth-weighted combination block	Progressive			
		DisenFuse ^[8]	TIP	N/A	Disentangled cross-modal fusion	Progressive			
		TDESDF ^[6]	TIP	N/A	Two-stage network; Depth estimation; Deep-selective saliency fusion network	Progressive			
		DPANet ^[16]	TIP	Pytorch	Depth potentiality perception; Gated multi-selectivity attention module	Progressive			
		JL-DCF ^[39]	CVPR	Caffe/Pytorch	Joint learning (JL) and densely-cooperative fusion (DCF)	Progressive			
		UCNet ^[176]	CVPR	Pytorch	Conditional probabilistic model; Saliency consensus; Depth correction network	Progressive			
		A2dele ^[108]	CVPR	Pytorch	Depth distiller; Lightweight architecture	Progressive			
		SSF ^[182]	CVPR	Pytorch	Complimentary interaction module; Compensation-aware loss	Progressive			
		S2MA ^[86]	CVPR	Pytorch	Self-Mutual Attention	Progressive			
		CoNet ^[56]	ECCV	Pytorch	Collaborative learning framework	Parallel			
2020	2020	CMWN ^[74]	ECCV	Caffe	Cross-modal weighting network; RGB-depth interaction modules	Progressive			
		BBSNet ^[74]	ECCV	Pytorch	Bifurcated backbone strategy; Depth-enhanced module	Progressive			
		HDFNet ^[101]	ECCV	Pytorch	Hierarchical dynamic filtering network; Hybrid enhanced loss	Progressive			
		DANet ^[203]	ECCV	Pytorch	Single stream network; Depth-enhanced dual attention; Pyramidally attended module	Progressive			
		PGAR ^[14]	ECCV	Pytorch	Lightweight depth stream; Alternate refinement strategy; Guided residual block	Progressive			
		CMMS ^[71]	ECCV	TensorFlow	Cross-modality feature modulation module; Adaptive feature selection module	Progressive			
		CAS-GNN ^[92]	ECCV	N/A	Graph-based reasoning module	Progressive			
		ATSA ^[180]	ECCV	Pytorch	Flow ladder module; Depth attention module	Progressive			
		DASNet ^[195]	ACM MM	Pytorch*	Channel-aware fusion model; Depth awareness module; Depth-aware error loss	Progressive			
		FRDT ^[183]	ACM MM	Pytorch	Interweave fusion module; Gated select fusion module; Adaptive fusion module	Progressive			
		MMNet ^[78]	ACM MM	Pytorch	Cross-modal multi-stage fusion; Bi-directional multi-scale decoder	Progressive			
2021	2021	HAINet ^[72]	TIP	Pytorch	Hierarchical alternate interaction module	Progressive			
		CDNet ^[58]	TIP	Pytorch	Depth estimation; Two-stage cross-modal fusion	Progressive			
		UTA ^[204]	TIP	Pytorch	Gated multi-scale predictor; Channel-aware fusion model; Depth-aware error loss	Progressive			
		DSNet ^[153]	TIP	Pytorch	Dynamic selective module; Cross-modal context module	Progressive			
		RD3D ^[13]	AAAI	Pytorch	3D encoder-decoder; Rich back projection paths	Progressive			
		DSA2F ^[126]	CVPR	Pytorch*	NAS-based model; Depth-sensitive attention	Progressive			
		DCF ^[55]	CVPR	Pytorch	Cross reference module; Depth calibration	Progressive			
		CMINet ^[177]	ICCV	Pytorch	Multi-stage cascaded learning; Mutual information minimization regularizer; New dataset	Progressive			
		SPNet ^[208]	ICCV	Pytorch	Specificity-preserving network; Cross-enhanced integration module; Multi-modal feature aggregation module	Progressive			
		DFM-Net ^[188]	ACM MM	Pytorch	Depth quality-inspired feature manipulation	Progressive			
		TriTransNet ^[91]	ACM MM	Pytorch	Triplet transformer embedding module; Spatial&Channel attention	Progressive			
		CDINet ^[175]	ACM MM	Pytorch	RGB-induced detail enhancement; Depth-induced semantic enhancement; Dense decoding reconstruction	Progressive			

No.	Year	Methods	Publication	Code Link	Core Components	Framework Style	CRF	Deep Supervision	Targeted Loss
Salient Object Detection in Optical Remote Sensing Images									
83	2019-2021	LV-Net[70]	TGRS	N/A	New dataset; L-shaped module; V-shaped module	Progressive			
84		DAFNet[186]	TIP	Pytorch*	New dataset; Dense attention fluid; Global context-aware attention	Progressive	✓		✓
85		PDF-Net[69]	NC	N/A	Parallel down-up fusion network; Dense connection	Progressive			
86		MFI-Net[209]	TGRS	N/A	Multi-scale feature integration under the explicit and implicit assistance of salient edge cues	Progressive	✓	✓	
87		RRNet[22]	TGRS	Pytorch	Parallel multi-scale attention; Relational reasoning module	Progressive			✓
88		GGRNet[89]	PRCV	N/A	Global graph reasoning module	Progressive			
89		MJRBm[135]	TGRS	Pytorch	New dataset; Multi-scale joint boundary and region model	Progressive	✓	✓	
Camouflaged Object Detection									
90	2020-2021	SINet[30]	CVPR	Pytorch	New dataset; Search and identification net	Progressive			
91		PFNet[97]	CVPR	Pytorch	Distraction mining strategy; Positioning and focus network	Progressive			
92		Rank-Net[93]	CVPR	Pytorch	Camouflaged object ranking&localization; New dataset; Triplet tasks learning model	Progressive			✓
93		MGL[174]	CVPR	Pytorch	Mutual guidance knowledge; Graph-based interaction module	Progressive			
94		JSODCOD[163]	CVPR	Pytorch	Adversarial learning; Similarity measure module; Data interaction strategy	Progressive			✓
95		UGTR[168]	ICCV	Pytorch	Bayesian learning into Transformer-based reasoning; Uncertainty-guided transformer reasoning model	Progressive			✓
96		MirrorNet[165]	Access	N/A	Object proposal; Bio-inspired attack stream	Progressive			✓
97		TANet[111]	TCSVT	N/A	Texture-aware refinement module; Boundary-consistency loss	Progressive			✓
98		ERRNet[54]	PR	N/A	Selective edge aggregation; Reversible re-calibration unit	Progressive	✓		✓
Defocus Blur Detection									
99	2018-2021	BTBNet[199]	CVPR	N/A	New dataset; Fully convolutional; Multi-stream network	Progressive			
100		DeFusionNet[132]	CVPR	N/A	Multi-scale deep features	Parallel	✓		
101		CENet[200]	CVPR	Caffe	Cross-ensemble network	Progressive	✓		
102		R2MRF[131]	AAAI	N/A	Residual refinement modules	Parallel	✓		
103		R2B2Net[130]	TMM	N/A	New dataset; Residual learning and refining module	Progressive			
104		Depth-Distill[23]	ECCV	Pytorch	Depth information; Depth Distillation; Selective reception fields block	Progressive			
105		IS2CNet[191]	TCSVT	Caffe	Hierarchical feature integration and bi-directional delivering mechanism	Progressive			
106		SG[198]	CVPR	Pytorch	New dataset; Dual adversarial discriminators; Unsupervised learning	Progressive	✓		✓
107		DENets[197]	TIP	Pytorch	Deep ensemble networks; Self-negative correlation and error function	Progressive	✓		✓
Shadow Detection									
108	2018-2021	ST-CGAN[140]	CVPR	N/A	Shadow detection and shadow removal; Stacked conditional generative adversarial network; New dataset	Progressive			
109		DSC[50]	CVPR	Caffe	Spatial recurrent neural network; Direction-aware spatial context	Progressive			
110		ADNet[65]	ECCV	Pytorch	GAN-based framework; Shadow detection/attenuation network	Progressive			
111		BDRAR[215]	ECVV	Pytorch	Recurrent attention residual module; Bidirectional feature pyramid network	Progressive	✓	✓	
112		ARGAN[25]	ICCV	N/A	Attentive recurrent generative adversarial network	Progressive			
113		DSDNet[206]	CVPR	Pytorch	Distraction-aware shadow module	Progressive			
114		AFFPN[62]	SPL	Pytorch	Attentive feedback feature pyramid network	Progressive			
115		RCMPNet[79]	ACM MM	N/A	Relative confidence map prediction network	Progressive			
116		MIB[216]	ICCV	N/A	Feature decomposition and reweighting; Self-supervised	Progressive			
117		FSDNet[49]	TIP	Pytorch	New dataset; Detail enhancement module	Progressive			
118		ECA[35]	ACM MM	N/A	Effective-Context augmentation	Progressive			
Transparent Object Detection									
119	2018-2021	TOM-Net[7]	CVPR	Torch	The first CNN-based model for transparent object detection; New dataset	Progressive			
120		TransLab[160]	ECCV	Pytorch	New dataset; Boundary attention module	Progressive			
121		Trans2Seg[161]	LJCAI	Pytorch	New dataset; Transformer-based network	Progressive			✓
122		Transfusion[217]	ICCV	N/A	New dataset; RGB-D SLAM approach	Progressive			✓
Glass Object Detection									
123	2020-2021	GDNet[98]	CVPR	Pytorch	New dataset; Large-field contextual feature integration module	Progressive			
124		RCARP[80]	CVPR	N/A	New dataset; Rich context aggregation module; Reflection-based refinement module	Progressive	✓		✓
125		EBLNet[43]	ICCV	Pytorch	Refined differential module; Point-based graph convolution network	Progressive	✓		✓
Mirror Object Detection									
126	2019-2021	MirrorNet[171]	ICCV	Pytorch	New dataset; Contextual contrasted feature extraction module	Progressive	✓		✓
127		PMD[81]	CVPR	Pytorch*	New dataset; Relational contextual contrasted local module; Edge detection and fusion module	Progressive	✓		✓
128		PDNet[96]	CVPR	Pytorch	New dataset; Depth information; Dynamic weighting scheme	Progressive	✓		✓
Polyp Segmentation (Medical Image)									
129	2020-2021	ACSNet[187]	MICCAI	Pytorch*	Local context attention; Global context Module; Adaptive selection module	Progressive			
130		PraNet[31]	MICCAI	Pytorch	Parallel partial decoder; Recurrent reverse attention	Progressive			
131		ResUNet++[52]	JBHI	TensorFlow*	Parallel partial decoder; Recurrent reverse attention	Progressive	✓		
132		TransFuse[190]	MICCAI	N/A	combines Transformers and CNNs in a parallel style; BiFusion module	Progressive			
133		MSNet[202]	MICCAI	Pytorch	Multi-scale subtraction module; LossNet	Progressive			
134		EMS-Net[143]	EMBC	N/A	Receptive field block; Local context attention	Progressive			
135		APRNet[118]	EMBC	N/A	Alternative prediction refinement network; Prediction residual refinement modules	Progressive			
136		UACANet[63]	ACM MM	Pytorch	Parallel axial attention; Uncertainty augmented context attention	Progressive			
137		SANet[150]	MICCAI	Pytorch	Shallow attention; e Color exchange operation; Probability correction strategy	Progressive			
138		LOD-Net[18]	MICCAI	Pytorch*	Oriented-derivatives feature	Progressive			
139		CCBANet[99]	MICCAI	Pytorch*	Cascading Context module; Attention balance module	Progressive			
140		HRENNet[117]	MICCAI	N/A	Context enhancement module; Adaptive feature aggregation module; Structure consistency aware loss	Progressive	✓		✓
141		SCR-Net[154]	AAAI	N/A	Semantic calibration module; Semantic refinement module	Progressive	✓		✓

2.2 Fully Supervised Binary Segmentation Models

We first formulate the image-based binary segmentation problem. Formally, let \mathcal{X} and \mathcal{Y} denote the input space and output segmentation space,

respectively. Fully supervised learning-based models generally seek to learn an *ideal* image-to-segmentation mapping $f^* : \mathcal{X} \mapsto \mathcal{Y}$ through directly utilizing ground truth masks as supervision signal.

In Tab. 1 and Tab. 2, we categorize recent fully supervised models. Through the analyses of 141 methods in 10 branches, we summarize

some instructive findings: **I)** Single task learning (STL) is still the main learning paradigm in binary segmentation. Compared with STL, the proportion of MTL-based methods is only 34/141 and they finish MTL via cooperating with boundary prediction or depth estimation usually. It is worth noting that MTL-based RGB SOD methods have reached the 6/9 scale in 2021. We believe that the potential of MTL is huge, and more effective and richer strategies will emerge in the future under the continuous efforts of researchers. **II)** Our GateNet is the only one mixes both progress and parallel structures among 141 methods, thereby enjoying the advantages of both. Most methods still adopt the single progressive style. **III)** Conditional random field (CRF) gradually disappear in many models. Only some shadow and mirror detection methods adopt the CRF as post-processing. **IV)** Deep supervision becomes a popular supervision approach. 73/141 methods build the network with side outs to perform deep supervision. On one hand, deep supervision [67] is originally designed to speed up network convergence. On the other hand, it may bring extra performance gain for most models. **V)** Targeted loss function is conducive to performance improvement. 72/141 models directly adopt previous or re-design a new targeted loss, such as the hybrid loss [110], consistency-enhanced loss [102], pixel position aware loss [151], etc. It is clear that there is increasing competition in the research of targeted loss.

2.3 Multi-scale Feature Extraction

The multi-scale paradigm is mainly inspired by the scale-space theory that has been widely validated as an effective and theoretically sound framework. It is well suited for addressing naturally occurring scale variations. Common forms in the field of computer vision mainly include the image pyramid [2] and the feature pyramid [82, 113]. Although the former has shown good performance, its application is limited by high computational and latency costs associated with the multi-input parallel processing paradigm, which makes it gradually give way to the more efficient latter in the era of deep learning. The feature pyramid can be roughly divided into two categories according to the form, namely, the inter-layer pyramid and the intra-layer pyramid.

The former is based on features with different scales extracted by the feature encoder, such as the U-shape [82, 102, 104, 109, 113, 189] architecture. In this way, the internal cross-layer information propagation path progressively integrates semantic context and texture details from diverse scale representations. The intra-layer pyramid [12, 170, 178, 192, 203] can enhance the diversity of semantic content by constructing the multi-path structure within a layer to obtain a rich combination of receptive fields. Its good pluggability has also made it an important component in the architecture design of modern segmentation methods. Recently, the atrous spatial pyramid pooling module (ASPP) [12] and its variants [103, 115, 128, 149, 157, 170, 203, 219], which typify this structure, are widely applied in many segmentation tasks and networks. Some methods [62, 80, 97, 176, 178, 215] insert several ASPP modules into the encoder/decoder blocks of different levels, while some ones [24, 37, 43, 56, 93, 107] install it on the highest-level encoder block. As a basic component of ASPP, atrous convolution has the advantage of enlarging the receptive field to obtain large-scale features without increasing the computational cost compared to the vanilla convolution. Nevertheless, the repeated stride and pooling operations already make the top-layer features lose much fine information. With the increase of atrous rate, the correlation of sampling points further degrades, which leads to difficulties in capturing the changes of image details (*e.g.*, lathy background regions between adjacent objects or spindly parts of objects). In this work, we propose a folded atrous convolution to alleviate these issues and achieve a *local-in-local* effect. The folded atrous convolution can seamlessly replace the original atrous convolution in ASPP and other variants (*e.g.*, DenseASPP [170], PAFE [203]), thus significantly improving performance.

2.4 Gated Mechanisms

The gated mechanism plays an important role in controlling the flow of information and is widely used in the long short term memory (LSTM). In [3], the gate unit combines two consecutive feature maps of different resolutions from the encoder to generate rich contextual information. And the gated mechanism is also integrated into the block feedback mechanism to bridge multiple

iterations in the recurrent architecture [61]. Zhang *et al.* [178] adopt gate function to control the message passing when combining feature maps at all levels of the encoder. Chen *et al.* [16] propose a gate function controller to focus on regulating the fusion rate of the cross-modal information. Zhang *et al.* [183] utilize the gated select fusion module to selectively process the useful information from two modal features in low-levels. Due to the ability to filter information, the gated mechanism can also be seen as a special kind of attention mechanism. Wang *et al.* [147] exploit the pyramid attention module to enhance saliency representations for each layer in the encoder and enlarge the receptive field. Chen *et al.* [17] propose a head attention module to reduce information redundancy and enhance the top layers features by leveraging both spatial and channel-wise attention. Zhang *et al.* [189] apply both spatial and channel attention to each layer of the decoder. Liu *et al.* [86] construct both self-attention and mutual-attention in a non-local [148] style for extracting the complementary information between the different modalities. Zhu *et al.* [215] design the recurrent attention residual module to combine and process spatial contexts in two adjacent CNN layers. Zhang *et al.* [187] apply both the local context attention and SE-like [47] channel-wise attention for context selection. Taehun *et al.* [63] propose the uncertainty augmented context attention module to incorporate uncertain area for rich semantic feature extraction. More description about attention-based methods can be found in Tab. 2. In general, the above methods unilaterally consider the information interaction between different layers or intra-layer in the encoder or decoder. We integrate the features from the encoder and the decoder to formulate gate function, which has the function of **block-wise attention** and models the overall distribution of all blocks in the network from the global perspective. However, while previous methods utilize the block-specific features to compute dense attention weights for the corresponding block, they directly feed the encoder features into the decoder and do not consider their mutual interference. Our proposed gate unit can naturally balance their contributions, thereby suppressing the response of the encoder to background regions. Experimental results in Fig. 8 and Fig. 9 intuitively demonstrate the effect of

multi-level gate units on the above two aspects, respectively.

3 Proposed Method

The gated network architecture is shown in Fig. 2, in which encoder blocks, transition layers, decoder blocks and gate units are denoted as \mathbf{E}^i , \mathbf{T}^i , \mathbf{D}^i and \mathbf{G}^i , respectively ($i \in \{1, 2, 3, 4, 5\}$ indexes different levels). Their output feature maps are denoted as E^i , T^i , D^i and G^i , respectively. The final prediction is obtained by combining the FPN branch and the parallel branch.

3.1 Network Overview

Encoder Network. In our model, the encoder is based on a common pretrained backbone network, *e.g.*, the VGG [121], ResNet [44] or ResNeXt [162]. We take the VGG-16 network as an example, which contains thirteen Conv layers, five max-pooling layers and two fully connected layers. In order to fit saliency detection task, similar to most previous approaches [45, 178, 185, 189], we cast away all the fully-connected layers of the VGG-16 and remove the last pooling layer to retain details of last convolutional layer.

Decoder Network. The decoder comprises three main components: i) the FPN branch, which continually fuses different level features from $T^1 \sim T^5$ by element-wise addition; ii) the parallel branch, which combines the saliency map of the FPN branch and the feature maps of transition layers by cross-channel concatenation (At the same time, multi-level gate units ($\mathbf{G}^1 \sim \mathbf{G}^5$) are inserted between the transition layer and the decoder layer); iii) the Fold-ASPP module, which improves the original atrous spatial pyramid pooling (ASPP) by using a “Fold” operation. It can take advantage of semantic features learned from E^5 to provide multi-scale information to the decoder.

3.2 Gated Dual Branch

The gate unit can control the message passing between scale-matching encoder and decoder blocks. By combining the feature maps of the previous decoder block, the gate value also characterizes the contribution that the current block of the encoder can provide. Fig. 3 shows the internal

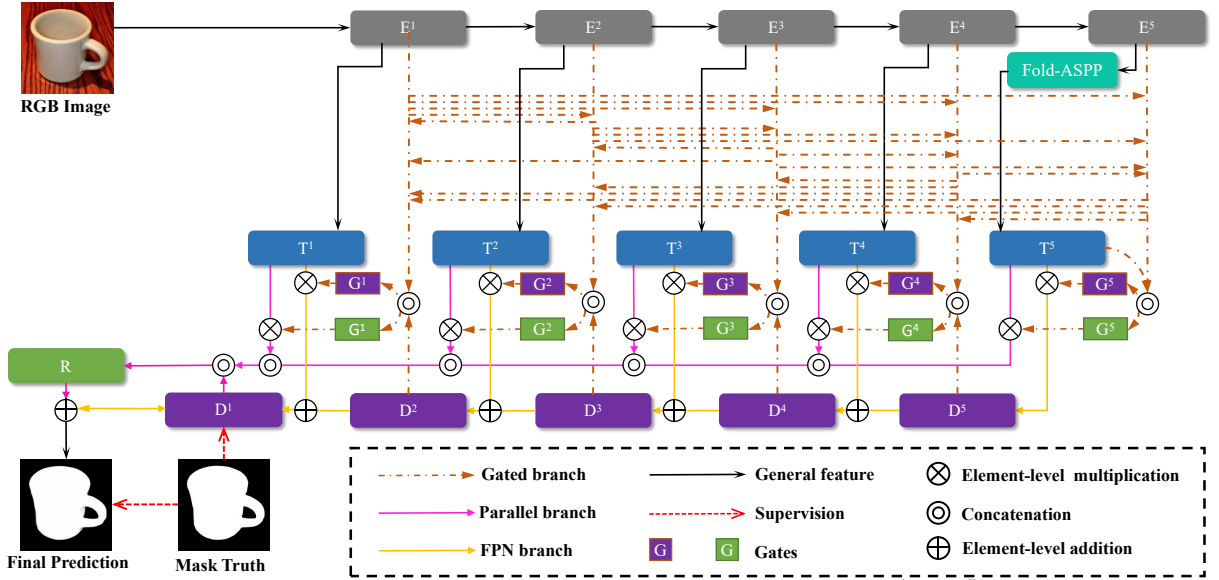


Fig. 2 Overall architecture of the gated network. It consists of five encoder blocks ($E^1 \sim E^5$), five transition layers ($T^1 \sim T^5$), five gate units ($G^1 \sim G^5$), five decoder blocks ($D^1 \sim D^5$) and the Fold-ASPP module. We employ twice supervision in this network. One acts at the end of the FPN branch D^1 . The other is used to guide the fusion of the two branches.

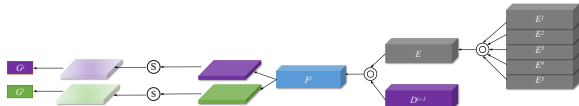


Fig. 3 Detailed illustration of the gate unit. D^{i+1} indicates feature maps of the previous decoder block. \odot is sigmoid function.

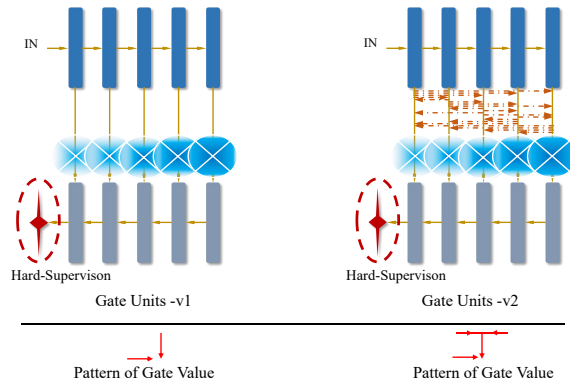


Fig. 4 Architecture comparison between the Gated FPN with gate units-v1 and gate units-v2.

structure of the proposed gate unit. In particular, the aggregated encoder feature E and decoder feature D^{i+1} are integrated to obtain feature F^i , and then the output is fed into two branches, which includes a series of convolution, activation and

pooling operations, to compute a pair of gate values G^i . The entire gated process can be formulated as,

$$E = \text{Conv}(\text{Cat}(E^1, E^2, E^3, E^4, E^5)), \quad (1)$$

$$G^i = \begin{cases} P(S(\text{Conv}(\text{Cat}(E, D^{i+1})))) & \text{if } i = 1, 2, 3, 4 \\ P(S(\text{Conv}(\text{Cat}(E, T^i)))) & \text{if } i = 5 \end{cases} \quad (2)$$

where $\text{Cat}(\cdot)$ is the concatenation operation among channel axis, $\text{Conv}(\cdot)$ is the convolution layer, $S(\cdot)$ is the element-wise sigmoid function, and $P(\cdot)$ is the global average pooling. The output channel of $\text{Conv}(\cdot)$ in Eq. 2 is 2. The resulted gate vector G^i has two different elements which correspond to two gate values in Fig. 3. Given the gate values, we can apply them to the FPN branch and the parallel branch to weight the transition-layer features $T^1 \sim T^5$, which are generated by exploiting 3×3 convolution to reduce the dimension of $E^1 \sim E^4$ and the Fold-ASPP to finely process E^5 (See Fig. 2 for details). Through multi-level gate units, we can suppress and balance the information flowing from different encoder blocks to the decoder.

Compared to the ECCV version [201] of Gate Units-v1, we modify the input feature maps of the

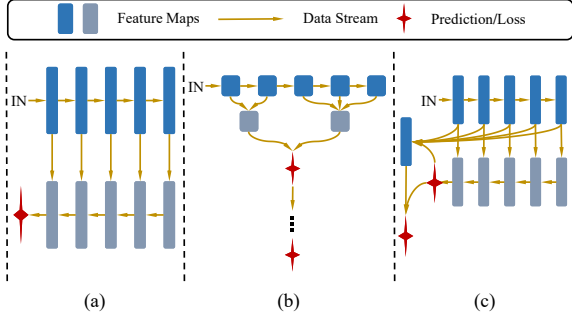


Fig. 5 Illustration of different decoder architectures. (a) Progressive structure. (b) Parallel structure. (c) Dual branch structure.

current encoder block E^i to the all-level aggregated feature maps E . As shown in Fig. 4, the Gated FPN with Gate Units-v2 enjoys bidirectional soft supervision, which motivates the gating values of each layer to consider their corresponding contributions from a global perspective, rather than the local perspective in Gate Unit-v1. In this way, the cooperation among the various layers is closer, thereby, making the optimization of the network more efficient.

Generally, binary segmentation methods usually adopt the progressive or parallel structure as decoder architecture, as shown in Fig. 5(a, b). Progressive style is more conducive to the localization of the objects through the high-level feature guidance, while the parallel style is easier to restore details by making full use of low-level features. As can be seen from Tab. 2, previous methods only adopt either progressive or parallel mode and ignore the advantages brought by the other. In this work, we mix the two structures to build a dual branch decoder to overcome the above restrictions. We briefly describe the FPN branch. Taking D^i as an example, we firstly apply bilinear interpolation to upsample the higher-level feature D^{i+1} to the same size as T^i . Next, to decrease the number of parameters, T^i is reduced to 32 channels and fed into gate unit G^i . Lastly, the gated feature is fused with the upsampled feature of D^{i+1} by element-wise addition and convolutional layers. This process can be formulated as:

$$D^i = \begin{cases} \text{Conv}(G_1^i \cdot T^i + \text{Up}(D^{i+1})) & \text{if } i = 1, 2, 3, 4 \\ \text{Conv}(G_1^i \cdot T^i), & \text{if } i = 5, \end{cases} \quad (3)$$

where D^1 is a single-channel feature map with the same size as the input image.

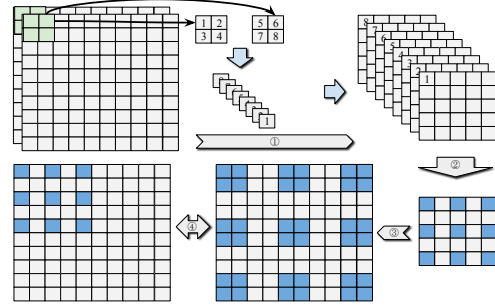


Fig. 6 Illustration of the folded atrous convolution. We use ①, ② and ③ to respectively indicate “Fold” operation, atrous convolution and “Unfold” operation. ④ shows the comparison between atrous convolution (Left) and the folded atrous convolution (Right).

In the parallel branch, we firstly upsample $T^1 \sim T^5$ to the same size of D^1 . Next, the multi-level gate units are followed to weight the corresponding transition-layer features. Lastly, we combine D^1 and the gated features by cross-channel concatenation. The whole process is written as:

$$F_{Cat} = \text{Cat}(D^1, \text{Up}(G_2^1 \cdot T^1), \text{Up}(G_2^2 \cdot T^2), \text{Up}(G_2^3 \cdot T^3), \text{Up}(G_2^4 \cdot T^4), \text{Up}(G_2^5 \cdot T^5)). \quad (4)$$

The final saliency map S^F is generated by integrating the predictions of the two branches with a residual connection as shown in Fig. 5(c),

$$S^F = S(\text{Conv}(F_{Cat}) + D^1), \quad (5)$$

where $S(\cdot)$ is the element-wise sigmoid function.

3.3 Folded Atrous Convolution

In order to obtain robust segmentation results by integrating multi-scale information, atrous spatial pyramid pooling (ASPP) is proposed in Deeplab [12]. And many works [43, 56, 62, 80, 93, 97, 107, 176, 178, 215] also show its effectiveness in different binary segmentation branches. The ASPP uses multiple parallel atrous convolutional layers with different dilation rates. The sparsity of atrous convolution kernel, especially when using a large dilation rate, results in that the association relationships among sampling points are too weak to extract stable features. In this paper, we apply a simple “Fold” operation to effectively relieve this issue. We visualize the folded atrous convolution

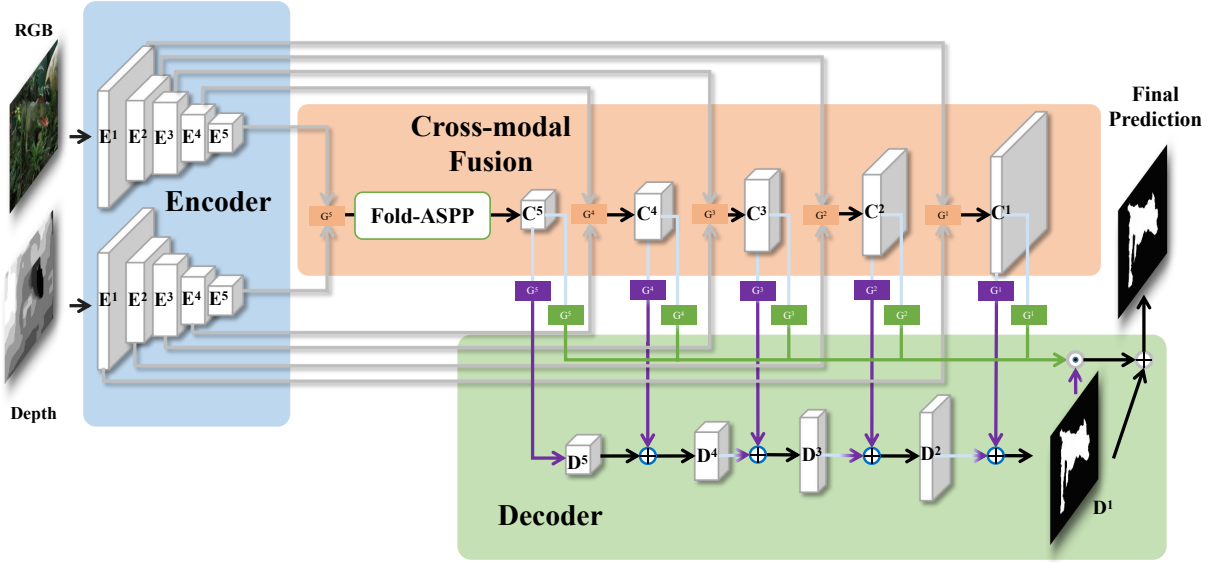


Fig. 7 Overall pipeline of the two-stream gated network. Firstly, we use two independent encoders to extract features for each modality separately. Fold-ASPP is followed and embedded in the top layer of the encoder. And then, we utilize multi-level gate units to control both cross-modal fusion and fused information transmitted to the decoder. The final prediction is yielded by the gated dual branch.

structure in Fig. 6, which not only further enlarges the receptive field but also extends each valid sampling position from an isolate point to a 2×2 connected region.

Let \mathbf{X} represent feature maps with the size of $N \times N \times C$ (C is the channel number). We slide a 2×2 window on \mathbf{X} in stride 2 and then conduct atrous convolution with kernel size $K \times K$ in different dilation rates. Fig. 6 shows the computational process when $K = 3$ and dilation rate is 2. Firstly, we collect $2 \times 2 \times C$ feature points in each window from \mathbf{X} and then it is stacked by channel direction, we call this operation “Fold”, which is shown in Fig. 6①. After the fold operation, we can get new feature maps with the size of $N/2 \times N/2 \times 4C$. A point on the new feature maps corresponds to a 2×2 area on the original feature maps. Secondly, we adopt an atrous convolution with a kernel size of 3×3 and dilation rate is 2. Followed by the reverse process of “Fold” which is called “Unfold” operation, the final feature maps are obtained. By using the folded atrous convolution, in the process of information transfer across convolution layers, more contexts are merged and the certain local correlation is also preserved, which provides the fault-tolerance capability for subsequent operations.

The Fold-ASPP is only equipped on the top of the encoder network, which consists of three folded atrous convolutional layers with dilation rates [2, 4, 6] to fit the size of feature maps. Just as group convolution [162] is a trade-off between depthwise convolution [21, 46] and vanilla convolution in the channel dimension, the proposed folded atrous convolution is a trade-off between atrous convolution and vanilla convolution in the spatial dimension.

3.4 Supervision

We use the pixel position aware loss L_{ppa} [151] which have been widely adopted in segmentation tasks. We use the same definitions as in [31, 151, 176, 202, 208]. As shown in Fig. 2, we apply supervision for both the intermediate prediction from the FPN branch and the final prediction from the dual branch. In the dual branch decoder, since the FPN branch gradually combines all-level gated encoding and decoding features, it has very powerful prediction ability. We expect that it can predict salient objects as accurately as possible under the supervision of ground truth. While the parallel branch only combines the gated encoding features, which is helpful to remedy the ignored details with the design of residual structure. Moreover, the

supervision on D^1 can drive gate units to learn the weight of the contribution of each encoder block to the final prediction. The total loss L could be written as:

$$L = L_{ppa}^{s1} + L_{ppa}^{sf}, \quad (6)$$

where L_{ppa}^{s1} and L_{ppa}^{sf} are respectively used to regularize the output of the FPN branch and the final prediction.

3.5 Two-Stream Network

To finish some two-source input tasks, *e.g.*, RGB-D salient object detection, we extend the GateNet to a two-stream architecture to further demonstrate its effectiveness. The proposed two-stream GateNet is shown in Fig. 7. Compared with the single-stream network for single source input tasks, there are two main differences: (1) We add an extra encoder to extract features of other modals. (2) We convey the output features from the encoding blocks of two modalities to the gate unit to achieve cross-modal fusion at each level. The motivation of embedding gate units when performing cross-modal fusion is straightforward, that is, different modalities present different characteristics in each layer of the encoder, and low-quality modal features can interfere with the other one, leading to build a poor decoder. The form and composition of all gate units are the same as Fig. 3 and Eq. 2 except that the input features are different.

4 Experiments

4.1 Datasets

For the training and test dataset, we follow the settings of the most state-of-the-art methods [63, 87, 91, 98, 135, 160, 168, 171, 197, 206] in Tab. 1 on each binary segmentation task. And the details about these datasets can find in Tab. 3.

4.2 Evaluation Metrics

There are ten popular metrics used in different binary segmentation branches. F-measure [1] (F_{β}^{max} , F_{β}^{mean}), weighted F-measure [95] (F_{β}^{ω}), S-measure [28] (S_m), E-measure [29] (E_m) and MAE [106] (\mathcal{M}) are widely used in salient object detection, camouflaged object detection

and defous blur detection tasks. IOU and Dice scores are popular with medical image segmentation. BER [137] and Pixel Accuracy (PA) are more commonly used for shadow, mirror, glass and transparent detection. The lower value is better for the BER and MAE, and higher is better for others.

- **Pixel Accuracy (PA)** is calculated based on the binarized prediction mask and ground-truth:

$$PA = \frac{TP + TN}{TP + TN + FP + FN}, \quad (7)$$

where TP, TN, FP, FN denote true-positive, true-negative, false-positive, and false-negative, respectively.

- **F-measure (F_{β})** [1] is a metric that comprehensively considers both precision and recall:

$$F_{\beta} = \frac{(1 + \beta^2) \text{Precision} \times \text{Recall}}{\beta^2 \text{Precision} + \text{Recall}}, \quad (8)$$

$$\text{Precision} = \frac{TP}{TP + FP}, \quad \text{Recall} = \frac{TP}{TP + FN}, \quad (9)$$

where β^2 is set to 0.3 as suggested in [1] to emphasize the precision. Some methods report the maximum F-measure (F_{β}^{max}) across the binary maps of different thresholds or the mean F-measure (F_{β}^{mean}) score by an adaptive threshold.

- **weighted F-measure (F_{β}^{ω})** [95] is proposed to improve the metric F-measure. It assigns different weights (ω) to precision and recall across different errors at different locations, considering the neighborhood information:

$$F_{\beta}^{\omega} = \frac{(1 + \beta^2) \text{Precision}^{\omega} \times \text{Recall}^{\omega}}{\beta^2 \text{Precision}^{\omega} + \text{Recall}^{\omega}}. \quad (10)$$

- **S-measure (S_m)** [28] evaluates the spatial structure similarity by combining the region-aware structural similarity S_r and the object-aware structural similarity S_o :

$$S_m = \alpha \times S_o + (1 - \alpha) \times S_r, \quad (11)$$

where α is empirically set to 0.5.

- **E-measure (E_m)** [29] can jointly capture image level statistics and local pixel matching information:

$$Q_S = \frac{1}{W \times H} \sum_{i=1}^W \sum_{j=1}^H \phi_S(i, j), \quad (12)$$

where ϕ_S is the enhanced alignment matrix, reflecting the correlation between prediction S and the ground truth G after subtracting their global means, respectively.

Table 3 Summary of essential characteristics about popular binary segmentation datasets.

Dataset	Year	Publication	#Image	Core Description	Role
RGB Salient Object Detection					
MSRA10K [19]	2015	TPAMI	10,000	Large scale; Multi-object	Train
ECSSD [106]	2015	CVPR	1,000	Semantically meaningful but structurally complex natural contents	Test
HKU-IS [75]	2015	CVPR	4,447	Multiple disconnected salient objects; Overlapping the image boundary	Test
PASCAL-S [77]	2014	CVPR	850	Selected from the PASCAL VOC2010 val set	Test
DUT-OMRON [107]	2013	CVPR	5,168	Complicated background and diverse content	Test
DUTS [142]	2017	CVPR	15,572	Large-scale; Complex scenarios with high-diversity contents; Most SOD models are typically trained on it	Train&Test
RGB-D Salient Object Detection					
NJUD [59]	2014	ICIP	1,985	Complex objects and challenging scenarios; Selected from 3D movies, the Internet, and photographs taken by a Fuji W3 stereo camera	Train&Test
NLPR [105]	2014	ECCV	1,000	There may exist multiple salient objects in each image; Captured by Kinect	Train&Test
DUTLF-D [107]	2019	ICCV	1,200	Contains 800 indoor and 400 outdoor scenes paired with the depth map and binary ground truth	Train&Test
STERE [100]	2012	CVPR	1,000	The first stereoscopic photo collection; Images downloaded from the Internet	Test
SIF [32]	2021	TNNLS	929	High-resolution images; Contain multiple salient persons per image	Test
SSD [213]	2017	ICCVW	80	Collected from three stereo movies	Test
RGB3D135 [20]	2014	ICIMCS	135	Consists of seven indoor scenes; Captured by Kinect	Test
LFSD [76]	2014	CVPR	100	Manly built for saliency detection on the light field	Test
ORSI Salient Object Detection					
ORSSD [70]	2019	TGRS	800	Diverse spatial resolution; Background is cluttered and complicated; Type of salient objects is various; The number and size of salient objects are variable	Train&Test
EORSSD [186]	2021	TIP	2,000	Multiple salient objects in one image; A number of small objects; More abundant scenarios; Imaging interferences; Specific circumstances	Train&Test
ORSI-4199 [135]	2021	TGRS	4,199	Large-scale; More challenges with background interference samples	Train&Test
Camouflaged Object Detection					
CHAMELEON [123]	2018	Unpublished Manuscript	76	The images were collected from the Internet via the Google search engine	Test
CAMO [66]	2019	CVIU	2,500	Eight categories	Train&Test
COD10k [30]	2020	CVPR	10,000	Large-scale; Broader size distribution; Global/Local contrast; Rich sub-classes; A large number of Full HD 1080p images	Train&Test
NC4k [93]	2021	CVPR	4,121	Large-scale; Evaluate the generalization ability of existing models	Test
Defocus Blur Detection					
CUHK [119]	2014	CVPR	704	Cluttered backgrounds and various scenes	Train&Test
DUT [199]	2018	CVPR	1,100	Multi-scale focused areas	Train&Test
Shadow Detection					
UCF [214]	2010	CVPR	245	Cluttered backgrounds and various scenes	Test
ISTD [141]	2018	CVPR	1,870	Both shadow detection and removal; Only 135 background scenes	Train&Test
SBU [138]	2016	ECCV	4,727	The largest shadow dataset covering general scenes; A wider variety of scenes	Train&Test
Transparent Object Detection					
Trans10K [160]	2020	ECCV	10,428	Two categories (stuff and things); Large-scale realworld images; Complex scenarios	Train&Test
Trans10K-v2 [161]	2021	IJCAI	10,428	Semantic Segmentation: 11 fine-grained glass image categories with a diverse scenario and high resolution	Train&Test
Glass Detection					
GDD [98]	2020	CVPR	3,916	Large-scale; Both indoor and outdoor scenes; Various types of common glass; Glass located at different positions of an image	Train&Test
Mirror Detection					
MSD [171]	2019	ICCV	4,018	Large-scale; Both indoor and outdoor scenes; Different mirror shapes and multiple mirrors; Low global color contrast	Train&Test
Polyp Segmentation					
CVC-ColonDB [127]	2015	TMI	380	Colonoscopy images each with a polyp inside; Selected from 15 short colonoscopy videos	Test
CVC-ClinicDB [5]	2015	CMIG	612	Images from 31 colonoscopy clip; Images of size 576 × 768	Train&Test
EndoScene [136]	2017	JHE	912	Images from CVC-ColonDB and CVC-ClinicDB and are reannotated; Extend the old annotations to account for lumen, and specular highlights	Train&Test
ETIS [120]	2014	IUCARS	196	An early established dataset for early diagnosis of colorectal cancer	Test
Kvasir [53]	2020	MMIM	1,000	Existing largest-scale dataset	Train&Test

- **IOU** is the most common metric for evaluating classification accuracy:

$$IOU = \frac{TP}{TP + FP + FN}. \quad (13)$$

- **Dice** is a statistic used to gauge the similarity of two samples and become the most used metric in validating medical image segmentation:

$$Dice = \frac{2TP}{FP + 2TP + FN}. \quad (14)$$

- **Balanced error rate (BER)** [137] is a common metric to evaluate shadow detection performance, where shadow and non-shadow regions contribute equally to the overall performance without considering their relative areas:

$$BER = (1 - \frac{1}{2}(\frac{TP}{TP + FN} + \frac{TN}{TN + FP})). \quad (15)$$

- **MAE (\mathcal{M})** [106] measures the average absolute difference between the prediction $\mathbf{S} \in [0, 1]^{W \times H}$ and the ground truth $\mathbf{G} \in \{0, 1\}^{W \times H}$ pixel by pixel:

$$MAE = \frac{1}{W \times H} \sum_{i=1}^W \sum_{j=1}^H |\mathbf{G}(i, j) - \mathbf{S}(i, j)|. \quad (16)$$

In fact, all above metrics can be used for any binary segmentation sub-task. In this paper, we are the first to introduce all ten metrics into the quantitative comparison to provide a comprehensive performance evaluation.

4.3 Implementation Details

We use the PyTorch framework to implement our models on one RTX 3090 GPU for 100 epochs. The input resolutions of images are resized to 352×352 and we employ a general multi-scale training strategy as most methods [17, 31, 93, 151, 202, 208]. We adopt some image augmentation techniques to avoid overfitting, including random flipping, rotating, and border clipping. For the optimizer, we use the Adam [64]. For the learning rate, initial learning rate is set to 0.0001. We adopt the “step” learning rate decay policy, and set the decay size as 30 and decay rate as 0.9. For any sub-tasks, the above training strategy is used for all the gated network models involved in this paper. The

Table 4 Quantitative comparison of different RGB SOD methods. Top 3 and Top 1 scores are highlighted in **blue** and **red**, respectively.

Metric	F3Net	ITSB	MINet	KRN	Auto-MSF	LDF	VST	CTDNet	GateNet
AAAI [151]	0.966	0.962	0.965	0.966	0.968	0.968	0.967	0.965	0.972
CVPR [207]	0.895	0.883	0.877	0.898	0.898	0.896	0.897	0.911	
ICCV [163]	0.840	0.804	0.828	0.856	0.851	0.855	0.818	0.853	0.857
ACMM [181]	0.845	0.824	0.834	0.847	0.845	0.845	0.828	0.844	
ICCV [202]	0.920	2020	2020	2021	2021	2020	2020	2021	—
Res-50	Res-50	Res-50	Res-50	Res-50	Res-50	T2T	Res-50	Res-50	Res-50
DUTS [142]									
F_A^+	0.966	0.962	0.965	0.966	0.968	0.968	0.967	0.965	0.972
$F_{\beta}^{max} \uparrow$	0.895	0.883	0.877	0.898	0.898	0.896	0.897	0.911	
$F_{\beta}^{mean} \uparrow$	0.840	0.804	0.828	0.856	0.851	0.855	0.818	0.853	0.857
F_S^+	0.845	0.824	0.834	0.847	0.845	0.845	0.828	0.844	
$S_m \uparrow$	0.918	0.918	0.918	0.917	0.917	0.926	0.916	0.928	0.931
$E_m \uparrow$	0.793	0.783	0.782	0.779	0.799	0.802	0.800	0.828	
$IOU \uparrow$	0.854	0.844	0.845	0.855	0.864	0.861	0.848	0.863	0.878
$Dice \uparrow$	0.854	0.844	0.845	0.855	0.864	0.861	0.848	0.863	0.878
$BER \downarrow$	0.065	0.065	0.065	0.067	0.072	0.064	0.064	0.060	0.052
$M \downarrow$	0.045	0.045	0.045	0.045	0.044	0.044	0.038	0.042	0.030
DUT-OMRON [167]									
F_A^+	0.940	0.942	0.946	0.951	0.953	0.950	0.946	0.949	0.952
$F_{\beta}^{max} \uparrow$	0.813	0.821	0.810	0.798	0.827	0.820	0.825	0.826	0.824
$F_{\beta}^{mean} \uparrow$	0.766	0.756	0.756	0.778	0.783	0.774	0.756	0.779	0.781
F_S^+	0.747	0.750	0.738	0.757	0.765	0.752	0.755	0.762	0.765
$S_m \uparrow$	0.837	0.839	0.832	0.831	0.845	0.838	0.849	0.842	0.847
$E_m \uparrow$	0.876	0.867	0.873	0.876	0.889	0.881	0.872	0.884	0.882
$IOU \uparrow$	0.710	0.715	0.699	0.705	0.723	0.711	0.731	0.720	0.730
$Dice \uparrow$	0.770	0.778	0.770	0.786	0.786	0.782	0.783	0.785	0.786
$BER \downarrow$	0.051	0.051	0.051	0.051	0.051	0.052	0.051	0.055	0.057
$M \downarrow$	0.053	0.061	0.056	0.050	0.049	0.052	0.058	0.052	0.050
ECSSD [168]									
F_A^+	0.969	0.969	0.969	0.969	0.967	0.967	0.968	0.973	0.970
$F_{\beta}^{max} \uparrow$	0.945	0.947	0.948	0.941	0.946	0.950	0.951	0.950	0.960
$F_{\beta}^{mean} \uparrow$	0.925	0.985	0.924	0.929	0.922	0.930	0.920	0.927	0.931
F_S^+	0.912	0.911	0.911	0.916	0.910	0.915	0.910	0.915	0.931
$S_m \uparrow$	0.924	0.925	0.925	0.914	0.923	0.932	0.922	0.925	0.941
$E_m \uparrow$	0.946	0.946	0.932	0.952	0.954	0.942	0.951	0.957	0.949
$IOU \uparrow$	0.879	0.879	0.879	0.871	0.876	0.878	0.876	0.881	0.885
$Dice \uparrow$	0.921	0.919	0.922	0.922	0.919	0.923	0.922	0.924	0.940
$BER \downarrow$	0.045	0.045	0.044	0.043	0.048	0.047	0.045	0.036	0.031
$M \downarrow$	0.033	0.035	0.034	0.033	0.036	0.034	0.034	0.033	0.026
HBU-IS [75]									
F_A^+	0.973	0.972	0.974	0.973	0.974	0.974	0.976	0.974	0.977
$F_{\beta}^{max} \uparrow$	0.910	0.938	0.914	0.914	0.915	0.915	0.901	0.947	0.948
$F_{\beta}^{mean} \uparrow$	0.891	0.890	0.890	0.904	0.902	0.905	0.898	0.908	0.916
F_S^+	0.916	0.916	0.916	0.908	0.918	0.920	0.928	0.930	0.931
$S_m \uparrow$	0.959	0.953	0.961	0.960	0.960	0.962	0.961	0.962	0.965
$E_m \uparrow$	0.862	0.857	0.862	0.853	0.863	0.867	0.877	0.869	0.886
$IOU \uparrow$	0.910	0.904	0.910	0.912	0.911	0.915	0.911	0.917	0.925
$Dice \uparrow$	0.908	0.898	0.908	0.904	0.905	0.904	0.908	0.905	0.937
$BER \downarrow$	0.028	0.031	0.028	0.029	0.029	0.027	0.028	0.026	0.025
$M \downarrow$	0.064	0.066	0.066	0.063	0.070	0.062	0.062	0.064	0.055
PASCAL-S [77]									
F_A^+	0.929	0.929	0.929	0.929	0.929	0.929	0.928	0.930	0.927
$F_{\beta}^{max} \uparrow$	0.882	0.882	0.880	0.874	0.886	0.887	0.890	0.889	0.900
$F_{\beta}^{mean} \uparrow$	0.844	0.797	0.840	0.854	0.842	0.853	0.841	0.848	
F_S^+	0.823	0.823	0.818	0.830	0.823	0.829	0.827	0.829	0.846
$S_m \uparrow$	0.857	0.859	0.854	0.849	0.854	0.859	0.871	0.859	0.875
$E_m \uparrow$	0.895	0.866	0.897	0.902	0.881	0.903	0.905	0.909	0.902
$IOU \uparrow$	0.780	0.782	0.773	0.775	0.773	0.783	0.801	0.783	0.808
$Dice \uparrow$	0.907	0.907	0.907	0.907	0.907	0.907	0.907	0.907	0.907
$BER \downarrow$	0.080	0.078	0.084	0.085	0.081	0.086	0.078	0.078	0.065
$M \downarrow$	0.064	0.066	0.066	0.063	0.070	0.062	0.062	0.064	0.055
Top 3	5/50	5/50	6/50	15/50	18/50	28/50	30/50	37/50	49/50
Top 1	0/50	0/50	0/50	1/50	5/50	0/50	3/50	1/50	40/50

difference among these models is only in the mini-batch size due to adopting different backbones. Specifically, the mini-batch size settings in the gatenet using VGG-16, ResNet-50, Res2Net-50, and ResNeXt-101 as the backbone are 8, 24, 24 and 16, respectively. The source code can be available at <https://github.com/Xiaoqi-Zhao-DLUT/GateNet-RGB-Saliency>.

4.4 Performance

We compare our models with state-of-the-art approaches in terms of ten metrics on all test sets corresponding for each binary segmentation task in Tab. 4 - Tab. 11. Since there are many test sets for RGB SOD, RGB-D SOD and polyp segmentation, we not only compare the performance under each metric, but also count the proportion of top 3 and top 1 performance to get an overall evaluation. Some quantitative analyses are as follows:

- In Tab. 4, among 50 scores of all **RGB SOD** datasets, our GateNet achieves significant performance improvement compared to the second best method CTDNet [205] in terms of top 3 (49/50

Table 5 Quantitative comparison of different polyp segmentation methods. Top 3 and Top 1 scores are highlighted in **blue** and **red**, respectively.

Metric	UNet	UNet++	SEA	PrnNet	SANet	MSNet	UACANet	GateNet
MICCAI [11]	0.979	0.984	0.936	0.990	0.993	0.990	0.995	0.993
2015 [211]	0.805	0.817	0.558	0.905	0.881	0.899	0.924	
TMI [36]	0.706	0.353	0.824	0.829	0.885	0.867		
2019 [19]	0.824	0.823	0.824	0.829	0.927	0.929	0.933	
2020 [150]	0.821	0.820	0.821	0.822	0.924	0.922	0.931	
Res-250 [202]	0.805	0.804	0.805	0.806	0.924	0.922	0.931	
Res-50 [205]	0.802	0.801	0.802	0.803	0.924	0.922	0.931	
Res-250 [205]	0.801	0.800	0.801	0.802	0.924	0.922	0.931	
Res-50 [205]	0.800	0.800	0.801	0.802	0.924	0.922	0.931	
Res-250 [205]	0.799	0.798	0.799	0.800	0.924	0.922	0.931	
Res-50 [205]	0.798	0.797	0.798	0.799	0.924	0.922	0.931	
Res-250 [205]	0.797	0.796	0.797	0.798	0.924	0.922	0.931	
Res-50 [205]	0.796	0.795	0.796	0.797	0.924	0.922	0.931	
Res-250 [205]	0.795	0.794	0.795	0.796	0.924	0.922	0.931	
Res-50 [205]	0.794	0.793	0.794	0.795	0.924	0.922	0.931	
Res-250 [205]	0.793	0.792	0.793	0.794	0.924	0.922	0.931	
Res-50 [205]	0.792	0.791	0.792	0.793	0.924	0.922	0.931	
Res-250 [205]	0.791	0.790	0.791	0.792	0.924	0.922	0.931	
Res-50 [205]	0.790	0.789	0.790	0.791	0.924	0.922	0.931	
Res-250 [205]	0.789	0.788	0.789	0.790	0.924	0.922	0.931	
Res-50 [205]	0.788	0.787	0.788	0.789	0.924	0.922	0.931	
Res-250 [205]	0.787	0.786	0.787	0.788	0.924	0.922	0.931	
Res-50 [205]	0.786	0.785	0.786	0.787	0.924	0.922	0.931	
Res-250 [205]	0.785	0.784	0.785	0.786	0.924	0.922	0.931	
Res-50 [205]	0.784	0.783	0.784	0.785	0.924	0.922	0.931	
Res-250 [205]	0.783	0.782	0.783	0.784	0.924	0.922	0.931	
Res-50 [205]	0.782	0.781	0.782	0.783	0.924	0.922	0.931	
Res-250 [205]	0.781	0.780	0.781	0.782	0.924	0.922	0.931	
Res-50 [205]	0.780	0.779	0.780	0.781	0.924	0.922	0.931	
Res-250 [205]	0.779	0.778	0.779	0.780	0.924	0.922	0.931	
Res-50 [205]	0.778	0.777	0.778	0.779	0.924	0.922	0.931	
Res-250 [205]	0.777	0.776	0.777	0.778	0.924	0.922	0.931	
Res-50 [205]	0.776	0.775	0.776	0.777	0.924	0.922	0.931	
Res-250 [205]	0.775	0.774	0.775	0.776	0.924	0.922	0.931	
Res-50 [205]	0.774	0.773	0.774	0.775	0.924	0.922	0.931	
Res-250 [205]	0.773	0.772	0.773	0.774	0.924	0.922	0.931	
Res-50 [205]	0.772	0.771	0.772	0.773	0.924	0.922	0.931	
Res-250 [205]	0.771	0.770	0.771	0.772	0.924			

Table 6 Quantitative comparison of different RGB-D SOD methods. Top 3 and Top 1 scores are highlighted in blue and red, respectively.

Metric	DCF	RD3D	UTA	DSNet	SPNet	TriTrans	GateNet	GateNet
	[55]	[13]	[204]	[153]	[208]	[91]	—	—
CVPR	AAAI	TIP	TIP	ICCV	ACMMM	—	—	—
2021	2021	2021	2021	2021	2021	—	—	—
Res-50	Res-50	Res-50	Res-50	Res2-50	Res-50	Res-50	Res-50	Res2-50
<i>DTU RGB-D [40]</i>								
$PA \uparrow$	—	0.973	—	—	—	0.975	0.977	0.977
$F_B^{\max} \uparrow$	—	0.946	—	—	—	0.951	0.958	0.957
$F_B^{\text{mean}} \uparrow$	—	0.924	—	—	—	0.938	0.946	0.944
$F_B^{\omega} \uparrow$	—	0.909	—	—	—	0.926	0.931	0.931
$S_m \uparrow$	—	0.931	—	—	—	0.932	0.943	0.943
$E_m \uparrow$	—	0.957	—	—	—	0.966	0.969	0.967
$IOU \uparrow$	—	0.888	—	—	—	0.893	0.909	0.909
$Dice \uparrow$	—	0.922	—	—	—	0.937	0.940	0.940
$BER \downarrow$	—	0.039	—	—	—	0.036	0.033	0.032
$\mathcal{M} \downarrow$	—	0.031	—	—	—	0.025	0.025	0.025
<i>NUSD [50]</i>								
$PA \uparrow$	0.963	0.966	0.963	0.969	0.973	0.970	0.975	0.974
$F_B^{\max} \uparrow$	0.917	0.923	0.915	0.930	0.935	0.934	0.943	0.936
$F_B^{\text{mean}} \uparrow$	0.897	0.901	0.903	0.907	0.917	0.920	0.928	0.920
$F_B^{\omega} \uparrow$	0.878	0.888	0.883	0.893	0.906	0.906	0.913	0.908
$S_m \uparrow$	0.903	0.916	0.902	0.921	0.924	0.920	0.931	0.930
$E_m \uparrow$	0.941	0.942	0.946	0.947	0.953	0.954	0.956	0.953
$IOU \uparrow$	0.841	0.862	0.847	0.870	0.879	0.871	0.888	0.885
$Dice \uparrow$	0.895	0.903	0.901	0.909	0.921	0.920	0.924	0.922
$BER \downarrow$	0.058	0.047	0.056	0.047	0.040	0.042	0.041	0.040
$\mathcal{M} \downarrow$	0.038	0.037	0.037	0.034	0.029	0.030	0.028	0.028
<i>NLPR [65]</i>								
$PA \uparrow$	0.978	0.980	0.980	0.978	0.980	0.980	0.978	0.981
$F_B^{\max} \uparrow$	0.917	0.927	0.932	0.928	0.926	0.929	0.936	0.937
$F_B^{\text{mean}} \uparrow$	0.892	0.892	0.918	0.886	0.904	0.910	0.911	0.911
$F_B^{\omega} \uparrow$	0.886	0.889	0.905	0.881	0.896	0.902	0.902	0.906
$S_m \uparrow$	0.921	0.929	0.928	0.926	0.927	0.928	0.933	0.938
$E_m \uparrow$	0.956	0.959	0.965	0.957	0.959	0.964	0.962	0.966
$IOU \uparrow$	0.849	0.862	0.866	0.855	0.861	0.864	0.873	0.878
$Dice \uparrow$	0.901	0.906	0.918	0.900	0.913	0.917	0.915	0.921
$BER \downarrow$	0.047	0.040	0.042	0.043	0.037	0.038	0.040	0.037
$\mathcal{M} \downarrow$	0.023	0.022	0.020	0.024	0.021	0.020	0.023	0.020
<i>STERE [100]</i>								
$PA \uparrow$	0.965	0.965	0.966	0.967	0.965	0.967	0.970	0.970
$F_B^{\max} \uparrow$	0.915	0.917	0.921	0.924	0.915	0.919	0.929	0.929
$F_B^{\text{mean}} \uparrow$	0.890	0.886	0.905	0.894	0.888	0.893	0.907	0.903
$F_B^{\omega} \uparrow$	0.873	0.871	0.887	0.876	0.873	0.882	0.889	0.888
$S_m \uparrow$	0.905	0.911	0.910	0.915	0.907	0.908	0.921	0.919
$E_m \uparrow$	0.943	0.944	0.949	0.947	0.942	0.950	0.952	0.950
$IOU \uparrow$	0.837	0.848	0.853	0.851	0.841	0.848	0.862	0.861
$Dice \uparrow$	0.896	0.899	0.909	0.909	0.899	0.907	0.909	0.909
$BER \downarrow$	0.051	0.044	0.046	0.048	0.046	0.041	0.043	0.042
$\mathcal{M} \downarrow$	0.037	0.037	0.036	0.036	0.037	0.033	0.032	0.033
<i>SIP [23]</i>								
$PA \uparrow$	0.950	0.954	0.952	0.951	0.958	0.957	0.963	0.958
$F_B^{\max} \uparrow$	0.900	0.906	0.896	0.902	0.916	0.916	0.927	0.921
$F_B^{\text{mean}} \uparrow$	0.877	0.874	0.872	0.865	0.893	0.892	0.902	0.898
$F_B^{\omega} \uparrow$	0.841	0.845	0.843	0.832	0.868	0.864	0.877	0.868
$S_m \uparrow$	0.873	0.885	0.873	0.876	0.894	0.886	0.903	0.894
$E_m \uparrow$	0.921	0.924	0.927	0.920	0.931	0.929	0.939	0.931
$IOU \uparrow$	0.786	0.800	0.797	0.793	0.824	0.815	0.840	0.822
$Dice \uparrow$	0.859	0.860	0.870	0.856	0.886	0.880	0.894	0.881
$BER \downarrow$	0.085	0.068	0.072	0.078	0.063	0.070	0.058	0.070
$\mathcal{M} \downarrow$	0.052	0.048	0.048	0.052	0.043	0.043	0.038	0.044
<i>RGBD135 [20]</i>								
$PA \uparrow$	0.978	0.982	0.975	0.980	0.986	0.986	0.985	0.985
$F_B^{\max} \uparrow$	0.926	0.941	0.921	0.939	0.950	0.946	0.951	0.950
$F_B^{\text{mean}} \uparrow$	0.901	0.917	0.891	0.910	0.935	0.936	0.931	0.931
$F_B^{\omega} \uparrow$	0.876	0.904	0.864	0.893	0.931	0.929	0.922	0.922
$S_m \uparrow$	0.916	0.938	0.901	0.928	0.945	0.943	0.941	0.941
$E_m \uparrow$	0.958	0.975	0.935	0.970	0.983	0.981	0.978	0.980
$IOU \uparrow$	0.823	0.860	0.808	0.846	0.888	0.884	0.878	0.876
$Dice \uparrow$	0.887	0.912	0.874	0.902	0.938	0.935	0.928	0.928
$BER \downarrow$	0.065	0.050	0.071	0.058	0.033	0.035	0.041	0.042
$\mathcal{M} \downarrow$	0.023	0.019	0.026	0.021	0.014	0.014	0.016	0.016
<i>SSD [213]</i>								
$PA \uparrow$	0.948	0.924	0.952	0.959	0.957	0.960	0.957	0.959
$F_B^{\max} \uparrow$	0.857	0.805	0.860	0.895	0.883	0.889	0.876	0.891
$F_B^{\text{mean}} \uparrow$	0.828	0.749	0.838	0.853	0.855	0.865	0.853	0.859
$F_B^{\omega} \uparrow$	0.790	0.707	0.799	0.829	0.823	0.842	0.824	0.834
$S_m \uparrow$	0.852	0.803	0.852	0.885	0.871	0.881	0.881	0.883
$E_m \uparrow$	0.906	0.863	0.901	0.923	0.920	0.935	0.923	0.923
$IOU \uparrow$	0.746	0.674	0.749	0.801	0.783	0.802	0.796	0.804
$Dice \uparrow$	0.813	0.737	0.822	0.852	0.852	0.862	0.849	0.861
$BER \downarrow$	0.102	0.143	0.101	0.076	0.075	0.075	0.074	0.068
$\mathcal{M} \downarrow$	0.053	0.082	0.049	0.045	0.044	0.041	0.044	0.043
<i>LFSD [76]</i>								
$PA \uparrow$	0.931	0.929	0.911	0.935	0.931	0.935	0.945	0.943
$F_B^{\max} \uparrow$	0.878	0.879	0.856	0.884	0.881	0.890	0.891	0.904
$F_B^{\text{mean}} \uparrow$	0.857	0.855	0.832	0.864	0.860	0.861	0.878	0.883
$F_B^{\omega} \uparrow$	0.824	0.816	0.797	0.823	0.823	0.840	0.841	0.849
$S_m \uparrow$	0.856	0.858	0.830	0.868	0.854	0.861	0.879	0.881
$E_m \uparrow$	0.903	0.898	0.878	0.905	0.897	0.908	0.917	0.913
$IOU \uparrow$	0.777	0.779	0.748	0.790	0.766	0.797	0.804	0.806
$Dice \uparrow$	0.849	0.849	0.832	0.854	0.847	0.865	0.865	0.871
$BER \downarrow$	0.081	0.074	0.090	0.069	0.083	0.072	0.067	0.068
$\mathcal{M} \downarrow$	0.071	0.073	0.089	0.069	0.071	0.066	0.058	0.059
Top 3	1/70	7/80	16/70	17/70	39/70	61/80	71/80	77/80
Top 1	0/80	0/80	2/70	2/70	10/70	11/80	43/80	32/80

methods, respectively. Without too much claim, our models achieve the best performance in terms of all ten metrics across 16 out of 17 different datasets.

• Tab. 12 lists the *model sizes, parameters, FLOPs and speed* of different methods with superior performance in Tab. 4 - Tab. 11 in detail. It can be seen that both two-stream and single stream GateNets still have obvious advantages against most state-of-the-art methods with different backbones.

4.5 Ablation Studies

To reflect the general contribution of each component to the overall performance, we conduct ablation studies on the largest dataset for each sub-task individually. Tab. 13 and Tab. 14 are the results for single-input tasks and the two-input task (RGB-D SOD), respectively. Tab. 15 verifies the effect of folded atrous convolution thoroughly.

• **Dual Branch Decoder.** The baseline (M1) is a FPN structure with a progressive decoder. We add the residual parallel branch to construct the dual branch decoder. We can see that M2 consistently outperforms M1 across all datasets in terms of all ten metrics. Meanwhile, M2 has been able to surpass SINet [30], PFNet [97], IS2CNet [191] and BDRAR [215]. Based on this strong dual branch network, the subsequent performance gain of gate units and fold atrous convolution is more convincing.

• **Gate Units.** We embed multi-level gate units in both the FPN and parallel branches. In Tab. 13, the M3 achieves a significant improvement compared to the M4 indicates the necessity of designing gate units-v2 with a global information perspective. Further, the performance gap between M2 and M4 shows that the dual branch gated network obtains a considerable performance gain. In Tab. 14, M3 vs. M2 and M4 vs. M3 demonstrate the effectiveness of gate units in cross-modal fusion and encoder-decoder feature transition, respectively. In addition, the curves of gate value on each dataset in ten tasks as shown in Fig. 8. Through the characteristics of the gated pattern, we reveal some insightful findings: **I)** For the distribution of gate values at all levels in the FPN branch, Fig. 8(a), (b), (e), (f), (g) present G1 and G2 are smaller than G3, G4, G5, while G1 in Fig. 8(c), (d), (h) has the opposite trend. Analyzed from the visual perception, camouflaged objects, orsi object and polyps are easy to be confused with the background. The boundary information

Table 7 Quantitative comparison of different camouflaged object methods. The best scores are highlighted in red.

Dataset	Method	Pub.	Backbone	$PA \uparrow$	$F_{\beta}^{max} \uparrow$	$F_{\beta}^{mean} \uparrow$	$F_{\beta}^{\omega} \uparrow$	$S_m \uparrow$	$E_m \uparrow$	$IOU \uparrow$	$Dice \uparrow$	$BER \downarrow$	$\mathcal{M} \downarrow$
CAMO [66]	SiNet [30]	CVPR 2020	ResNet-50	0.907	0.762	0.709	0.606	0.751	0.835	0.546	0.639	0.201	0.100
	PFNet [97]	CVPR 2021	ResNet-50	0.917	0.795	0.751	0.695	0.782	0.855	0.624	0.725	0.150	0.085
	RankNet [93]	CVPR 2021	ResNet-50	0.922	0.791	0.756	0.696	0.787	0.859	0.626	0.722	0.154	0.080
	MGL [174]	CVPR 2021	ResNet-50	0.914	0.792	0.738	0.673	0.775	0.848	0.605	0.699	0.172	0.088
	UGTR [168]	ICCV 2021	ResNet-50	0.918	0.800	0.748	0.684	0.784	0.858	0.618	0.712	0.161	0.086
	GateNet	—	ResNet-50	0.934	0.835	0.804	0.756	0.829	0.888	0.694	0.781	0.122	0.069
CHAMELEON [123]	SiNet [30]	CVPR 2020	ResNet-50	0.965	0.846	0.776	0.740	0.869	0.899	0.726	0.776	0.107	0.044
	PFNet [97]	CVPR 2021	ResNet-50	0.970	0.860	0.820	0.810	0.882	0.942	0.769	0.835	0.077	0.033
	RankNet [93]	CVPR 2021	ResNet-50	0.972	0.866	0.835	0.822	0.890	0.936	0.776	0.844	0.077	0.031
	MGL [174]	CVPR 2021	ResNet-50	0.973	0.868	0.826	0.813	0.893	0.923	0.781	0.832	0.082	0.030
	UGTR [168]	ICCV 2021	ResNet-50	0.974	0.863	0.805	0.794	0.887	0.921	0.761	0.816	0.093	0.031
	GateNet	—	ResNet-50	0.977	0.902	0.858	0.855	0.910	0.951	0.821	0.872	0.060	0.026
COD10K [30]	SiNet [30]	CVPR 2020	ResNet-50	0.957	0.708	0.593	0.551	0.770	0.797	0.532	0.602	0.191	0.051
	PFNet [97]	CVPR 2021	ResNet-50	0.962	0.748	0.676	0.660	0.798	0.868	0.602	0.700	0.136	0.040
	RankNet [93]	CVPR 2021	ResNet-50	0.965	0.756	0.699	0.673	0.802	0.883	0.609	0.705	0.144	0.037
	MGL [174]	CVPR 2021	ResNet-50	0.968	0.770	0.681	0.666	0.811	0.865	0.617	0.695	0.154	0.035
	UGTR [168]	ICCV 2021	ResNet-50	0.968	0.772	0.671	0.666	0.815	0.850	0.620	0.697	0.150	0.036
	GateNet	—	ResNet-50	0.974	0.823	0.752	0.742	0.846	0.901	0.689	0.768	0.114	0.028
NC4K [93]	SiNet [30]	CVPR 2020	ResNet-50	0.943	0.805	0.768	0.723	0.807	0.883	0.646	0.745	0.141	0.058
	PFNet [97]	CVPR 2021	ResNet-50	0.949	0.821	0.779	0.745	0.828	0.894	0.683	0.773	0.117	0.053
	RankNet [93]	CVPR 2021	ResNet-50	0.954	0.836	0.802	0.766	0.839	0.904	0.700	0.785	0.118	0.048
	MGL [174]	CVPR 2021	ResNet-50	0.951	0.830	0.778	0.740	0.832	0.890	0.682	0.761	0.129	0.053
	UGTR [168]	ICCV 2021	ResNet-50	0.952	0.833	0.778	0.747	0.839	0.888	0.694	0.770	0.120	0.052
	GateNet	—	ResNet-50	0.963	0.872	0.832	0.806	0.869	0.918	0.751	0.824	0.094	0.040

Table 8 Quantitative comparison of different defocus blur detection methods. The best scores are highlighted in red.

Dataset	Method	Pub.	Backbone	$PA \uparrow$	$F_{\beta}^{max} \uparrow$	$F_{\beta}^{mean} \uparrow$	$F_{\beta}^{\omega} \uparrow$	$S_m \uparrow$	$E_m \uparrow$	$IOU \uparrow$	$Dice \uparrow$	$BER \downarrow$	$\mathcal{M} \downarrow$
CUHK [119]	CENet [200]	CVPR 2019	VGG-16	0.942	0.914	0.873	0.867	0.873	0.894	0.804	0.877	0.081	0.060
	Depth-Distill [23]	ECCV 2020	VGG-16	0.955	0.924	0.848	0.881	0.891	0.898	0.845	0.904	0.052	0.049
	SG [198]	CVPR 2021	VGG-16	0.881	0.820	0.641	0.737	0.762	0.749	0.673	0.788	0.123	0.123
	IS2CNet [191]	TCSVT 2021	VGG-16	0.939	0.917	0.899	0.862	0.863	0.909	0.799	0.872	0.085	0.063
	DENet [197]	TIP 2021	VGG-16	0.953	0.931	0.881	0.882	0.887	0.909	0.837	0.890	0.068	0.055
	GateNet	—	VGG-16	0.963	0.935	0.920	0.903	0.906	0.941	0.869	0.919	0.046	0.040
DUT [199]	CENet [200]	CVPR 19	VGG-16	0.867	0.826	0.767	0.697	0.742	0.775	0.609	0.703	0.185	0.136
	Depth-Distill [23]	ECCV 2020	VGG-16	0.890	0.860	0.813	0.766	0.787	0.828	0.677	0.780	0.143	0.113
	SG [198]	CVPR 2021	VGG-16	0.827	0.749	0.629	0.612	0.663	0.718	0.522	0.650	0.210	0.175
	IS2CNet [191]	TCSVT 2021	VGG-16	0.865	0.827	0.784	0.699	0.731	0.788	0.601	0.710	0.188	0.136
	DENet [197]	TIP 2021	VGG-16	0.910	0.876	0.807	0.799	0.814	0.837	0.735	0.814	0.115	0.096
	GateNet	—	VGG-16	0.939	0.905	0.887	0.861	0.862	0.908	0.816	0.882	0.072	0.064

Table 9 Quantitative comparison of different shadow detection methods. The best scores are highlighted in red.

Dataset	Method	Pub.	Backbone	$PA \uparrow$	$F_{\beta}^{max} \uparrow$	$F_{\beta}^{mean} \uparrow$	$F_{\beta}^{\omega} \uparrow$	$S_m \uparrow$	$E_m \uparrow$	$IOU \uparrow$	$Dice \uparrow$	$BER \downarrow$	$\mathcal{M} \downarrow$
SBU [138]	DSC [50]	CVPR 2018	VGG-16	0.969	0.914	0.892	0.861	0.856	0.939	0.801	0.871	0.081	0.032
	ADNet [65]	ECCV 2018	—	0.951	0.877	0.696	0.424	0.700	0.811	0.747	0.539	0.074	0.201
	BDRAR [215]	ECCV 2018	ResNeXt-101	0.961	0.884	0.830	0.827	0.844	0.930	0.784	0.863	0.052	0.039
	DSD [206]	CVPR 2019	ResNeXt-101	0.965	0.896	0.841	0.835	0.851	0.933	0.797	0.873	0.046	0.036
	GateNet	—	ResNeXt-101	0.978	0.937	0.903	0.889	0.886	0.957	0.848	0.899	0.059	0.025
	DSC [50]	CVPR 18	VGG-16	0.947	0.806	0.772	0.737	0.788	0.897	0.675	0.770	0.121	0.054
UCF [214]	ADNet [65]	ECCV 18	—	0.916	0.783	0.575	0.371	0.647	0.748	0.611	0.483	0.110	0.229
	BDRAR [215]	ECCV 18	ResNeXt-101	0.927	0.819	0.613	0.644	0.763	0.765	0.630	0.723	0.079	0.080
	DSD [206]	CVPR 19	ResNeXt-101	0.938	0.791	0.726	0.710	0.779	0.862	0.667	0.775	0.079	0.063
	GateNet	—	ResNeXt-101	0.954	0.865	0.800	0.777	0.821	0.907	0.723	0.812	0.093	0.048
	BDRAR [215]	ECCV 18	ResNeXt-101	0.973	0.910	0.880	0.878	0.901	0.946	0.856	0.906	0.026	0.027
	DSD [206]	CVPR 19	ResNeXt-101	0.980	0.933	0.919	0.897	0.930	0.961	0.883	0.912	0.040	0.023

Table 10 Quantitative comparison of different transparent, glass and mirror detection methods. The best scores are highlighted in red.

Transparent Object Detection													
Dataset	Method	Pub.	Backbone	$PA \uparrow$	$F_{\beta}^{max} \uparrow$	$F_{\beta}^{mean} \uparrow$	$F_{\beta}^{\omega} \uparrow$	$S_m \uparrow$	$E_m \uparrow$	$IOU \uparrow$	$Dice \uparrow$	$BER \downarrow$	$\mathcal{M} \downarrow$
Transparent-Easy [160]	Translab [160]	ECCV 2020	ResNet-50	0.978	0.955	0.953	0.941	0.935	0.974	0.921	0.957	0.027	0.022
Transparent-Hard [160]	Translab [160]	ECCV 2020	ResNet-50	0.913	0.843	0.827	0.783	0.798	0.871	0.733	0.827	0.110	0.087
Transparent-All [160]	Translab [160]	ECCV 2020	ResNet-50	0.964	0.931	0.927	0.907	0.906	0.952	0.881	0.929	0.044	0.036
Glass Detection													
GDD [98]	GDNet [98]	CVPR 2020	ResNeXt-101	0.939	0.927	0.920	0.901	0.864	0.919	0.876	0.924	0.056	0.061
	EBLNet [43]	ICCV 2021	ResNeXt-101	0.944	0.937	0.929	0.875	0.875	0.925	0.882	0.928	0.054	0.056
	GateNet	—	ResNeXt-101	0.951	0.944	0.937	0.921	0.892	0.933	0.898	0.935	0.049	0.049
Mirror Detection													
MSD [171]	MirrorNet [?]	ICCV 19	ResNeXt-101	0.934	0.857	0.777	0.744	0.846	0.861	0.785	0.806	0.065	0.085
	GateNet	—	ResNeXt-101	0.949	0.865	0.839	0.829	0.872	0.907	0.811	0.849	0.077	0.053

Table 11 Quantitative comparison of different ORSI SOD methods. The best scores are highlighted in red.

Dataset	Method	Pub.	Backbone	$PA \uparrow$	$F_{\beta}^{max} \uparrow$	$F_{\beta}^{mean} \uparrow$	$F_{\beta}^{\omega} \uparrow$	$S_m \uparrow$	$E_m \uparrow$	$IOU \uparrow$	$Dice \uparrow$	$BER \downarrow$	$\mathcal{M} \downarrow$
ORSSD [70]	DAFNet [186]	TIP 2020	VGG-16	0.990	0.903	0.788	0.844	0.912	0.920	0.823	0.874	0.059	0.011
	MJRBMB [135]	TGRS 2021	VGG-16	0.986	0.893	0.802	0.844	0.910	0.934	0.817	0.853	0.066	0.016
	GateNet	–	VGG-16	0.990	0.914	0.847	0.875	0.925	0.959	0.839	0.885	0.048	0.011
EORSSD [186]	DAFNet [186]	TIP 2020	VGG-16	0.996	0.867	0.642	0.783	0.883	0.815	0.800	0.830	0.051	0.006
	MJRBMB [135]	TGRS 2021	VGG-16	0.992	0.877	0.707	0.813	0.879	0.890	0.793	0.822	0.070	0.010
	RRNet [22]	TGRS 2021	Res2Net-50	0.994	0.887	0.725	0.827	0.885	0.873	0.834	0.862	0.067	0.008
	GateNet	–	VGG-16	0.993	0.896	0.799	0.859	0.894	0.915	0.850	0.892	0.057	0.008
ORSI-4199 [135]	MJRBMB [135]	TGRS 2021	VGG-16	0.965	0.867	0.800	0.806	0.853	0.909	0.747	0.813	0.103	0.037
	GateNet	–	VGG-16	0.969	0.883	0.853	0.840	0.864	0.935	0.767	0.839	0.095	0.032

Table 12 Efficiency comparisons of the top-performing methods in Tab. 4 - Tab. 11. The best and worst results are shown in red and blue, respectively.

Model Name	TriTrans ^T [91]	SPNet ^T [208]	GateNet ^T	EBLNet	GDNet	MirrorNet	DSDNet	GateNet	UACANet	GateNet	UGTR	MGL	Translab	CTDNet	GateNet	MJRBMB GateNet [135]	
Backbone	Res-50	Res-2-50	Res-50	ResX-101	ResX-101	ResX-101	ResX-101	ResX-101	Res-2-50	Res-50	Res-50	Res-50	Res-50	Res-50	Res-50	VGG-16 VGG-16	
Model Size (MB)↓	559	702	254	845	770	465	414	373	278	211	296	435	162	94	119	175	78
Parameters (MB)↓	139.55	175.29	81.55	111.45	201.72	121.77	58.16	92.89	69.16	52.51	48.87	63.60	42.20	21.93	29.68	43.78	20.43
FLOPs (G)↓	680.07	135.86	63.30	674.41	244.21	111.92	54.34	94.18	119.60	74.16	358.53	475.40	284.68	21.43	64.24	191.46	131.01
Speed (FPS)↑	16	22	35	16	23	25	49	38	34	35	24	18	22	133	55	35	36

Table 13 Ablation experiments for seven binary segmentation tasks. M1: FPN Baseline. M2: + Residual Parallel Branch. M3: + Gate Units v1. M4: + Gate Units v2. M5: + Fold-ASPP.

Dataset	Method	$PA \uparrow$	$F_{\beta}^{max} \uparrow$	$F_{\beta}^{mean} \uparrow$	$F_{\beta}^{\omega} \uparrow$	$S_m \uparrow$	$E_m \uparrow$	$IOU \uparrow$	$Dice \uparrow$	$BER \downarrow$	$AM \downarrow$	$\Delta \text{ gains}$
DUTS [142]	M1	0.968	0.870	0.801	0.809	0.870	0.888	0.763	0.820	0.102	0.045	
	M2	0.962	0.875	0.810	0.808	0.875	0.894	0.775	0.830	0.095	0.043	1.85%
	M3	0.967	0.888	0.835	0.830	0.886	0.906	0.795	0.844	0.082	0.038	7.70%
	M4	0.970	0.895	0.842	0.836	0.889	0.914	0.807	0.856	0.071	0.035	78.26%
	M5	0.972	0.911	0.857	0.864	0.906	0.931	0.828	0.878	0.052	0.030	12.91%
Kvasir [53]	M1	0.967	0.890	0.807	0.806	0.870	0.890	0.760	0.820	0.105	0.045	
	M2	0.968	0.914	0.805	0.809	0.876	0.915	0.791	0.845	0.101	0.045	3.52%
	M3	0.969	0.925	0.887	0.874	0.890	0.932	0.820	0.873	0.089	0.034	78.54%
	M4	0.968	0.929	0.897	0.889	0.902	0.940	0.832	0.884	0.078	0.031	11.09%
	M5	0.970	0.937	0.916	0.903	0.921	0.958	0.864	0.912	0.052	0.024	16.37%
COD10K [30]	M1	0.965	0.781	0.685	0.668	0.897	0.840	0.605	0.685	0.167	0.042	
	M2	0.970	0.796	0.696	0.681	0.891	0.852	0.612	0.696	0.170	0.042	2.66%
	M3	0.972	0.805	0.722	0.708	0.874	0.848	0.624	0.711	0.141	0.037	76.32%
	M4	0.972	0.810	0.730	0.717	0.882	0.881	0.660	0.731	0.130	0.037	78.84%
	M5	0.974	0.823	0.752	0.742	0.874	0.901	0.689	0.768	0.114	0.026	12.99%
DUT [199]	M1	0.905	0.860	0.800	0.784	0.808	0.776	0.686	0.776	0.157	0.116	
	M2	0.911	0.868	0.818	0.808	0.891	0.824	0.714	0.794	0.143	0.109	3.91%
	M3	0.930	0.890	0.869	0.858	0.882	0.871	0.775	0.848	0.102	0.079	7.25%
	M4	0.930	0.895	0.887	0.874	0.886	0.892	0.781	0.859	0.102	0.079	12.34%
	M5	0.939	0.905	0.887	0.861	0.898	0.908	0.816	0.882	0.072	0.064	118.29%
SBU [138]	M1	0.961	0.880	0.836	0.820	0.840	0.920	0.774	0.857	0.099	0.041	
	M2	0.964	0.892	0.852	0.841	0.857	0.928	0.791	0.865	0.092	0.038	12.56%
	M3	0.969	0.907	0.868	0.858	0.888	0.938	0.813	0.879	0.093	0.037	65.55%
	M4	0.972	0.917	0.881	0.870	0.887	0.942	0.834	0.887	0.092	0.036	10.83%
	M5	0.978	0.937	0.903	0.889	0.886	0.957	0.848	0.899	0.095	0.025	12.86%
GDD [98]	M1	0.930	0.915	0.900	0.887	0.845	0.900	0.852	0.905	0.061	0.068	
	M2	0.933	0.920	0.909	0.891	0.850	0.906	0.861	0.910	0.061	0.065	11.81%
	M3	0.943	0.924	0.919	0.904	0.878	0.914	0.874	0.921	0.055	0.058	74.02%
	M4	0.944	0.927	0.917	0.902	0.893	0.923	0.898	0.924	0.052	0.055	75.42%
	M5	0.960	0.933	0.927	0.916	0.897	0.934	0.904	0.935	0.049	0.049	77.89%
ORSI-4199 [135]	M1	0.960	0.820	0.792	0.808	0.831	0.878	0.727	0.780	0.122	0.045	
	M2	0.961	0.832	0.812	0.808	0.836	0.890	0.730	0.855	0.120	0.043	11.42%
	M3	0.965	0.855	0.827	0.846	0.872	0.912	0.746	0.884	0.112	0.038	14.82%
	M4	0.967	0.865	0.835	0.830	0.852	0.921	0.752	0.874	0.108	0.036	6.37%
	M5	0.969	0.883	0.853	0.840	0.864	0.935	0.767	0.899	0.095	0.032	79.48%

is very important to distinguish the fore/background, which drives the network to pay more attention on low-level features. **II)** For the distribution of gate values at all levels in the parallel branch, the greater contribution of G1 and G2 in Fig. 8(d), (h) compared to the other tasks further illustrates the importance of details information in camouflaged and polyp segmentation tasks. **III)** As shown in Fig. 8(e), G4 and G5 have high values in both FPN branch and parallel branch, indicating that the accurate localization of focused regions is extremely crucial for defocus blur detection and motivate the network to consistently maintain a high pass-through pattern for high-level features. **IV)** Compared to other gate values in the FPN branch, G4 is the largest one

Table 14 Ablation experiments for RGB-D salient object detection. M1: FPN Baseline. M2: + Residual Parallel Branch. M3: + Cross-modal Gate Units. M4: + Encoder-Decoder Gate Units. M5: + Fold-ASPP.

Dataset	Method	$PA \uparrow$	$F_{\beta}^{max} \uparrow$	$F_{\beta}^{mean} \uparrow$	$F_{\beta}^{\omega} \uparrow$	$S_m \uparrow$	$E_m \uparrow$	$IOU \uparrow$	$Dice \uparrow$	$BER \downarrow$	$AM \downarrow$	$\Delta \text{ gains}$
STERE [100]	M1	0.944	0.882	0.853	0.802	0.860	0.874	0.817	0.832	0.057	0.048	
	M2	0.949	0.888	0.871	0.825	0.870	0.890	0.825	0.845	0.045	0.044	2.31%
	M3	0.958	0.905	0.885	0.847	0.892	0.914	0.838	0.867	0.050	0.041	15.53%
	M4	0.960	0.925	0.897	0.869	0.910	0.934	0.850	0.887	0.048	0.036	78.80%
	M5	0.970	0.929	0.907	0.889	0.922	0.957	0.889	0.922	0.043	0.033	111.42%
SIP [32]	M1	0.952	0.877	0.850	0.810	0.859	0.860	0.774	0.816	0.110	0.078	
	M2	0.955	0.885	0.861	0.817	0.862	0.874	0.795	0.830	0.114	0.078	34.41%
	M3	0.960	0.892	0.874	0.847	0.871	0.884	0.822	0.865	0.116	0.078	67.95%
	M4	0.960	0.915	0.890	0.862	0.894	0.922	0.827	0.879	0.070	0.044	12.18%
	M5	0.963	0.927	0.902	0.877	0.903	0.939	0.840	0.889	0.073	0.033	115.39%
NJUD [59]	M1	0.953	0.874	0.830	0.825	0.867	0.870	0.802	0.848	0.072	0.059	
	M2	0.957	0.886	0.845	0.840	0.876	0.886	0.820	0.866	0.067	0.055	2.73%
	M3	0.964	0.905	0.874	0.874	0.891	0.914	0.850	0.887	0.065	0.046	17.82%
	M4	0.964	0.924	0.902	0.882	0.912	0.934	0.879	0.914	0.061	0.041	112.96%
	M5	0.975	0.943	0.928	0.913	0.931	0.956	0.888	0.924	0.041	0.028	116.80%
NLPR [105]	M1	0.952	0.882	0.840								

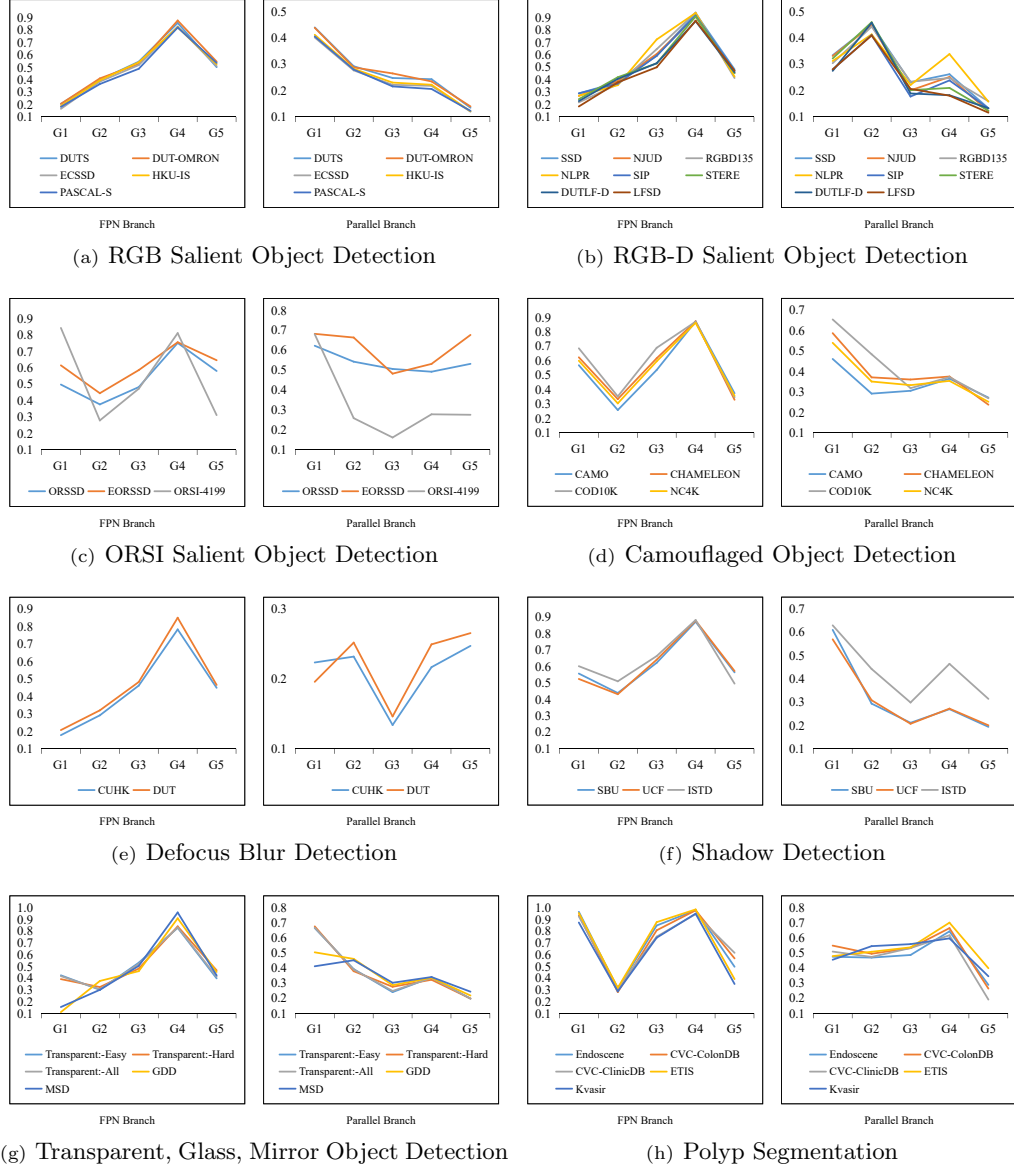


Fig. 8 Distributions of gate weights separately presented in the FPN and parallel branch on 35 datasets of 10 tasks.

rows). The corners of the poster, the limbs and even tentacles of the mantis are retained well. Besides, we show the visual results of the gate units in the two-stream network for RGB-D SOD, as shown in Fig. 10. Intuitively, the depth branch has more significant and pure position and edge information about the foreground (cloth) than the RGB branch on E4, E2 and E1, thus distributes larger gate weights correspondingly in cross-modal fusion.

• **Folded Atrous Convolution.** Based on the gated dual branch network, we design a series of experimental options to verify the effectiveness of the folded atrous convolution. Tab. 15 illustrates the results in detail. We adopt the atrous convolution with dilation rates of [2, 4, 6] and the same dilation rates are also applied to the folded atrous convolution. It can be observed that the folded atrous convolution consistently yields significant performance improvement at

Table 15 Evaluation of the folded atrous convolution. (x) stands for different sampling rates of atrous convolution. D-ASPP is DenseASPP [170].

Metric	Atrous r=2	Atrous r=4	Atrous r=6	Fold r=2	Fold r=4	Fold r=6	ASPP	Fold- ASPP	D-ASPP	Fold- D-ASPP
<i>DUITS [148]</i>										
$PA \uparrow$	0.970	0.970	0.971	0.971	0.971	0.971	0.972	0.972	0.971	0.971
$F_{\beta}^{max} \uparrow$	0.894	0.895	0.898	0.898	0.902	0.906	0.903	0.911	0.902	0.909
$F_{\beta}^{mean} \uparrow$	0.843	0.845	0.848	0.847	0.851	0.853	0.852	0.857	0.854	0.861
$F_{\beta}^2 \uparrow$	0.837	0.841	0.843	0.841	0.845	0.852	0.850	0.864	0.844	0.858
$S_m \uparrow$	0.891	0.894	0.896	0.896	0.899	0.901	0.901	0.906	0.898	0.902
$E_m \uparrow$	0.914	0.916	0.918	0.918	0.921	0.924	0.924	0.931	0.923	0.934
$IOU \uparrow$	0.805	0.806	0.811	0.811	0.815	0.820	0.816	0.828	0.815	0.821
$Dice \uparrow$	0.856	0.859	0.861	0.861	0.863	0.867	0.864	0.864	0.864	0.872
$BER \downarrow$	0.073	0.069	0.064	0.067	0.062	0.056	0.057	0.052	0.060	0.057
$M \downarrow$	0.035	0.034	0.034	0.034	0.034	0.033	0.033	0.030	0.031	0.031
Δ gains	10.76%	11.94%	11.48%	12.48%	13.91%	13.62%	16.03%	12.78%	14.73%	
<i>Kewei [53]</i>										
$PA \uparrow$	0.968	0.968	0.970	0.971	0.973	0.975	0.974	0.976	0.974	0.976
$F_{\beta}^{max} \uparrow$	0.929	0.938	0.932	0.933	0.935	0.935	0.937	0.935	0.935	0.941
$F_{\beta}^{mean} \uparrow$	0.899	0.902	0.904	0.905	0.903	0.912	0.909	0.916	0.913	0.922
$F_{\beta}^2 \uparrow$	0.888	0.889	0.892	0.893	0.896	0.899	0.897	0.903	0.897	0.902
$S_m \uparrow$	0.902	0.905	0.912	0.907	0.912	0.917	0.915	0.921	0.917	0.925
$E_m \uparrow$	0.941	0.943	0.945	0.945	0.949	0.953	0.952	0.958	0.949	0.953
$IOU \uparrow$	0.827	0.831	0.835	0.842	0.844	0.847	0.853	0.864	0.850	0.860
$Dice \uparrow$	0.892	0.898	0.900	0.898	0.901	0.908	0.908	0.912	0.905	0.910
$BER \downarrow$	0.076	0.074	0.070	0.071	0.065	0.064	0.064	0.054	0.065	0.056
$M \downarrow$	0.031	0.030	0.029	0.029	0.027	0.026	0.027	0.024	0.027	0.025
Δ gains	10.81%	11.93%	11.84%	13.13%	14.31%	13.96%	16.86%	13.80%	16.30%	
<i>COD-DRC [30]</i>										
$PA \uparrow$	0.972	0.972	0.972	0.972	0.974	0.974	0.973	0.974	0.972	0.973
$F_{\beta}^{max} \uparrow$	0.808	0.811	0.813	0.814	0.817	0.819	0.819	0.823	0.810	0.810
$F_{\beta}^{mean} \uparrow$	0.730	0.734	0.738	0.737	0.741	0.747	0.746	0.752	0.740	0.745
$F_{\beta}^2 \uparrow$	0.717	0.720	0.722	0.724	0.729	0.734	0.730	0.742	0.717	0.726
$S_m \uparrow$	0.828	0.833	0.834	0.833	0.837	0.840	0.836	0.846	0.833	0.839
$E_m \uparrow$	0.878	0.882	0.886	0.884	0.890	0.893	0.893	0.901	0.890	0.895
$IOU \uparrow$	0.663	0.667	0.671	0.670	0.677	0.680	0.679	0.689	0.665	0.671
$Dice \uparrow$	0.753	0.755	0.756	0.758	0.761	0.764	0.761	0.768	0.747	0.751
$BER \downarrow$	0.135	0.138	0.127	0.130	0.123	0.119	0.121	0.114	0.133	0.126
$M \downarrow$	0.033	0.032	0.032	0.031	0.030	0.030	0.031	0.028	0.032	0.030
Δ gains	11.47%	12.74%	13.39%	14.40%	15.31%	14.64%	17.50%	15.08%	18.03%	
<i>DUT [199]</i>										
$PA \uparrow$	0.931	0.932	0.934	0.934	0.935	0.935	0.937	0.939	0.937	0.939
$F_{\beta}^{max} \uparrow$	0.892	0.895	0.898	0.896	0.899	0.901	0.900	0.905	0.901	0.910
$F_{\beta}^{mean} \uparrow$	0.863	0.867	0.871	0.872	0.875	0.881	0.879	0.886	0.878	0.887
$F_{\beta}^2 \uparrow$	0.840	0.844	0.847	0.847	0.851	0.854	0.852	0.861	0.854	0.864
$S_m \uparrow$	0.837	0.840	0.845	0.844	0.850	0.854	0.852	0.862	0.853	0.866
$E_m \uparrow$	0.872	0.877	0.883	0.882	0.887	0.892	0.892	0.908	0.896	0.905
$IOU \uparrow$	0.779	0.784	0.790	0.788	0.796	0.804	0.800	0.816	0.805	0.822
$Dice \uparrow$	0.855	0.859	0.863	0.865	0.870	0.874	0.872	0.882	0.874	0.885
$BER \downarrow$	0.107	0.099	0.092	0.089	0.084	0.080	0.084	0.072	0.080	0.068
$M \downarrow$	0.079	0.076	0.074	0.071	0.070	0.069	0.070	0.064	0.070	0.064
Δ gains	10.78%	12.20%	11.85%	13.07%	13.59%	13.22%	15.39%	12.29%	13.68%	
<i>SDU [188]</i>										
$PA \uparrow$	0.972	0.974	0.975	0.975	0.976	0.977	0.978	0.976	0.976	0.976
$F_{\beta}^{max} \uparrow$	0.917	0.921	0.924	0.923	0.927	0.931	0.930	0.937	0.927	0.934
$F_{\beta}^{mean} \uparrow$	0.881	0.886	0.891	0.890	0.893	0.897	0.896	0.901	0.894	0.900
$F_{\beta}^2 \uparrow$	0.873	0.876	0.877	0.876	0.880	0.883	0.882	0.889	0.877	0.883
$S_m \uparrow$	0.870	0.873	0.875	0.876	0.878	0.881	0.880	0.886	0.875	0.881
$E_m \uparrow$	0.944	0.946	0.949	0.948	0.951	0.952	0.951	0.957	0.950	0.954
$IOU \uparrow$	0.825	0.831	0.836	0.833	0.839	0.843	0.842	0.848	0.836	0.840
$Dice \uparrow$	0.882	0.885	0.888	0.886	0.891	0.893	0.894	0.898	0.885	0.892
$BER \downarrow$	0.072	0.071	0.065	0.067	0.065	0.063	0.063	0.059	0.067	0.064
$M \downarrow$	0.031	0.030	0.029	0.029	0.027	0.027	0.028	0.025	0.028	0.026
Δ gains	10.78%	12.20%	11.85%	13.07%	13.59%	13.22%	15.39%	12.29%	13.68%	
<i>OSR44109 [135]</i>										
$PA \uparrow$	0.966	0.967	0.967	0.968	0.967	0.968	0.967	0.969	0.968	0.970
$F_{\beta}^{max} \uparrow$	0.864	0.867	0.869	0.870	0.873	0.877	0.876	0.883	0.876	0.888
$F_{\beta}^{mean} \uparrow$	0.834	0.837	0.840	0.830	0.845	0.847	0.846	0.853	0.845	0.853
$F_{\beta}^2 \uparrow$	0.830	0.831	0.833	0.833	0.836	0.838	0.836	0.840	0.838	0.848
$S_m \uparrow$	0.850	0.854	0.856	0.855	0.858	0.860	0.860	0.864	0.862	0.869
$E_m \uparrow$	0.919	0.923	0.926	0.925	0.929	0.930	0.929	0.935	0.932	0.938
$IOU \uparrow$	0.754	0.755	0.758	0.760	0.762	0.763	0.763	0.767	0.766	0.778
$Dice \uparrow$	0.816	0.820	0.824	0.823	0.829	0.832	0.830	0.839	0.835	0.848
$BER \downarrow$	0.111	0.105	0.103	0.103	0.101	0.100	0.101	0.095	0.098	0.089
$M \downarrow$	0.037	0.037	0.036	0.036	0.034	0.035	0.035	0.032	0.035	0.031
Δ gains	10.79%	11.47%	11.47%	12.50%	12.78%	12.32%	14.06%	12.77%	15.59%	

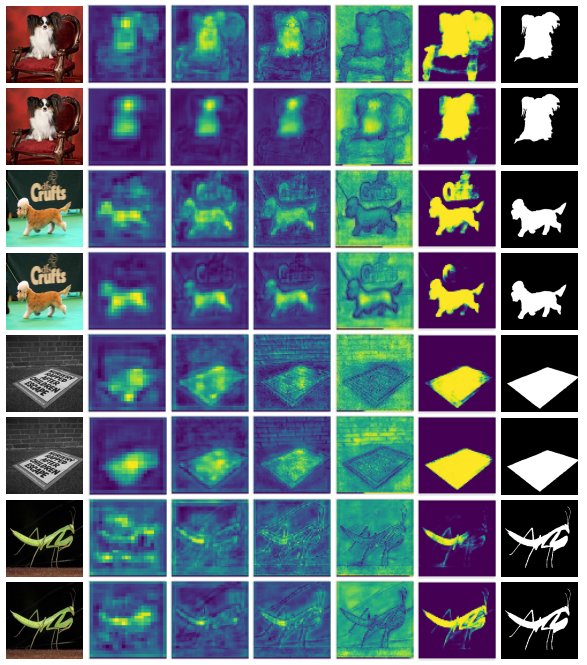


Fig. 9 Visual comparison of feature maps for showing the effect of the multi-level gate units. D5 ~ D1 represent the feature maps of each decoder block from high level to low level. Odd rows and even rows are the results of the FPN baseline without or with multi-level gate units, respectively.

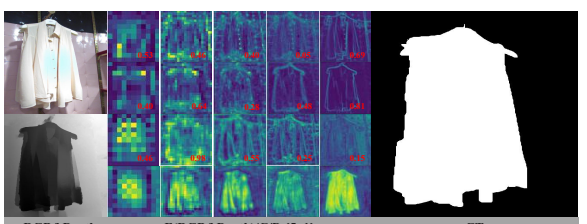


Fig. 11 shows visual results of the above ablation studies on some examples. It can be seen that the gated FPN model accurately determines where is the foreground object. With the help of Fold-ASPP, the overall integrity of the object is further captured. It should also be noted that the gated

each dilation rate than the corresponding atrous convolution in terms of all ten metrics. And the single-layer Fold(6) already performs better than the ASPP and DenseASPP of aggregating three atrous convolution layers. The Fold-ASPP and Fold-DenseASPP naturally outperforms the ASPP and DenseASPP, respectively. Our fold operation can naturally increase the receptive field. For a fair comparison, we can also see that compared with Atrous(4) with the same receptive field, Fold(2) still has an advantage under all metrics.

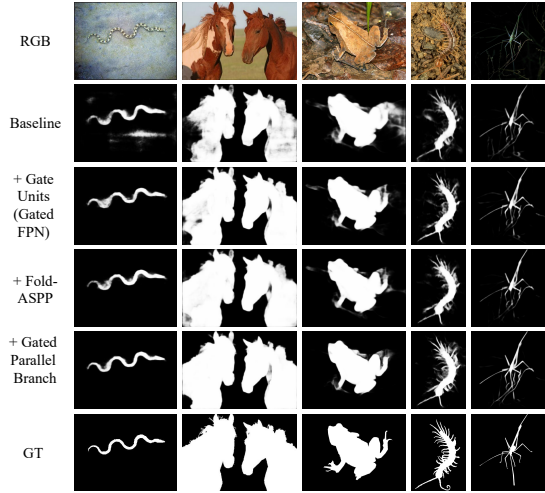


Fig. 11 Illustration of the benefit of each component.

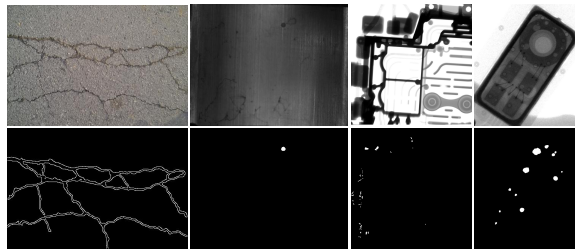


Fig. 12 Some examples of surface defect detection (e.g., crack, magnetic tiles, car parts, electronic components).

parallel branch can improve perceptual results greatly by highlighting the fore/back-ground difference and preserving the intra-class consistency, thereby yielding the sharpened boundary.

5 Discussion

In this section, we further discuss the multi-level gated mechanism and give some potential applications:

- Our gate unit can suppress both each channel and spatial pixel of feature maps. In this way, the network actually learns adaptive thresholding. The area of which feature values are below this threshold has a lower response in the prediction, while the feature values above this threshold correspond to the task-specific activation area. It helps the decoder to gradually filter out the region with strong feature response. This kind of region can usually attract our attention. If we remove the gate units, the network will not have such strong constraints. Therefore, the gated mechanism can

also be regarded as an implicit supervision.

- The proposed gated mechanism has its limitations. It is unsuitable for semantic segmentation task. Because this task needs to treat all pixels of the whole image equally importantly and all categories have the same importance, the information suppression design is out of place. This also means that the GateNet has wider applicability to binary segmentation problems.

- In this paper, we have given detailed experimental analyses in ten popular binary segmentation tasks. Besides, GateNet has potential application in the field of industry with complex scenes as shown in Fig 12. We hope that this study can provide deep insights into the underlying design for more binary segmentation tasks and spark novel ideas.

6 Conclusions

As far as we know, this is the first work to comprehensively review recent progress in binary segmentation, which summarizes more than 140 fully supervised models according to task settings, technique contributions, and learning strategies. To unify all the sub-branches and establish a fair model benchmark to promote the prosperous development of the binary segmentation field, we propose a novel yet general gated network architecture. We first adopt multi-level gate units to balance the contribution of each encoder block and suppress the activation of the features of non-task-aware regions, which can provide useful context information for the decoder while minimizing interference. We quantitatively reveal the role played by features at all levels of the encoder for different segmentation tasks, which provides a new perspective on the interpretability of deep learning. Next, we use the Fold-ASPP to gather multi-scale semantic information for the decoder. By the folded operation, the atrous convolution achieves a local-in-local effect, which not only expands the receptive field but also retains the correlation among local sampling points. Finally, to further supplement the details, we combine all encoder features in parallel and construct a residual structure. Experimental results on 33 benchmark datasets towards 10 binary segmentation tasks demonstrate that the proposed model outperforms 42 state-of-the-art methods under 10 evaluation metrics.

References

- [1] Radhakrishna Achanta, Sheila Hemami, Francisco Estrada, and Sabine Süsstrunk. Frequency-tuned salient region detection. In *CVPR*, pages 1597–1604, 2009.
- [2] Edward Adelson, Charles Anderson, James Bergen, Peter Burt, and Joan Ogden. Pyramid methods in image processing. *RCA Eng.*, 29, 11 1983.
- [3] Md Amirul Islam, Mrigank Rochan, Neil DB Bruce, and Yang Wang. Gated feedback refinement network for dense image labeling. In *CVPR*, pages 3751–3759, 2017.
- [4] Pablo Arbelaez, Michael Maire, Charless Fowlkes, and Jitendra Malik. Contour detection and hierarchical image segmentation. *IEEE TPAMI*, 33:898–916, 2010.
- [5] Jorge Bernal, F Javier Sánchez, Gloria Fernández-Esparrach, Debora Gil, Cristina Rodríguez, and Fernando Vilarino. Wm-dova maps for accurate polyp highlighting in colonoscopy: Validation vs. saliency maps from physicians. *CMIG*, 43:99–111, 2015.
- [6] Chenglizhao Chen, Jipeng Wei, Chong Peng, Weizhong Zhang, and Hong Qin. Improved saliency detection in rgb-d images using two-phase depth estimation and selective deep fusion. *IEEE TIP*, 29:4296–4307, 2020.
- [7] Guanying Chen, Kai Han, and Kwan-Yee K Wong. Tom-net: Learning transparent object matting from a single image. In *CVPR*, pages 9233–9241, 2018.
- [8] Hao Chen, Yongjian Deng, Youfu Li, Tzu-Yi Hung, and Guosheng Lin. Rgb-d salient object detection via disentangled cross-modal fusion. *IEEE TIP*, 29:8407–8416, 2020.
- [9] Hao Chen and Youfu Li. Progressively complementarity-aware fusion network for rgb-d salient object detection. In *CVPR*, pages 3051–3060, 2018.
- [10] Hao Chen and Youfu Li. Three-stream attention-aware network for rgb-d salient object detection. *IEEE TIP*, 28:2825–2835, 2019.
- [11] Hao Chen, Youfu Li, and Dan Su. Multi-modal fusion network with multi-scale multi-path and cross-modal interactions for rgb-d salient object detection. *Pattern Recognition*, 86:376–385, 2019.
- [12] Liang-Chieh Chen, George Papandreou, Iasonas Kokkinos, Kevin Murphy, and Alan L Yuille. Deeplab: Semantic image segmentation with deep convolutional nets, atrous convolution, and fully connected crfs. *IEEE TPAMI*, 40:834–848, 2017.
- [13] Qian Chen, Ze Liu, Yi Zhang, Keren Fu, Qijun Zhao, and Hongwei Du. Rgb-d salient object detection via 3d convolutional neural networks. In *AAAI*, pages 1063–1071, 2021.
- [14] Shuhan Chen and Yun Fu. Progressively guided alternate refinement network for rgb-d salient object detection. In *ECCV*, pages 520–538, 2020.
- [15] Shuhan Chen, Xiuli Tan, Ben Wang, and Xuelong Hu. Reverse attention for salient object detection. In *ECCV*, pages 234–250, 2018.
- [16] Zuyao Chen, Runmin Cong, Qianqian Xu, and Qingming Huang. Dpanet: Depth potentiality-aware gated attention network for rgb-d salient object detection. *IEEE TIP*, 30:7012–7024, 2020.
- [17] Zuyao Chen, Qianqian Xu, Runmin Cong, and Qingming Huang. Global context-aware progressive aggregation network for salient object detection. In *AAAI*, pages 10599–10606, 2020.
- [18] Mengjun Cheng, Zishang Kong, Guoli Song, Yonghong Tian, Yongsheng Liang, and Jie Chen. Learnable oriented-derivative network for polyp segmentation. In *MICCAI*, pages 720–730, 2021.

- [19] Ming-Ming Cheng, Niloy J Mitra, Xiaolei Huang, Philip HS Torr, and Shi-Min Hu. Global contrast based salient region detection. *IEEE TPAMI*, 37:569–582, 2014.
- [20] Yupeng Cheng, Huazhu Fu, Xingxing Wei, Jiangjian Xiao, and Xiaochun Cao. Depth enhanced saliency detection method. In *ICIMCS*, page 23, 2014.
- [21] François Chollet. Xception: Deep learning with depthwise separable convolutions. In *CVPR*, pages 1251–1258, 2017.
- [22] Runmin Cong, Yumo Zhang, Leyuan Fang, Jun Li, Yao Zhao, and Sam Kwong. RRNet: Relational reasoning network with parallel multi-scale attention for salient object detection in optical remote sensing images. *IEEE TGRS*, 60:1558–1644, 2022.
- [23] Xiaodong Cun and Chi-Man Pun. Defocus blur detection via depth distillation. In *ECCV*, pages 747–763, 2020.
- [24] Zijun Deng, Xiaowei Hu, Lei Zhu, Xuemiao Xu, Jing Qin, Guoqiang Han, and Pheng-Ann Heng. R3net: Recurrent residual refinement network for saliency detection. In *IJCAI*, pages 684–690, 2018.
- [25] Bin Ding, Chengjiang Long, Ling Zhang, and Chunxia Xiao. Argan: Attentive recurrent generative adversarial network for shadow detection and removal. In *ICCV*, pages 10213–10222, 2019.
- [26] Alexey Dosovitskiy, Lucas Beyer, Alexander Kolesnikov, Dirk Weissenborn, Xiaohua Zhai, Thomas Unterthiner, Mostafa Dehghani, Matthias Minderer, Georg Heigold, Sylvain Gelly, et al. An image is worth 16x16 words: Transformers for image recognition at scale. *arXiv preprint arXiv:2010.11929*, 2020.
- [27] Mark Everingham, Luc Van Gool, Christopher KI Williams, John Winn, and Andrew Zisserman. The pascal visual object classes (voc) challenge. *IJCV*, 88(2):303–338, 2010.
- [28] Deng-Ping Fan, Ming-Ming Cheng, Yun Liu, Tao Li, and Ali Borji. Structure-measure: A new way to evaluate foreground maps. In *ICCV*, pages 4548–4557, 2017.
- [29] Deng-Ping Fan, Cheng Gong, Yang Cao, Bo Ren, Ming-Ming Cheng, and Ali Borji. Enhanced-alignment measure for binary foreground map evaluation. *arXiv preprint arXiv:1805.10421*, 2018.
- [30] Deng-Ping Fan, Ge-Peng Ji, Guolei Sun, Ming-Ming Cheng, Jianbing Shen, and Ling Shao. Camouflaged object detection. In *CVPR*, pages 2777–2787, 2020.
- [31] Deng-Ping Fan, Ge-Peng Ji, Tao Zhou, Geng Chen, Huazhu Fu, Jianbing Shen, and Ling Shao. Planet: Parallel reverse attention network for polyp segmentation. In *MICCAI*, pages 263–273, 2020.
- [32] Deng-Ping Fan, Zheng Lin, Zhao Zhang, Menglong Zhu, and Ming-Ming Cheng. Rethinking rgb-d salient object detection: Models, data sets, and large-scale benchmarks. *IEEE TNNLS*, 32:2075–2089, 2020.
- [33] Deng-Ping Fan, Yingjie Zhai, Ali Borji, Jufeng Yang, and Ling Shao. Bbs-net: Rgb-d salient object detection with a bifurcated backbone strategy network. In *ECCV*, pages 275–292, 2020.
- [34] Hao Fang, Saurabh Gupta, Forrest Iandola, Rupesh K Srivastava, Li Deng, Piotr Dollár, Jianfeng Gao, Xiaodong He, Margaret Mitchell, John C Platt, et al. From captions to visual concepts and back. In *CVPR*, pages 1473–1482, 2015.
- [35] Xianyong Fang, Xiaohao He, Linbo Wang, and Jianbing Shen. Robust shadow detection by exploring effective shadow contexts. In *ACM MM*, pages 2927–2935, 2021.
- [36] Yuqi Fang, Cheng Chen, Yixuan Yuan, and Kai-yu Tong. Selective feature aggregation network with area-boundary constraints for polyp segmentation. In *MICCAI*, pages 302–310, 2019.

- [37] Mengyang Feng, Huchuan Lu, and Errui Ding. Attentive feedback network for boundary-aware salient object detection. In *CVPR*, pages 1623–1632, 2019.
- [38] Keren Fu, Deng-Ping Fan, Ge-Peng Ji, and Qijun Zhao. Jl-dcf: Joint learning and densely-cooperative fusion framework for rgb-d salient object detection. In *CVPR*, pages 3052–3062, 2020.
- [39] Keren Fu, Deng-Ping Fan, Ge-Peng Ji, and Qijun Zhao. Jl-dcf: Joint learning and densely-cooperative fusion framework for rgb-d salient object detection. In *CVPR*, pages 3052–3062, 2020.
- [40] Shang-Hua Gao, Ming-Ming Cheng, Kai Zhao, Xin-Yu Zhang, Ming-Hsuan Yang, and Philip Torr. Res2net: A new multi-scale backbone architecture. *IEEE TPAMI*, 43:652–662, 2019.
- [41] Shang-Hua Gao, Yong-Qiang Tan, Ming-Ming Cheng, Chengze Lu, Yumpeng Chen, and Shuicheng Yan. Highly efficient salient object detection with 100k parameters. In *ECCV*, pages 702–721, 2020.
- [42] Yu-Chao Gu, Shang-Hua Gao, Xu-Sheng Cao, Peng Du, Shao-Ping Lu, and Ming-Ming Cheng. inas: Integral nas for device-aware salient object detection. In *ICCV*, pages 4934–4944, 2021.
- [43] Hao He, Xiangtai Li, Guangliang Cheng, Jianping Shi, Yunhai Tong, Gaofeng Meng, Véronique Prinet, and LuBin Weng. Enhanced boundary learning for glass-like object segmentation. In *ICCV*, pages 15859–15868, 2021.
- [44] Kaiming He, Xiangyu Zhang, Shaoqing Ren, and Jian Sun. Deep residual learning for image recognition. In *CVPR*, pages 770–778, 2016.
- [45] Qibin Hou, Ming-Ming Cheng, Xiaowei Hu, Ali Borji, Zhiwen Tu, and Philip HS Torr. Deeply supervised salient object detection with short connections. In *CVPR*, pages 3203–3212, 2017.
- [46] Andrew G Howard, Menglong Zhu, Bo Chen, Dmitry Kalenichenko, Weijun Wang, Tobias Weyand, Marco Andreetto, and Hartwig Adam. Mobilenets: Efficient convolutional neural networks for mobile vision applications. *arXiv preprint arXiv:1704.04861*, 2017.
- [47] Jie Hu, Li Shen, and Gang Sun. Squeeze-and-excitation networks. In *CVPR*, pages 7132–7141, 2018.
- [48] Xiaowei Hu, Chi-Wing Fu, Lei Zhu, Jing Qin, and Pheng-Ann Heng. Direction-aware spatial context features for shadow detection and removal. *IEEE TPAMI*, 42:2795–2808, 2019.
- [49] Xiaowei Hu, Tianyu Wang, Chi-Wing Fu, Yitong Jiang, Qiong Wang, and Pheng-Ann Heng. Revisiting shadow detection: A new benchmark dataset for complex world. *IEEE TIP*, 30:1925–1934, 2021.
- [50] Xiaowei Hu, Lei Zhu, Chi-Wing Fu, Jing Qin, and Pheng-Ann Heng. Direction-aware spatial context features for shadow detection. In *CVPR*, pages 7454–7462, 2018.
- [51] Gao Huang, Zhuang Liu, Laurens Van Der Maaten, and Kilian Q Weinberger. Densely connected convolutional networks. In *CVPR*, pages 4700–4708, 2017.
- [52] Debesh Jha, Pia H Smedsrud, Dag Johansen, Thomas de Lange, Håvard D Johansen, Pål Halvorsen, and Michael A Riegler. A comprehensive study on colorectal polyp segmentation with resunet++, conditional random field and test-time augmentation. *IEEE JBHI*, 25:2029–2040, 2021.
- [53] Debesh Jha, Pia H Smedsrud, Michael A Riegler, Pål Halvorsen, Thomas de Lange, Dag Johansen, and Håvard D Johansen. Kvasir-seg: A segmented polyp dataset. In *MMM*, pages 451–462, 2020.
- [54] Ge-Peng Ji, Lei Zhu, Mingchen Zhuge, and Keren Fu. Fast camouflaged object detection via edge-based reversible re-calibration

network. *Pattern Recognition*, 123:108414, 2022.

[55] Wei Ji, Jingjing Li, Shuang Yu, Miao Zhang, Yongri Piao, Shunyu Yao, Qi Bi, Kai Ma, Yefeng Zheng, Huchuan Lu, et al. Calibrated rgb-d salient object detection. In *CVPR*, pages 9471–9481, 2021.

[56] Wei Ji, Jingjing Li, Miao Zhang, Yongri Piao, and Huchuan Lu. Accurate rgb-d salient object detection via collaborative learning. In *ECCV*, pages 52–69, 2020.

[57] Bo Jiang, Zitai Zhou, Xiao Wang, Jin Tang, and Bin Luo. cmsalgan: Rgb-d salient object detection with cross-view generative adversarial networks. *IEEE TMM*, 23:1343–1353, 2020.

[58] Wen-Da Jin, Jun Xu, Qi Han, Yi Zhang, and Ming-Ming Cheng. Cdnet: Complementary depth network for rgb-d salient object detection. *IEEE TIP*, 30:3376–3390, 2021.

[59] Ran Ju, Ling Ge, Wenjing Geng, Tongwei Ren, and Gangshan Wu. Depth saliency based on anisotropic center-surround difference. In *ICIP*, pages 1115–1119, 2014.

[60] Imran N Junejo and Hassan Foroosh. Estimating geo-temporal location of stationary cameras using shadow trajectories. In *ECCV*, pages 318–331, 2008.

[61] Rezaul Karim, Md Amirul Islam, and Neil D. B. Bruce. Recurrent iterative gating networks for semantic segmentation. In *WACV*, pages 1070–1079, 2019.

[62] Jinhee Kim and Wonjun Kim. Attentive feedback feature pyramid network for shadow detection. *IEEE SPL*, 27:1964–1968, 2020.

[63] Taehun Kim, Hyemin Lee, and Daijin Kim. Uacanet: Uncertainty augmented context attention for polyp segmentation. In *ACM MM*, pages 2167–2175, 2021.

[64] Diederick P Kingma and Jimmy Ba. Adam: A method for stochastic optimization. In *ICLR*, 2015.

[65] Hieu Le, Tomas F Yago Vicente, Vu Nguyen, Minh Hoai, and Dimitris Samaras. A+ d net: Training a shadow detector with adversarial shadow attenuation. In *ECCV*, pages 662–678, 2018.

[66] Trung-Nghia Le, Tam V Nguyen, Zhongliang Nie, Minh-Triet Tran, and Akihiro Sugimoto. Anabrand network for camouflaged object segmentation. *CVIU*, 184:45–56, 2019.

[67] Chen-Yu Lee, Saining Xie, Patrick Gallagher, Zhengyou Zhang, and Zhuowen Tu. Deeply-supervised nets. In *Artificial intelligence and statistics*, pages 562–570. PMLR, 2015.

[68] Aixuan Li, Jing Zhang, Yunqiu Lv, Bowen Liu, Tong Zhang, and Yuchao Dai. Uncertainty-aware joint salient object and camouflaged object detection. In *CVPR*, pages 10071–10081, 2021.

[69] Chongyi Li, Runmin Cong, Chunle Guo, Hua Li, Chunjie Zhang, Feng Zheng, and Yao Zhao. A parallel down-up fusion network for salient object detection in optical remote sensing images. *Neurocomputing*, 415:411–420, 2020.

[70] Chongyi Li, Runmin Cong, Junhui Hou, Sanyi Zhang, Yue Qian, and Sam Kwong. Nested network with two-stream pyramid for salient object detection in optical remote sensing images. *IEEE TGRS*, 57:9156–9166, 2019.

[71] Chongyi Li, Runmin Cong, Yongri Piao, Qianqian Xu, and Chen Change Loy. Rgb-d salient object detection with cross-modality modulation and selection. In *ECCV*, pages 225–241, 2020.

[72] Gongyang Li, Zhi Liu, Minyu Chen, Zhen Bai, Weisi Lin, and Haibin Ling. Hierarchical alternate interaction network for rgb-d salient object detection. *IEEE TIP*, 30:3528–3542, 2021.

[73] Gongyang Li, Zhi Liu, and Haibin Ling. Icnet: Information conversion network for rgb-d based salient object detection. *IEEE TIP*, 29:4873–4884, 2020.

[74] Gongyang Li, Zhi Liu, Linwei Ye, Yang Wang, and Haibin Ling. Cross-modal weighting network for rgb-d salient object detection. In *ECCV*, pages 665–681, 2020.

[75] Guanbin Li and Yizhou Yu. Visual saliency based on multiscale deep features. In *CVPR*, pages 5455–5463, 2015.

[76] Nianyi Li, Jinwei Ye, Yu Ji, Haibin Ling, and Jingyi Yu. Saliency detection on light field. In *CVPR*, pages 2806–2813, 2014.

[77] Yin Li, Xiaodi Hou, Christof Koch, James M Rehg, and Alan L Yuille. The secrets of salient object segmentation. In *CVPR*, pages 280–287, 2014.

[78] Guibiao Liao, Wei Gao, Qiuping Jiang, Ronggang Wang, and Ge Li. Mmnet: Multi-stage and multi-scale fusion network for rgb-d salient object detection. In *ACM MM*, pages 2436–2444, 2020.

[79] Jingwei Liao, Yanli Liu, Guanyu Xing, Housheng Wei, Jueyu Chen, and Songhua Xu. Shadow detection via predicting the confidence maps of shadow detection methods. In *ACM MM*, pages 704–712, 2021.

[80] Jiaying Lin, Zebang He, and Rynson WH Lau. Rich context aggregation with reflection prior for glass surface detection. In *CVPR*, pages 13415–13424, 2021.

[81] Jiaying Lin, Guodong Wang, and Rynson WH Lau. Progressive mirror detection. In *CVPR*, pages 3697–3705, 2020.

[82] Tsung-Yi Lin, Piotr Dollár, Ross Girshick, Kaiming He, Bharath Hariharan, and Serge Belongie. Feature pyramid networks for object detection. In *CVPR*, pages 2117–2125, 2017.

[83] Jiang-Jiang Liu, Qibin Hou, Ming-Ming Cheng, Jiashi Feng, and Jianmin Jiang. A simple pooling-based design for real-time salient object detection. In *CVPR*, pages 3917–3926, 2019.

[84] Nian Liu and Junwei Han. Dhsnet: Deep hierarchical saliency network for salient object detection. In *CVPR*, pages 678–686, 2016.

[85] Nian Liu, Junwei Han, and Ming-Hsuan Yang. Picanet: Learning pixel-wise contextual attention for saliency detection. In *CVPR*, pages 3089–3098, 2018.

[86] Nian Liu, Ni Zhang, and Junwei Han. Learning selective self-mutual attention for rgb-d saliency detection. In *CVPR*, pages 13756–13765, 2020.

[87] Nian Liu, Ni Zhang, Kaiyuan Wan, Ling Shao, and Junwei Han. Visual saliency transformer. In *ICCV*, pages 4722–4732, 2021.

[88] Tie Liu, Zejian Yuan, Jian Sun, Jingdong Wang, Nanning Zheng, Xiaou Tang, and Heung-Yeung Shum. Learning to detect a salient object. *IEEE TPAMI*, 33:353–367, 2010.

[89] Xuan Liu, Yumo Zhang, Runmin Cong, Chen Zhang, Ning Yang, Chunjie Zhang, and Yao Zhao. Ggrnet: Global graph reasoning network for salient object detection in optical remote sensing images. In *PRCV*, pages 584–596, 2021.

[90] Yi Liu, Qiang Zhang, Dingwen Zhang, and Jungong Han. Employing deep part-object relationships for salient object detection. In *ICCV*, pages 1232–1241, 2019.

[91] Zhengyi Liu, Yuan Wang, Zhengzheng Tu, Yun Xiao, and Bin Tang. Tritransnet: Rgb-d salient object detection with a triplet transformer embedding network. In *ACM MM*, pages 4481–4490, 2021.

[92] Ao Luo, Xin Li, Fan Yang, Zhicheng Jiao, Hong Cheng, and Siwei Lyu. Cascade graph neural networks for rgb-d salient object detection. In *ECCV*, pages 346–364, 2020.

[93] Yunqiu Lv, Jing Zhang, Yuchao Dai, Aixuan Li, Bowen Liu, Nick Barnes, and Deng-Ping Fan. Simultaneously localize, segment and rank the camouflaged objects. In *CVPR*, pages 11591–11601, 2021.

[94] Mingcan Ma, Changqun Xia, and Jia Li. Pyramidal feature shrinking for salient object detection. In *AAAI*, pages 2311–2318, 2021.

[95] Ran Margolin, Lihi Zelnik-Manor, and Ayellet Tal. How to evaluate foreground maps? In *CVPR*, pages 248–255, 2014.

[96] Haiyang Mei, Bo Dong, Wen Dong, Pieter Peers, Xin Yang, Qiang Zhang, and Xiaopeng Wei. Depth-aware mirror segmentation. In *CVPR*, pages 3044–3053, 2021.

[97] Haiyang Mei, Ge-Peng Ji, Ziqi Wei, Xin Yang, Xiaopeng Wei, and Deng-Ping Fan. Camouflaged object segmentation with distraction mining. In *CVPR*, pages 8772–8781, 2021.

[98] Haiyang Mei, Xin Yang, Yang Wang, Yuanyuan Liu, Shengfeng He, Qiang Zhang, Xiaopeng Wei, and Rynson WH Lau. Don’t hit me! glass detection in real-world scenes. In *CVPR*, pages 3687–3696, 2020.

[99] Tan-Cong Nguyen, Tien-Phat Nguyen, Gia-Han Diep, Anh-Huy Tran-Dinh, Tam V Nguyen, and Minh-Triet Tran. Ccbanet: Cascading context and balancing attention for polyp segmentation. In *MICCAI*, pages 633–643, 2021.

[100] Yuzhen Niu, Yujie Geng, Xueqing Li, and Feng Liu. Leveraging stereopsis for saliency analysis. In *CVPR*, pages 454–461, 2012.

[101] Youwei Pang, Lihe Zhang, Xiaoqi Zhao, and Huchuan Lu. Hierarchical dynamic filtering network for rgb-d salient object detection. In *ECCV*, pages 235–252, 2020.

[102] Youwei Pang, Xiaoqi Zhao, Lihe Zhang, and Huchuan Lu. Multi-scale interactive network for salient object detection. In *CVPR*, pages 9413–9422, 2020.

[103] Hyojin Park, Youngjoon Yoo, Geonseok Seo, Dongyoон Han, Sangdoo Yun, and Nojun Kwak. C3: Concentrated-comprehensive convolution and its application to semantic segmentation. *arXiv preprint arXiv:1812.04920*, 2018.

[104] Chao Peng, Xiangyu Zhang, Gang Yu, Guiming Luo, and Jian Sun. Large kernel matters—improve semantic segmentation by global convolutional network. In *CVPR*, pages 4353–4361, 2017.

[105] Houwen Peng, Bing Li, Weihua Xiong, Weiming Hu, and Rongrong Ji. Rgb-d salient object detection: A benchmark and algorithms. In *ECCV*, pages 92–109, 2014.

[106] Federico Perazzi, Philipp Krähenbühl, Yael Pritch, and Alexander Hornung. Saliency filters: Contrast based filtering for salient region detection. In *CVPR*, pages 733–740, 2012.

[107] Yongri Piao, Wei Ji, Jingjing Li, Miao Zhang, and Huchuan Lu. Depth-induced multi-scale recurrent attention network for saliency detection. In *ICCV*, pages 7254–7263, 2019.

[108] Yongri Piao, Zhengkun Rong, Miao Zhang, Weisong Ren, and Huchuan Lu. A2dele: Adaptive and attentive depth distiller for efficient rgb-d salient object detection. In *CVPR*, pages 9060–9069, 2020.

[109] Xuebin Qin, Zichen Zhang, Chenyang Huang, Masood Dehghan, Osmar R Zaiane, and Martin Jagersand. U2-net: Going deeper with nested u-structure for salient object detection. *Pattern Recognition*, 106:107404, 2020.

[110] Xuebin Qin, Zichen Zhang, Chenyang Huang, Chao Gao, Masood Dehghan, and Martin Jagersand. Basnet: Boundary-aware salient object detection. In *CVPR*, pages 7479–7489, 2019.

- [111] Jingjing Ren, Xiaowei Hu, Lei Zhu, Xuemiao Xu, Yangyang Xu, Weiming Wang, Zijun Deng, and Pheng-Ann Heng. Deep texture-aware features for camouflaged object detection. *IEEE TCSVT*, 2021.
- [112] Zhixiang Ren, Shenghua Gao, Liang-Tien Chia, and Ivor Wai-Hung Tsang. Region-based saliency detection and its application in object recognition. *IEEE TCSVT*, 24(5):769–779, 2013.
- [113] Olaf Ronneberger, Philipp Fischer, and Thomas Brox. U-net: Convolutional networks for biomedical image segmentation. In *MICCAI*, pages 234–241, 2015.
- [114] Zhao Rui, Wanli Ouyang, and Xiaogang Wang. Unsupervised salience learning for person re-identification. In *CVPR*, 2013.
- [115] Anat Caspi Linda Shapiro Sachin Mehta, Mohammad Rastegari and Hannaneh Hajishirzi. Espnet: Efficient spatial pyramid of dilated convolutions for semantic segmentation. In *ECCV*, 2018.
- [116] Mark Sandler, Andrew Howard, Menglong Zhu, Andrey Zhmoginov, and Liang-Chieh Chen. Mobilenetv2: Inverted residuals and linear bottlenecks. In *CVPR*, pages 4510–4520, 2018.
- [117] Yutian Shen, Xiao Jia, and Max Q-H Meng. Hrenet: A hard region enhancement network for polyp segmentation. In *MICCAI*, pages 559–568, 2021.
- [118] Yutian Shen, Xiao Jia, Jin Pan, and Max Q-H Meng. Aprnet: Alternative prediction refinement network for polyp segmentation. In *IEEE EMBC*, pages 3114–3117, 2021.
- [119] Jianping Shi, Li Xu, and Jiaya Jia. Discriminative blur detection features. In *CVPR*, pages 2965–2972, 2014.
- [120] Juan Silva, Aymeric Histace, Olivier Romain, Xavier Dray, and Bertrand Granado. Toward embedded detection of polyps in wce images for early diagnosis of colorectal cancer. *IJCARS*, 9:283–293, 2014.
- [121] Karen Simonyan and Andrew Zisserman. Very deep convolutional networks for large-scale image recognition. *arXiv preprint arXiv:1409.1556*, 2014.
- [122] Avishek Siris, Jianbo Jiao, Gary KL Tam, Xianghua Xie, and Rynson WH Lau. Scene context-aware salient object detection. In *ICCV*, pages 4156–4166, 2021.
- [123] P Skurowski, H Abdulameer, J Błaszczyk, T Depta, A Kornacki, and P Koziel. Animal camouflage analysis: Chameleon database. *Unpublished Manuscript*, 2018.
- [124] Martin Stevens and Sami Merilaita. Animal camouflage: current issues and new perspectives. *Philosophical Transactions of the Royal Society B: Biological Sciences*, 364:423–427, 2009.
- [125] Jinming Su, Jia Li, Yu Zhang, Changqun Xia, and Yonghong Tian. Selectivity or invariance: Boundary-aware salient object detection. In *ICCV*, pages 3799–3808, 2019.
- [126] Peng Sun, Wenhui Zhang, Huanyu Wang, Songyuan Li, and Xi Li. Deep rgb-d saliency detection with depth-sensitive attention and automatic multi-modal fusion. In *CVPR*, pages 1407–1417, 2021.
- [127] Nima Tajbakhsh, Suryakanth R Gurudu, and Jianming Liang. Automated polyp detection in colonoscopy videos using shape and context information. *IEEE TMI*, 35:630–644, 2015.
- [128] Naoya Takahashi and Yuki Mitsufuji. Densely connected multidilated convolutional networks for dense prediction tasks. In *CVPR*, pages 993–1002, 2021.
- [129] Mingxing Tan and Quoc Le. Efficientnet: Rethinking model scaling for convolutional neural networks. In *ICML*, pages 6105–6114, 2019.
- [130] Chang Tang, Xinwang Liu, Shan An, and Pichao Wang. Br2net: Defocus blur detection via a bidirectional channel attention residual refining network. *IEEE TMM*,

23:624–635, 2020.

[131] Chang Tang, Xinwang Liu, Xinzhong Zhu, En Zhu, Kun Sun, Pichao Wang, Lizhe Wang, and Albert Zomaya. R2mrf: Defocus blur detection via recurrently refining multi-scale residual features. In *AAAI*, pages 12063–12070, 2020.

[132] Chang Tang, Xinzhong Zhu, Xinwang Liu, Lizhe Wang, and Albert Zomaya. Defusionnet: Defocus blur detection via recurrently fusing and refining multi-scale deep features. In *CVPR*, pages 2700–2709, 2019.

[133] Lv Tang, Bo Li, Yijie Zhong, Shouhong Ding, and Mofei Song. Disentangled high quality salient object detection. In *ICCV*, pages 3580–3590, 2021.

[134] Hugo Touvron, Matthieu Cord, Matthijs Douze, Francisco Massa, Alexandre Sablayrolles, and Hervé Jégou. Training data-efficient image transformers & distillation through attention. In *ICML*, pages 10347–10357, 2021.

[135] Zhengzheng Tu, Chao Wang, Chenglong Li, Minghao Fan, Haifeng Zhao, and Bin Luo. Orsi salient object detection via multiscale joint region and boundary model. *IEEE TGRS*, 60:1–13, 2022.

[136] David Vázquez, Jorge Bernal, F Javier Sánchez, Gloria Fernández-Esparrach, Antonio M López, Adriana Romero, Michal Drozdzal, and Aaron Courville. A benchmark for endoluminal scene segmentation of colonoscopy images. *JHE*, 2017, 2017.

[137] Tomás F Yago Vicente, Minh Hoai, and Dimitris Samaras. Leave-one-out kernel optimization for shadow detection. In *ICCV*, pages 3388–3396, 2015.

[138] Tomás F Yago Vicente, Le Hou, Chen-Ping Yu, Minh Hoai, and Dimitris Samaras. Large-scale training of shadow detectors with noisily-annotated shadow examples. In *ECCV*, pages 816–832, 2016.

[139] Bo Wang, Quan Chen, Min Zhou, Zhiqiang Zhang, Xiaogang Jin, and Kun Gai. Progressive feature polishing network for salient object detection. In *AAAI*, pages 12128–12135, 2020.

[140] Jifeng Wang, Xiang Li, and Jian Yang. Stacked conditional generative adversarial networks for jointly learning shadow detection and shadow removal. In *CVPR*, pages 1788–1797, 2018.

[141] Jifeng Wang, Xiang Li, and Jian Yang. Stacked conditional generative adversarial networks for jointly learning shadow detection and shadow removal. In *CVPR*, pages 1788–1797, 2018.

[142] Lijun Wang, Huchuan Lu, Yifan Wang, Mengyang Feng, Dong Wang, Baocai Yin, and Xiang Ruan. Learning to detect salient objects with image-level supervision. In *CVPR*, pages 136–145, 2017.

[143] Miao Wang, Xingwei An, Yuhao Li, Ning Li, Wei Hang, and Gang Liu. Ems-net: Enhanced multi-scale network for polyp segmentation. In *IEEE EMBC*, pages 2936–2939, 2021.

[144] Ningning Wang and Xiaojin Gong. Adaptive fusion for rgb-d salient object detection. *IEEE Access*, 7:55277–55284, 2019.

[145] Tiantian Wang, Lihe Zhang, Shuo Wang, Huchuan Lu, Gang Yang, Xiang Ruan, and Ali Borji. Detect globally, refine locally: A novel approach to saliency detection. In *CVPR*, pages 3127–3135, 2018.

[146] Wenguan Wang, Jianbing Shen, Ming-Ming Cheng, and Ling Shao. An iterative and cooperative top-down and bottom-up inference network for salient object detection. In *CVPR*, pages 5968–5977, 2019.

[147] Wenguan Wang, Shuyang Zhao, Jianbing Shen, Steven CH Hoi, and Ali Borji. Salient object detection with pyramid attention and salient edges. In *CVPR*, pages 1448–1457, 2019.

- [148] Xiaolong Wang, Ross Girshick, Abhinav Gupta, and Kaiming He. Non-local neural networks. In *CVPR*, pages 7794–7803, 2018.
- [149] Zhengyang Wang and Shuiwang Ji. Smoothed dilated convolutions for improved dense prediction. In *ACM SIGKDD*, pages 2486–2495, 2018.
- [150] Jun Wei, Yiwen Hu, Ruimao Zhang, Zhen Li, S Kevin Zhou, and Shuguang Cui. Shallow attention network for polyp segmentation. In *MICCAI*, pages 699–708, 2021.
- [151] Jun Wei, Shuhui Wang, and Qingming Huang. F³net: Fusion, feedback and focus for salient object detection. In *AAAI*, pages 12321–12328, 2020.
- [152] Jun Wei, Shuhui Wang, Zhe Wu, Chi Su, Qingming Huang, and Qi Tian. Label decoupling framework for salient object detection. In *CVPR*, pages 13025–13034, 2020.
- [153] Hongfa Wen, Chenggang Yan, Xiaofei Zhou, Runmin Cong, Yaoqi Sun, Bolun Zheng, Jiyong Zhang, Yongjun Bao, and Guiguang Ding. Dynamic selective network for rgb-d salient object detection. *IEEE TIP*, 30:9179–9192, 2021.
- [154] Huisi Wu, Jiafu Zhong, Wei Wang, Zhenkun Wen, and Jing Qin. Precise yet efficient semantic calibration and refinement in convnets for real-time polyp segmentation from colonoscopy videos. In *AAAI*, pages 2916–2924, 2021.
- [155] Lin Wu, Xiaochun Cao, and Hassan Foroosh. Camera calibration and geolocation estimation from two shadow trajectories. *CVIU*, 114:915–927, 2010.
- [156] Runmin Wu, Mengyang Feng, Wenlong Guan, Dong Wang, Huchuan Lu, and Errui Ding. A mutual learning method for salient object detection with intertwined multi-supervision. In *CVPR*, pages 8150–8159, 2019.
- [157] Tianyi Wu, Sheng Tang, Rui Zhang, Juan Cao, and JinTao Li. Tree-structured kronecker convolutional network for semantic segmentation. In *ICME*, pages 940–945, 2019.
- [158] Zhe Wu, Li Su, and Qingming Huang. Cascaded partial decoder for fast and accurate salient object detection. In *CVPR*, pages 3907–3916, 2019.
- [159] Zhe Wu, Li Su, and Qingming Huang. Stacked cross refinement network for edge-aware salient object detection. In *ICCV*, pages 7264–7273, 2019.
- [160] Enze Xie, Wenjia Wang, Wenhui Wang, Mingyu Ding, Chunhua Shen, and Ping Luo. Segmenting transparent objects in the wild. In *ECCV*, pages 696–711, 2020.
- [161] Enze Xie, Wenjia Wang, Wenhui Wang, Peize Sun, Hang Xu, Ding Liang, and Ping Luo. Segmenting transparent objects in the wild with transformer. In *IJCAI*, pages 1194–1200, 2021.
- [162] Saining Xie, Ross Girshick, Piotr Dollár, Zhuowen Tu, and Kaiming He. Aggregated residual transformations for deep neural networks. In *CVPR*, pages 1492–1500, 2017.
- [163] Binwei Xu, Haoran Liang, Ronghua Liang, and Peng Chen. Locate globally, segment locally: A progressive architecture with knowledge review network for salient object detection. In *AAAI*, pages 3004–3012, 2021.
- [164] Yingyue Xu, Dan Xu, Xiaopeng Hong, Wanli Ouyang, Rongrong Ji, Min Xu, and Guoying Zhao. Structured modeling of joint deep feature and prediction refinement for salient object detection. In *ICCV*, pages 3789–3798, 2019.
- [165] Jinnan Yan, Trung-Nghia Le, Khanh-Duy Nguyen, Minh-Triet Tran, Thanh-Toan Do, and Tam V Nguyen. Mirrornet: Bio-inspired camouflaged object segmentation. *IEEE Access*, 9:43290–43300, 2021.

[166] Qiong Yan, Li Xu, Jianping Shi, and Jiaya Jia. Hierarchical saliency detection. In *CVPR*, pages 1155–1162, 2013.

[167] Chuan Yang, Lihe Zhang, Huchuan Lu, Xiang Ruan, and Ming-Hsuan Yang. Saliency detection via graph-based manifold ranking. In *CVPR*, pages 3166–3173, 2013.

[168] Fan Yang, Qiang Zhai, Xin Li, Rui Huang, Ao Luo, Hong Cheng, and Deng-Ping Fan. Uncertainty-guided transformer reasoning for camouflaged object detection. In *ICCV*, pages 4146–4155, 2021.

[169] Guangyu Robert Yang, John D Murray, and Xiao-Jing Wang. A dendritic disinhibitory circuit mechanism for pathway-specific gating. *Nature communications*, 7:12815, 2016.

[170] Maoke Yang, Kun Yu, Chi Zhang, Zhiwei Li, and Kuiyuan Yang. Denseaspp for semantic segmentation in street scenes. In *CVPR*, pages 3684–3692, 2018.

[171] Xin Yang, Haiyang Mei, Ke Xu, Xiaopeng Wei, Baocai Yin, and Rynson WH Lau. Where is my mirror? In *ICCV*, pages 8809–8818, 2019.

[172] Li Yuan, Yunpeng Chen, Tao Wang, Weihao Yu, Yujun Shi, Zi-Hang Jiang, Francis E.H. Tay, Jiashi Feng, and Shuicheng Yan. Tokens-to-token vit: Training vision transformers from scratch on imagenet. In *ICCV*, pages 558–567, 2021.

[173] Yi Zeng, Pingping Zhang, Jianming Zhang, Zhe Lin, and Huchuan Lu. Towards high-resolution salient object detection. In *ICCV*, pages 7234–7243, 2019.

[174] Qiang Zhai, Xin Li, Fan Yang, Chengli Zhao Chen, Hong Cheng, and Deng-Ping Fan. Mutual graph learning for camouflaged object detection. In *CVPR*, pages 12997–13007, 2021.

[175] Chen Zhang, Runmin Cong, Qinwei Lin, Lin Ma, Feng Li, Yao Zhao, and Sam Kwong. Cross-modality discrepant interaction network for rgb-d salient object detection. In *ACM MM*, pages 2094–2102, 2021.

[176] Jing Zhang, Deng-Ping Fan, Yuchao Dai, Saeed Anwar, Fatemeh Sadat Saleh, Tong Zhang, and Nick Barnes. Uc-net: Uncertainty inspired rgb-d saliency detection via conditional variational autoencoders. In *CVPR*, pages 8582–8591, 2020.

[177] Jing Zhang, Deng-Ping Fan, Yuchao Dai, Xin Yu, Yiran Zhong, Nick Barnes, and Ling Shao. Rgb-d saliency detection via cascaded mutual information minimization. In *ICCV*, pages 4338–4347, 2021.

[178] Lu Zhang, Ju Dai, Huchuan Lu, You He, and Gang Wang. A bi-directional message passing model for salient object detection. In *CVPR*, pages 1741–1750, 2018.

[179] Lu Zhang, Jianming Zhang, Zhe Lin, Huchuan Lu, and You He. Capsal: Leveraging captioning to boost semantics for salient object detection. In *CVPR*, pages 6024–6033, 2019.

[180] Miao Zhang, Sun Xiao Fei, Jie Liu, Shuang Xu, Yongri Piao, and Huchuan Lu. Asymmetric two-stream architecture for accurate rgb-d saliency detection. In *ECCV*, pages 374–390, 2020.

[181] Miao Zhang, Tingwei Liu, Yongri Piao, Shunyu Yao, and Huchuan Lu. Auto-msfnet: Search multi-scale fusion network for salient object detection. In *ACM MM*, pages 667–676, 2021.

[182] Miao Zhang, Weisong Ren, Yongri Piao, Zhengkun Rong, and Huchuan Lu. Select, supplement and focus for rgb-d saliency detection. In *CVPR*, pages 3472–3481, 2020.

[183] Miao Zhang, Yu Zhang, Yongri Piao, Beiqi Hu, and Huchuan Lu. Feature reintegration over differential treatment: A top-down and adaptive fusion network for rgb-d salient object detection. In *ACM MM*, pages 4107–4115, 2020.

[184] Pingping Zhang, W. Liu, Huchuan Lu, and Chunhua Shen. Salient object detection by

lossless feature reflection. In *IJCAI*, page 1149–1155, 2018.

[185] Pingping Zhang, Dong Wang, Huchuan Lu, Hongyu Wang, and Xiang Ruan. Amulet: Aggregating multi-level convolutional features for salient object detection. In *ICCV*, pages 202–211, 2017.

[186] Qijian Zhang, Runmin Cong, Chongyi Li, Ming-Ming Cheng, Yuming Fang, Xiaochun Cao, Yao Zhao, and Sam Kwong. Dense attention fluid network for salient object detection in optical remote sensing images. *IEEE TIP*, 30:1305–1317, 2020.

[187] Ruifei Zhang, Guanbin Li, Zhen Li, Shuguang Cui, Dahong Qian, and Yizhou Yu. Adaptive context selection for polyp segmentation. In *MICCAI*, pages 253–262, 2020.

[188] Wenbo Zhang, Ge-Peng Ji, Zhuo Wang, Keren Fu, and Qijun Zhao. Depth quality-inspired feature manipulation for efficient rgb-d salient object detection. In *ACM MM*, pages 731–740, 2021.

[189] Xiaoning Zhang, Tiantian Wang, Jinqing Qi, Huchuan Lu, and Gang Wang. Progressive attention guided recurrent network for salient object detection. In *CVPR*, pages 714–722, 2018.

[190] Yundong Zhang, Huiye Liu, and Qiang Hu. Transfuse: Fusing transformers and cnns for medical image segmentation. In *MICCAI*, pages 14–24, 2021.

[191] Fan Zhao, Huimin Lu, Wenda Zhao, and Libo Yao. Image-scale-symmetric cooperative network for defocus blur detection. *IEEE TCSVT*, 2021.

[192] Hengshuang Zhao, Jianping Shi, Xiaojuan Qi, Xiaogang Wang, and Jiaya Jia. Pyramid scene parsing network. In *CVPR*, pages 2881–2890, 2017.

[193] Jia-Xing Zhao, Yang Cao, Deng-Ping Fan, Ming-Ming Cheng, Xuan-Yi Li, and Le Zhang. Contrast prior and fluid pyramid integration for rgbd salient object detection. In *CVPR*, pages 3922–3931, 2019.

[194] Jia-Xing Zhao, Jiang-Jiang Liu, Deng-Ping Fan, Yang Cao, Jufeng Yang, and Ming-Ming Cheng. Egnet: Edge guidance network for salient object detection. In *ICCV*, pages 8779–8788, 2019.

[195] Jiawei Zhao, Yifan Zhao, Jia Li, and Xiaowu Chen. Is depth really necessary for salient object detection? In *ACM MM*, pages 1745–1754, 2020.

[196] Ting Zhao and Xiangqian Wu. Pyramid feature attention network for saliency detection. In *CVPR*, pages 3085–3094, 2019.

[197] Wenda Zhao, Xueqing Hou, You He, and Huchuan Lu. Defocus blur detection via boosting diversity of deep ensemble networks. *IEEE TIP*, 30:5426–5438, 2021.

[198] Wenda Zhao, Cai Shang, and Huchuan Lu. Self-generated defocus blur detection via dual adversarial discriminators. In *CVPR*, pages 6933–6942, 2021.

[199] Wenda Zhao, Fan Zhao, Dong Wang, and Huchuan Lu. Defocus blur detection via multi-stream bottom-top-bottom fully convolutional network. In *CVPR*, pages 3080–3088, 2018.

[200] Wenda Zhao, Bowen Zheng, Qiuhua Lin, and Huchuan Lu. Enhancing diversity of defocus blur detectors via cross-ensemble network. In *CVPR*, pages 8905–8913, 2019.

[201] Xiaoqi Zhao, Youwei Pang, Lihe Zhang, Huchuan Lu, and Lei Zhang. Suppress and balance: A simple gated network for salient object detection. In *ECCV*, pages 35–51, 2020.

[202] Xiaoqi Zhao, Lihe Zhang, and Huchuan Lu. Automatic polyp segmentation via multi-scale subtraction network. In *MICCAI*, pages 120–130, 2021.

[203] Xiaoqi Zhao, Lihe Zhang, Youwei Pang, Huchuan Lu, and Lei Zhang. A single

stream network for robust and real-time rgb-d salient object detection. In *ECCV*, pages 646–662, 2020.

[204] Yifan Zhao, Jiawei Zhao, Jia Li, and Xiaowu Chen. Rgb-d salient object detection with ubiquitous target awareness. *IEEE TIP*, 30:7717–7731, 2021.

[205] Zhirui Zhao, Changqun Xia, Chenxi Xie, and Jia Li. Complementary trilateral decoder for fast and accurate salient object detection. In *ACM MM*, pages 4967–4975, 2021.

[206] Quanlong Zheng, Xiaotian Qiao, Ying Cao, and Rynson WH Lau. Distraction-aware shadow detection. In *CVPR*, pages 5167–5176, 2019.

[207] Huajun Zhou, Xiaohua Xie, Jian-Huang Lai, Zixuan Chen, and Lingxiao Yang. Interactive two-stream decoder for accurate and fast saliency detection. In *CVPR*, pages 9141–9150, 2020.

[208] Tao Zhou, Huazhu Fu, Geng Chen, Yi Zhou, Deng-Ping Fan, and Ling Shao. Specificity-preserving rgb-d saliency detection. In *ICCV*, pages 4681–4691, 2021.

[209] Xiaofei Zhou, Kunye Shen, Zhi Liu, Chen Gong, Jiyong Zhang, and Cheng-gang Clarence Yan. Edge-aware multi-scale feature integration network for salient object detection in optical remote sensing images. *IEEE TGRS*, 60:1–15, 2022.

[210] Ziqi Zhou, Zheng Wang, Huchuan Lu, Song Wang, and Meijun Sun. Multi-type self-attention guided degraded saliency detection. In *AAAI*, pages 13082–13089, 2020.

[211] Zongwei Zhou, Md Mahfuzur Rahman Sidiquee, Nima Tajbakhsh, and Jianming Liang. Unet++: Redesigning skip connections to exploit multiscale features in image segmentation. *IEEE TMI*, 39:1856–1867, 2019.

[212] Chunbiao Zhu, Xing Cai, Kan Huang, Thomas H Li, and Ge Li. Pdnet: Prior-model guided depth-enhanced network for salient object detection. In *ICME*, pages 199–204, 2019.

[213] Chunbiao Zhu and Ge Li. A three-pathway psychobiological framework of salient object detection using stereoscopic technology. In *ICCVW*, pages 3008–3014, 2017.

[214] Jiejie Zhu, Kegan GG Samuel, Syed Z Masood, and Marshall F Tappen. Learning to recognize shadows in monochromatic natural images. In *CVPR*, pages 223–230, 2010.

[215] Lei Zhu, Zijun Deng, Xiaowei Hu, Chi-Wing Fu, Xuemiao Xu, Jing Qin, and Pheng-Ann Heng. Bidirectional feature pyramid network with recurrent attention residual modules for shadow detection. In *ECCV*, pages 121–136, 2018.

[216] Lei Zhu, Ke Xu, Zhanghan Ke, and Rynson WH Lau. Mitigating intensity bias in shadow detection via feature decomposition and reweighting. In *ICCV*, pages 4702–4711, 2021.

[217] Yifan Zhu, Jiaxiong Qiu, and Bo Ren. Transfusion: A novel slam method focused on transparent objects. In *ICCV*, pages 6019–6028, 2021.

[218] Yunzhi Zhuge, Yu Zeng, and Huchuan Lu. Deep embedding features for salient object detection. In *AAAI*, pages 9340–9347, 2019.

[219] Thomas Ziegler, Manuel Fritsche, Lorenz Kuhn, and Konstantin Donhauser. Efficient smoothing of dilated convolutions for image segmentation. *arXiv preprint arXiv:1903.07992*, 2019.

Appendix A Qualitative Evaluation

Fig. A1 - Fig. A10 illustrate some visual comparisons on each sub-task. We summarize the advantages of the GateNet compared to others

when facing some challenges: **I) Interference produced by complex.** In camouflaged object detection and poly segmentation tasks, foreground objects usually share the similar appearance to the background, which can easily deceive predictors. But the GateNet can accurately capture the hidden objects and separate them from the surrounding environment (see the Fig. A9 and Fig. A10). The gated mechanism also plays an important role in RGB -D salient object detection. As shown in Fig. A3, the proposed two-stream GateNet can effectively utilize the guidance information provided by the high-quality depth map while suppressing the interference information from the low-quality depth map, thereby identifying the whole object precisely. **II) Interference produced by adjacent objects.** In the real world, shadows often exist on the ground or desktop, and are closely adjacent to the original object. This characteristic requires shadow detection networks to have the ability to distinguish between adjacent objects. As shown in Fig. A5, most methods are disturbed by the surface or the original object, but our method can focus on the shadow regions. **III) The foreground exists multiple or small objects.** On the one hand, glass-like objects are often present in groups in the real world, which poses a serious challenge to the perception capability of the network for the multiple objects. On the other hand, small objects usually appear in remote sensing images. Benefiting from the Fold-ASPP, both multiple and small objects can be localized accurately. Fig. A4 and Fig. A7 show that our method can accurately distinguish each independent connected region without sticking to each other. GateNet is the only one can provide clean prediction maps and maintain the basic shape of the aircraft (see the 6th - 8th columns in Fig. A2). **IV) Boundary and details.** Our GateNet has a mix feature aggregation decoder that a parallel branch by concatenating the output of the progressive branch and the features of the gated encoder, so that the residual information complementary to the progressive branch is supplemented to generate the final prediction. In this way, the prediction can restore more details, therefore, the limbs and even tentacles of the insects are retained well (see the 3th and 8th columns in Fig. A9). **V) Regional consistency.** In defocus blur detection task, the focused area usually has incomplete semantic information because the

blurred region may also belong to the semantic part of the foreground. Benefiting from the folded operation, our model can obtain more stable structural features to improve the intra-class consistency. From the results in Fig. A6, it can be observed that our method can segment the foreground well while the other methods more or less lose similar areas inside or around focused regions.

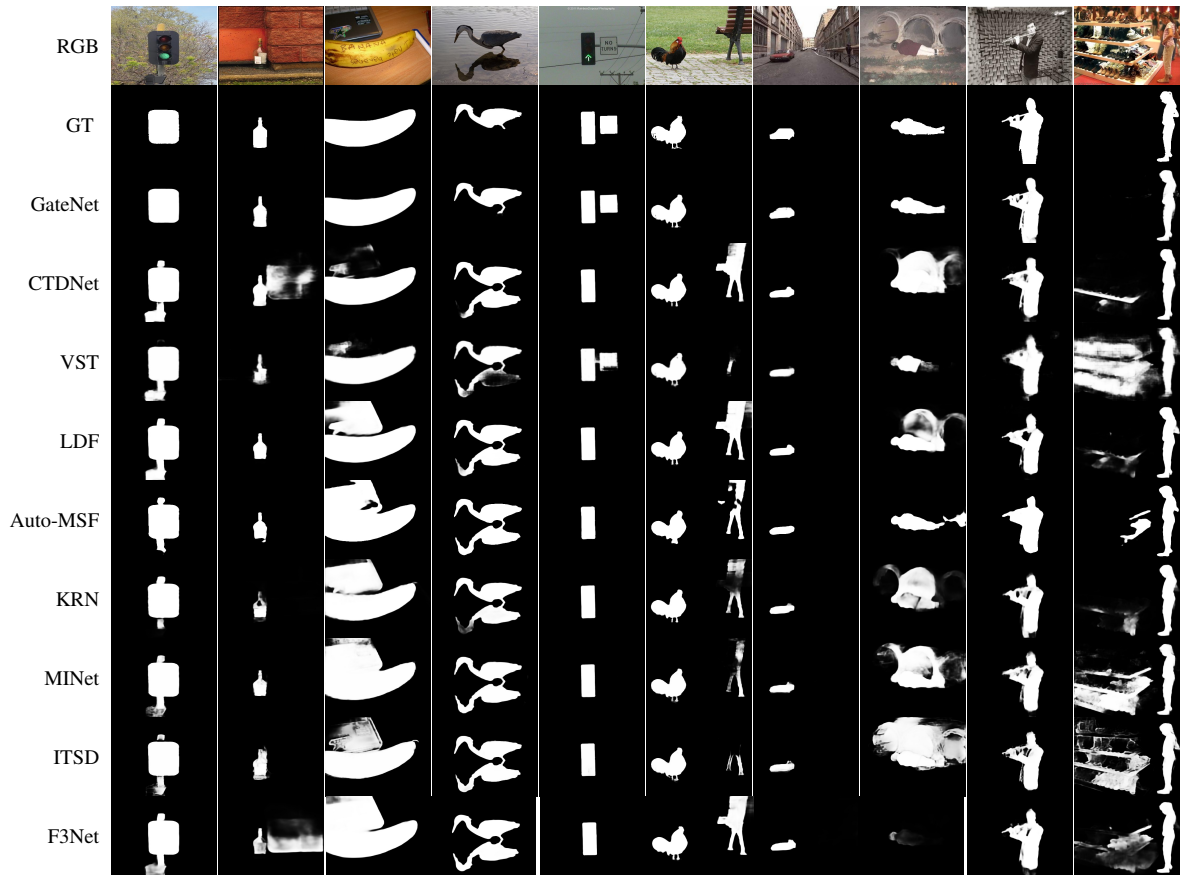


Fig. A1 Visual comparison between our GateNet results and the state-of-the-art methods (CTDNet [205], VST [87], LDF [152], Auto-MSF [181], KRN [163], MINet [102], ITSD [207], F3Net [151]) on **RGB SOD** datasets.

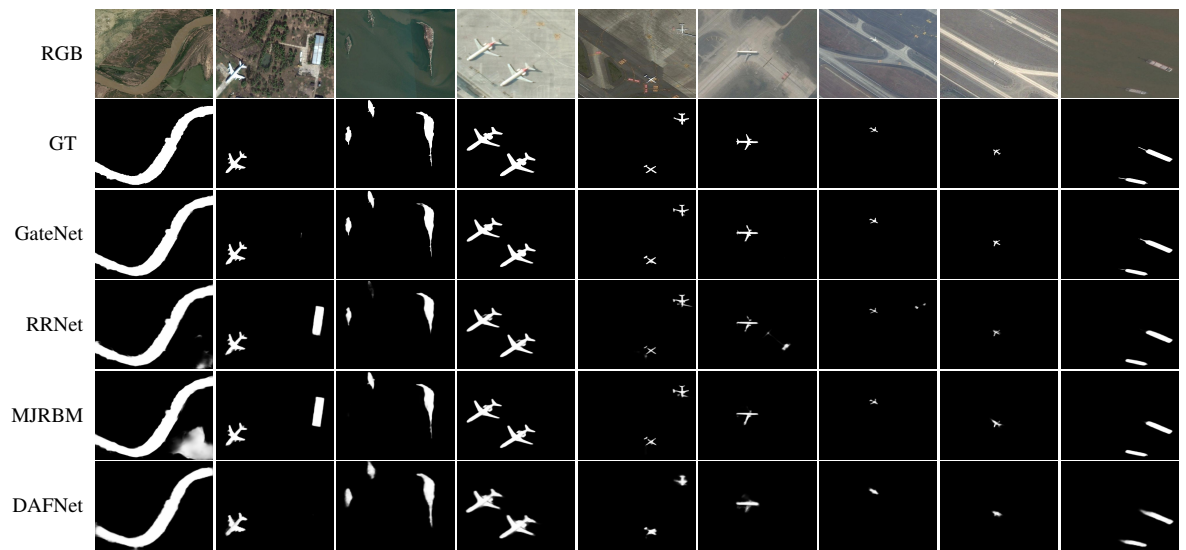


Fig. A2 Visual comparison between our GateNet results and the state-of-the-art methods (RRNet [22], MJRBM [135], DAFNet [186]) on **ORSI SOD** datasets.

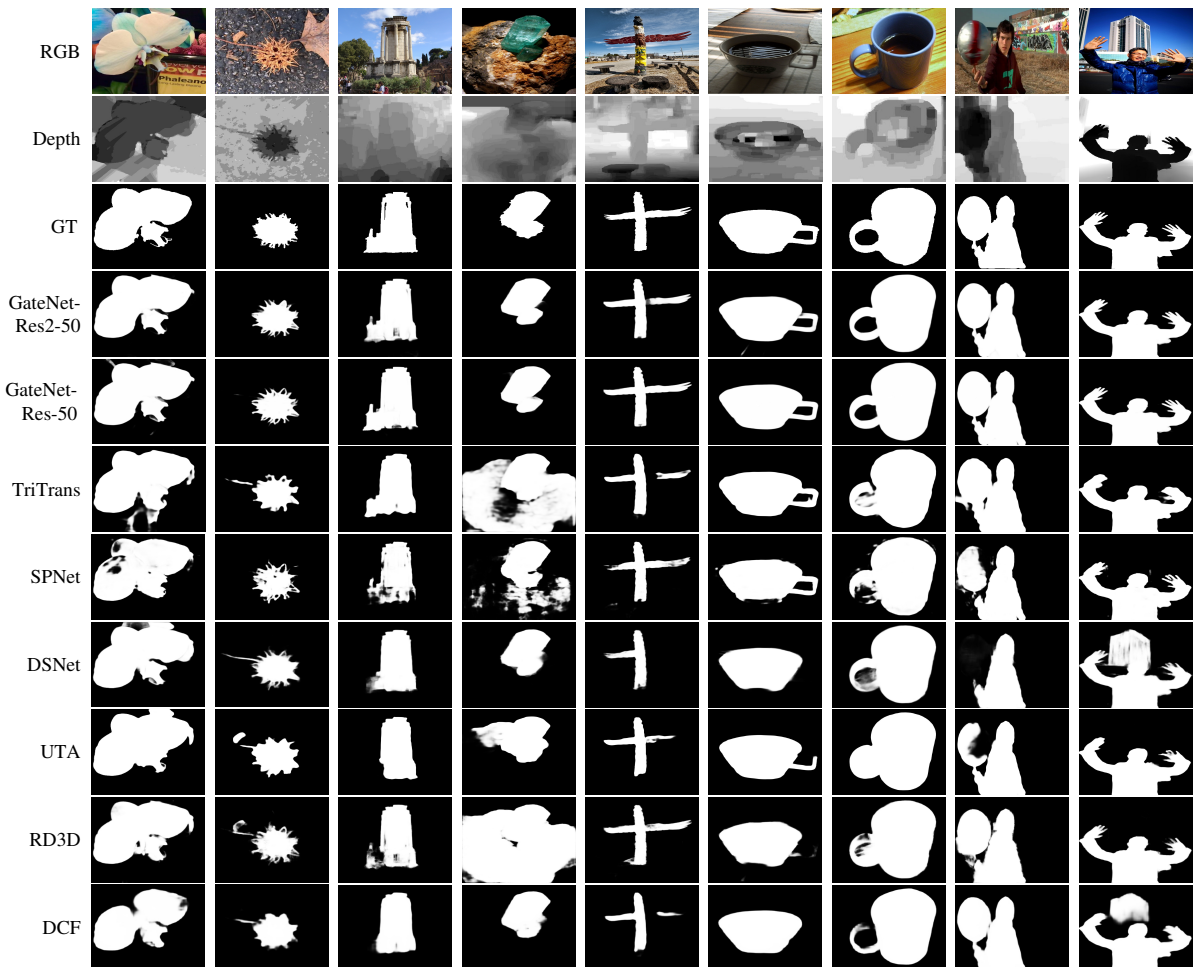


Fig. A3 Visual comparison between our GateNet results and the state-of-the-art methods (TriTransNet [91], SPNet [208], DSNet [153], UTA [204], RD3D [13], DCF [55]) on **RGB-D SOD** datasets.

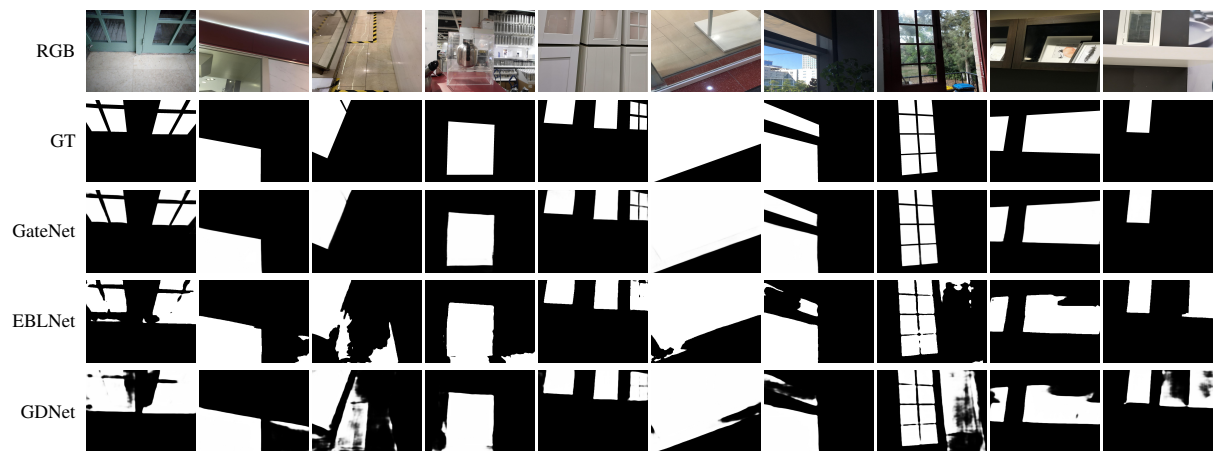


Fig. A4 Visual comparison between our GateNet results and the state-of-the-art methods (EBLNet [43], GDNet [98]) on **Glass Object Detection** datasets.

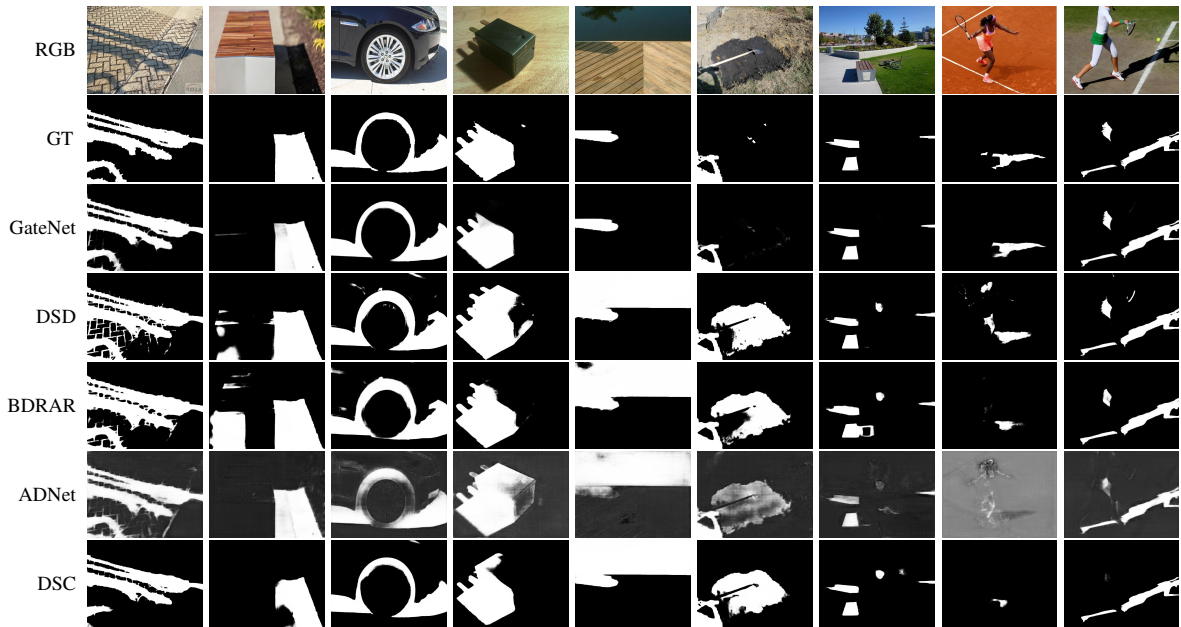


Fig. A5 Visual comparison between our GateNet results and the state-of-the-art methods (DSD [206], BDRAR [215], ADNet [65], DSC [50]) on **Shadow Detection** datasets.



Fig. A6 Visual comparison between our GateNet results and the state-of-the-art methods (DENets [197], IS2CNet [191], SG [198], Depth-Distill [23], CENet [200]) on **Defocus Blur Detection** datasets.

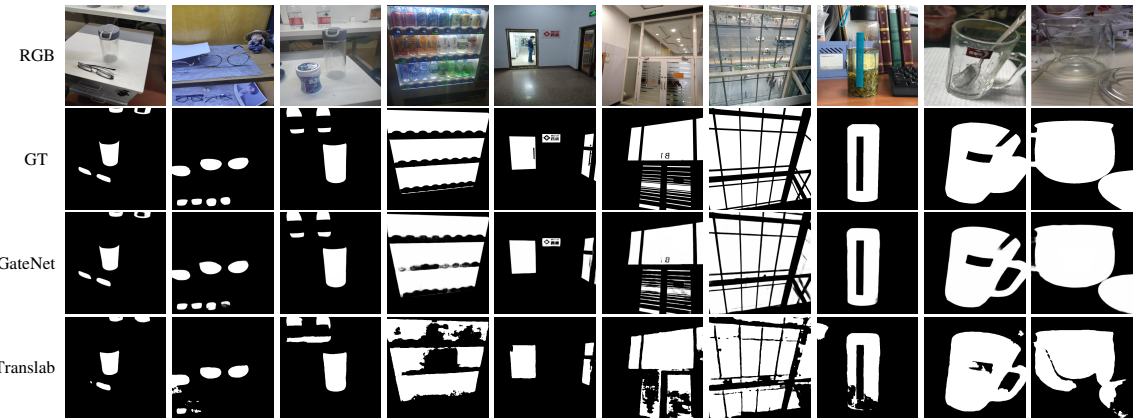


Fig. A7 Visual comparison between our GateNet results and the state-of-the-art method (Translab [160]) on **Transparent Object Detection** datasets.

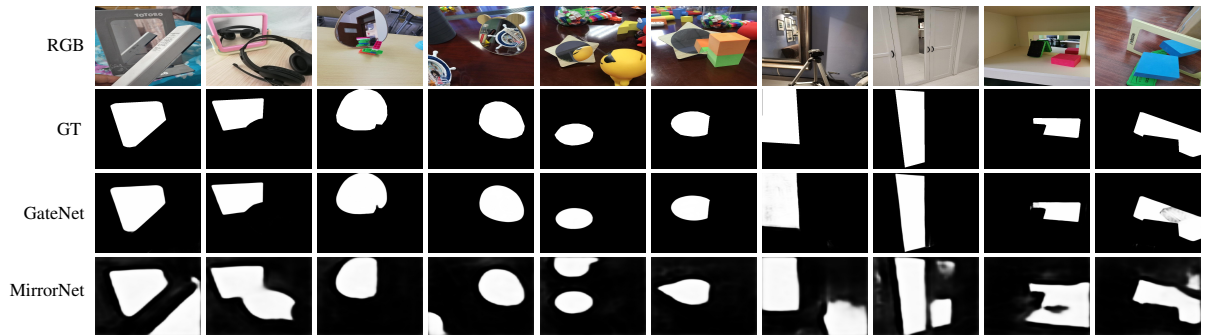


Fig. A8 Visual comparison between our GateNet results and the state-of-the-art method (MirrorNet [171]) on **Mirror Detection** datasets.



Fig. A9 Visual comparison between our GateNet results and the state-of-the-art methods (UGTR [168], IS2CNet [174], RankNet [93], PFNet [97], SINet [30]) on **Camouflaged Object Detection** datasets.

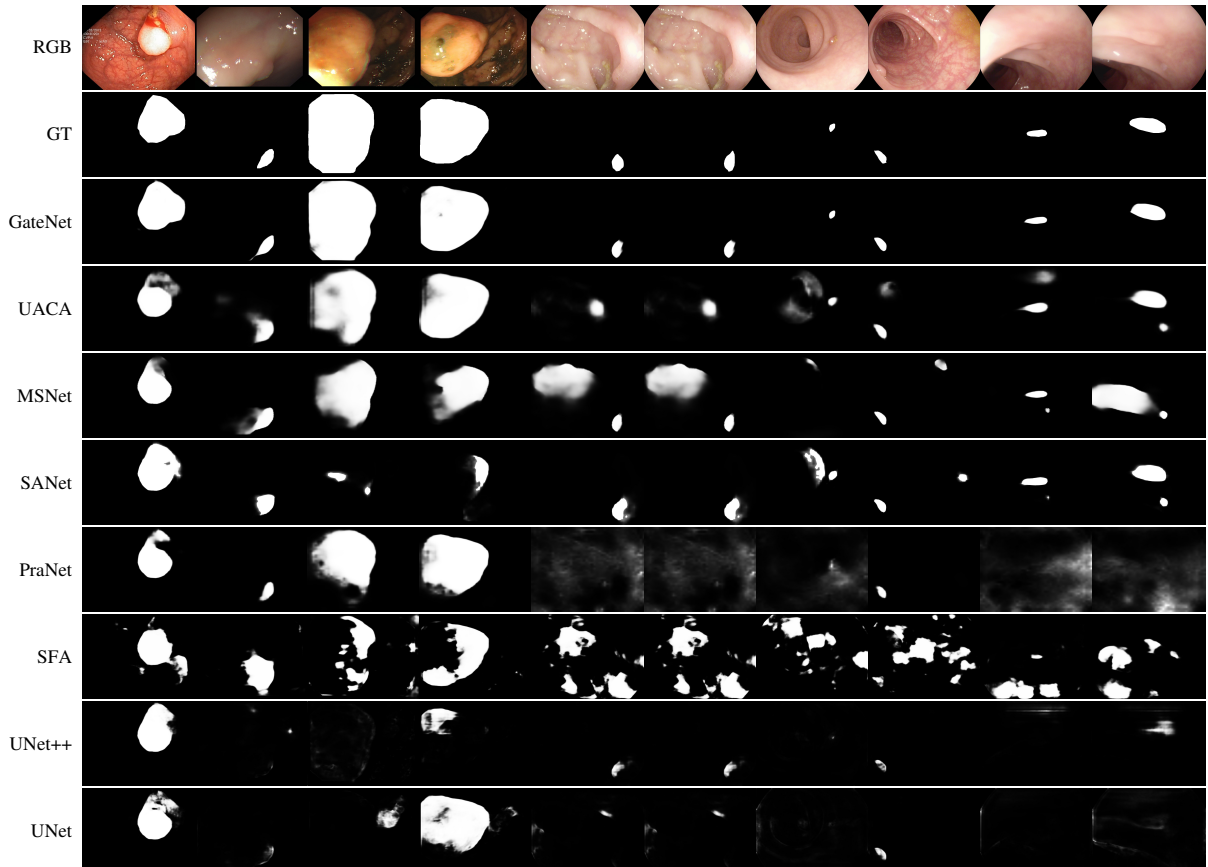


Fig. A10 Visual comparison between our GateNet results and the state-of-the-art methods (UACA [63], MSNet [202], SANet [150], PraNet [31], SFA [36], UNet++ [211], UNet [113]) on **Polyp Segmentation** datasets.